BEAM DYNAMICS IN THE CEBAF SUPERCONDUCTING CAVITIES

A Dissertation
Presented to
The Faculty of the Physics Department
The College of William and Mary in Virginia

in Partial Fulfillment
of the Requirements for the Degree of
Doctor of Philosophy

---

by
Zenghai Li
March 1995

Douglas

This dissertation is submitted in partial fulfillment of
the requirements for the degree of
Doctor of Philosophy

Zenghai Li

Approved, March 1995

Joseph J. Bisognano

Morton Eckhause

Eugene R. Tracy

John D. Walecka

David Douglas
CEBAF

Table of Contents

Acknowledgements

I wish to thank my adviser, Prof. Joseph J. Bisognano, for his guidance, support, and encouragement during the whole course of this research.

I wish to thank Dr. Byung Yunn for his generous help on running MAFIA and TBCI and many discussions on cavity modeling and wake field calculations. Thanks are also due to Dr. David Douglas for fruitful discussions on beam dynamics and on emittance measurements. Thanks to Dr. Geoferry A. Krafft for his help on cavity steering measurement, and discussions on cavity azimuthal focusing. Thanks to Dr. Mike Tiefenback and Dr. Byung Yunn for collaborating on cavity focusing measurements. Thanks to Dr. Steve Benson and Dr. Lia Merminga for their interest and help on cavity focusing measurements. The machine control center staff has been very helpful on the experiments carried out. Thanks to Dr. Rui Li for discussions on wakefield calculations.

I would like to acknowledge the collaboration between the College of William and Mary and CEBAF and the administrative support provided by both institutions, which made this work possible.

Finally, I wish to thank my wife, Zhaomei Zhang, for her unwavering love, support, and understanding throughout the whole course of this work. She took most of the responsibility of the family, and let me concentrate more on my research. I am grateful to my parents, Linsheng and Jihau Li, for their love and support.

This work was supported by the U.S. Department of Energy under contract No. DE-AC05-84ER40150.

List of Tables

List of Figures

ABSTRACT

This work is a study of beam dynamics in the CEBAF superconducting cavities under the influence of the fields generated by externally applied RF and beam particles.

A full 3-D modeling of the CEBAF 5-cell superconducting cavity is carried out. Details of the modeling with MAFIA are discussed. Multipole fields due to the asymmetric couplers are studied by means of 3-D Fourier transforms. The cavity steering and focusing of the multipole fields are studied. Experimental measurements of these effects are performed to validate the modeling. Evaluation of the cavity misalignment is discussed. The emittance degradation effects in the CEBAF superconducting linacs and an FEL driver linac due to the head-tail effects of the cavity steering and the $x-y$ coupling effects of the multipole fields are studied.

The beam-cavity interactions for cases of $v_s, v_t \neq c$ are studied. The Lindman boundary condition is implemented to accommodate simulation of infinite long beam pipes of the beam line. A fourth-order finite-difference algorithm is derived in cylindrical coordinates to reduce the frequency dependent truncation errors, which were discovered in the process of calculating wake fields of very short bunches, of the second-order Yee algorithm. The effects of the slippage between the source particle and the test particle are considered in the wake function calculations. Radial scaling relations are obtained for calculating the wake functions on the axis from the integrated value at the beam pipe radius. The scaling found not only depends on the beam energy but also depends on the bunch length of the beam and the opening of the cavity. The conditions for the validity of the ultrarelativistic treatment of the wakefield are discussed.

The emittance growth and the energy spread due to the combined effects of the cavity multipole fields and the wakefields in a 40 MeV IR FEL driver linac are studied.

BEAM DYNAMICS IN THE CEBAF SUPERCONDUCTING CAVITIES

Chapter 1

Introduction

Since the first charged particle accelerator was built in 1932 for nuclear reaction studies, research and development in accelerator physics have blossomed significantly in the past several decades. Today, particle accelerators are found in a wide variety of applications such as nuclear and high energy particle physics research, synchrotron radiation sources for a wide variety of applications of ultraviolet and x-ray beams in material science, medical therapy, heavy ion fusion, oil and natural gas exploration, and food treatment. Electron accelerators are also used to drive free electron lasers (FELs), which provide high power and wavelength tunable light which can meet the needs of basic research and industrial applications.

The heart of each high energy accelerator is the RF accelerating section which is generally composed of a number of accelerating modules each of which is a chain of coupled RF resonant cavities. An accelerating cavity is energized by two power sources. One is the RF generator which supplies power to the cavity in order to make up for the power dissipated in the walls and absorbed by the accelerating beam. Breaking of the cylindrical symmetry of the cavity, for example, by power couplers can generate deflecting fields at the fundamental RF frequency. The other power source is the bunched particle beam itself which deposits energy into the cavity in a wide band of frequencies. The interactions between the beam bunches, the fundamental deflecting fields, and the higher-order modes generated by the beam may result in serious side effects which are the prime factors that limit the beam current. Even if well under the threshold current, the beam quality and the machine performance are still limited by these beam-cavity interactions. The theoretical and experimental study of the beam dynamics in the superconducting linacs is the subject of this dissertation.

This work is performed at the Continuous Electron Beam Accelerator Facility (CEBAF) being built in Newport News, Virginia. The CEBAF superconducting recirculating accelerator will provide electron beams at energies from 0.5 GeV to 4 GeV to nuclear physics experiments in three experimental halls. The CEBAF accelerator compromises a 45 MeV superconducting injector linac, two 400 MeV superconducting linacs, recirculation beam lines, and a beam extraction system. The electron beam can be recirculated five times to yield a beam energy of 4 GeV for three nuclear physics end-stations at average current up to 200 μA. In addition to the average current, good transverse and longitudinal beam quality is necessary for effective nuclear physics experimentation. The design goals are a full energy spread of 10^{-4} and a normalized rms emittance of 0.1 cm·mrad. Recently, it has been proposed to use a superconducting linac to drive an IR FEL. One such FEL driver consists of a 10 MeV superconducting injector and a 30 MeV superconducting linac. The beam final energy is 40 MeV. The normalized rms emittance is 1 cm·mrad. Energy spread (σ_E/E) is 2×10^{-3} at 40 MeV. The reference design will also be addressed in this dissertation.

1.1 The CEBAF superconducting cavity

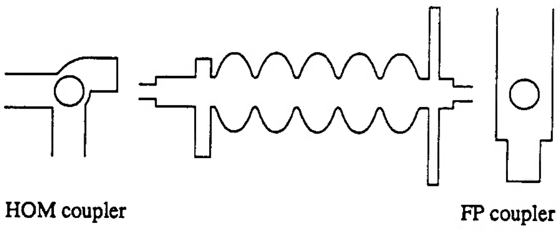

Figure 1-1: The CEBAF 5-cell cavity.

The superconducting cavities used in the CEBAF linacs were initially designed at Cornell. A cavity consists of five elliptical cells and a pair of couplers-one for fundamental power (FP) coupling and one for higher-order-mode (HOM) coupling, Fig. 1-1. The cavity operates with the π mode, which has a frequency of 1497 MHz. The advantage of using a superconducting cavity over a normal temperature cavity is the low operation cost and high field gradient (for CW operation). The unloaded Q, defined as

$$Q = \frac{\omega U}{P_w} \qquad (1-1)$$

where U is the stored energy in the cavity and P_w is the power lost in the Joule heating the cavity wall, of a superconducting cavity (order of 10^9) is much higher than that of a normal copper temperature cavity (order of 10^4). At the same accelerating gradient, for example 5 MV/m for the CEBAF cavity, the dissipated power in a superconducting cavity is less than 5 Watts. Considering the power being absorbed at 2-4 K and the efficiency of the refrigerator at such a low temperature, the total power needed for the wall loss is several kilowatts, which is still hundred of times lower than the power dissipated in an equivalent copper structure. The theoretical limitation on the maximum accelerating gradient for niobium material is about 50 MV/m at 2 K [1]. Higher than 10 MV/m has been obtained experimentally at CEBAF. The nominal gradient of the CEBAF cavities is 5 MV/m. It could be upgraded to higher gradients. Because of the efficiency of the cavities (maximization of shunt impedance is not as crucial as with room temperature cavities) and the requirement of coupling through the beam pipe to avoid sites for multipactoring and breakdown, a typical RF cavity has a large aperture. The large opening reduces the coupling impedance of the higher-order modes; for transverse modes this coupling can be an order of magnitude below that would be expected for an optimized room temperature cavity. The shape of the cells of the CEBAF cavity are elliptical. Two-dimension codes LALA [2] and SUPERFISH [3, 4] were used for cavity-shape optimization and mode analyses.

The 2-D codes only take into account the five cylindrical symmetric cells in the calculation. As a whole, the cavity must have a power coupler to couple the RF power from the generator into the cavity. The asymmetric coupler generates multipole fields in that region. The field of the steering mode steers the beam off axis. This may cause several problems. Firstly, it causes head-tail effects due to the finite length of the bunch and the time variation of the field. Secondly, the off axis particles interact with the cavity and generate HOM fields. This not only creates unwanted Joule heating but also may build up a high field which leads to beam quality degradation or even beam breakup. To avoid such circumstances, the external Qs of dangerous HOMs have to be reduced to low values. This is done by adding the HOM coupler to damp the cavity HOMs. The HOM coupler waveguide propagate only waves with frequencies higher than the fundamental mode. Strong coupler-cell coupling is obtained by using a particular geometry structure and connecting the coupler directly to the end cell of the cavity. Although this can efficiently reduce the wakefield effects, it will generate other side effects like steering and cross-plane coupling. It is these effects of coupler fields that we want to study.

1.2 The effects of the multipole fields of the cavity

The dominant multipole fields of the cavity are the dipole, quadrupole, and skew quadrupole fields. They are localized at the coupler regions. The dipole steering results in a movement of the bunch centroid, and most importantly a differential movement of the head of the bunch relative to the tail of the bunch, the so called head-tail effect. The beam centroid movement can be corrected by use of orbit correctors. The differential movement between the head and the tail will, however, result in an (projected) emittance growth. The emittance of the beam is defined as the area of the phase space in the (x, x') plane divided by π. At each longitudinal location of the bunch, a phase space ($x(z)$, $x'(z)$) can be found. Usually the projection of these phase spaces onto the $z = z_0$ plane

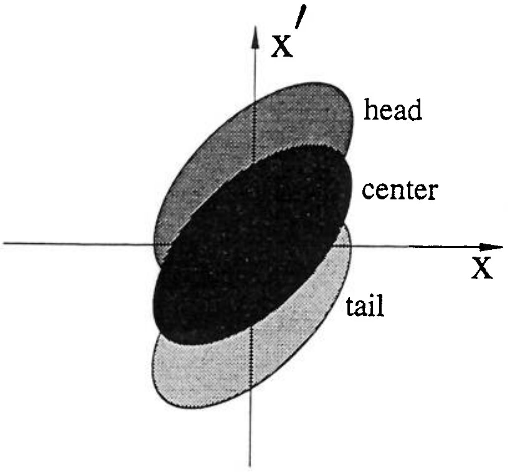

Figure 1-2: Projected emittance of the head-tail effect due to the cavity steering.

occupy the same area, where z_0 is the center of the bunch. If differential kicks are applied to different part of the beam, the resulted projected phase space would look like Fig. 1-2. The area of the phase space is increased. The head-tail effects linearly depend on the bunch length. It can be reduced by carefully arranging the orientation of the couplers of the cavities in the cryomodule. The cancellation, however relies on the gradient distribution in the cryomodules.

The $x-y$ coupling smears the x and y emittances. The force of the coupling has the form of

$$y\mathrm{x}_0 + x\mathrm{y}_0 \tag{1-2}$$

The particles with horizontal offsets will be deflected vertically and *vice versa.* The coupled emittance shows a pattern similar to Fig. 1-2. Unlike the head-tail effects, the $x-y$ coupling occurs within the same longitudinal plane.

Other effects of the cavity multipole fields include normal quadrupole focusing and azimuthal focusing. These effects do not degrade the beam quality. They only modify the β functions of the beam line, which can be adjusted by changing the focusing of the external elements.

To quantitatively study the multipole field effects, full 3-D modeling of the cavity is needed. The 3-D code MAFIA [7] is used for this purpose. Unlike the 2-D simulations, the requirement for the number of mesh points for a 3-D simulation is large. As the memory of the computer limits the maximum number of mesh points that can be used, the cavity shape will not be accurately fitted by the 3-D meshes. In such a case, the modeling should be made to represent the cavity as closely as possible. The discrepancy of the calculated cavity from the real cavity will lead to a frequency shift, which needs to be tuned back to the frequency of 1497 MHz. The local field errors caused by the unsmoothened cavity boundary will not strongly perturb the field distribution near the axis. The whole cavity model includes the 5-cells as well as the FP coupler and the HOM couplers. The different couplings between the cell to the FP coupler and the cell to the HOM coupler imbalance the fields if the two end cells are identical. A flat field distribution in the 5-cells is needed and this is accomplished by slightly adjusting the size of the two end cells. Since the code cannot model the open condition for the FP waveguide, appropriate boundary condition should be applied so that a finite domain can be defined for the problem. The length of the FP waveguide is found by finding the short position of the fundamental mode in the waveguide. Finally, the coupling strength of the FP to the end cell is found to simulate the experimental condition where the power flow in the FP coupler is 500 Watts, the gradient is 5 MV/m, and the beam current is low with negligible beam loading.

The 3-D fields calculated by use of MAFIA are Fourier decomposed in a 3-D cylindrical coordinate system. Then, the multipole fields and their impact on beam dynamics are analyzed. Experimental measurements were performed to validate the numerical modeling. The results agree with the numerical simulations. Full 3-D modelling of the CEBAF superconducting cavity is included in the beam dynamics studies in the CEBAF injector, linacs, and FEL driver linac. Head-tail and skew-coupling emittance growth under nominal operation conditions and mismatched conditions are studied.

The experimental results on the emittance growth and cavity focusing in the linacs are explainable by the numerical simulations. Methods of reducing the $x - y$ coupling are suggested.

1.3 Wakefield effects on beam dynamics

The beam-cavity interaction that generates wakefields which in turn act back on the beam is a prime concern in accelerator designs. In the design of CW linear accelerators using the latest generation of superconducting RF cavities, cost optimization and certain operational requirements favor configurations where the beam passes several times through the same accelerating structure. It has long been recognized that recirculating a beam through a linac cavity can lead to a transverse instability in which transverse displacements on successive recirculations can excite modes that further deflect the initial beam. The recirculated beam and cavities form a feedback loop that can be driven unstable at sufficiently high currents, and this effect is worsened by the higher Q's associated with modes of a superconducting RF structure. This multipass beam breakup has limited the current of early superconducting linacs such as the Stanford recyclotron [8] to currents of a few tens of microamperes. However with the improvements obtained in HOM damping through the HOM couplers, the threshold current is significantly increased. The analyses of the multipass beam breakups have been well documented in the early work of theoretical and experimental studies [9, 10, 11].

In addition to the multipass and coupled-bunch phenomena, there is a large class of single-bunch, single-pass effects which limit the peak current (more precisely, bunch charge and length) handling capabilities in storage rings and linacs. In a single pass through a RF structure, there is insufficient time for the bunch to experience the long-term ringing associated with the high Qs characteristics of superconducting cavities. Thus, these current limits are not particularly sensitive to success or failure of damping the HOM Qs. In the situation of high beam current (but lower than the threshold current), like in an FEL driver, the single-bunch, single-pass effects may worsen the machine performance.

In this dissertation, we will not address the issue of beam breakup due to wakefield effects. We will instead investigate the beam optics under the influences of both the wakefield effects and the cavity multipole-field effects in the cases of beam current that is lower than the threshold current but high enough to generate unwanted beam quality degradation. We will take a 40 MeV IR FEL driver linac as an example.

In the FEL application, the bunches do not fill up all of the RF cycles of the fundamental mode. The interbunch spacing is large. For a 25 MHz repetition frequency and a 1497 MHz RF frequency, the interbunch spacing is 12 meters. The higher frequency modes are strongly damped within the interbunch spacing and produce wakefields that act effectively only within the bunches. The effects of single bunch wakefields that concern us are the energy spread that is induced by the variation of the longitudinal wakefield across the bunch and transverse emittance degradation effects due to the dipole steering modes of the wakefields. The energy spread generated by the longitudinal wakefields may be reduced by adjusting the RF phase of the acceleration field. By doing so, the skew-coupling and head-tail effects of the cavity multipole fields will also be changed since they are functions of the RF phase. The correlation of these two kinds of effects is an issue that needs to be understood.

The evaluation of the wakefield effects relies on the correct calculation of the wakefields. Usually, wakefields are calculated under the assumption that the particles are ultrarelativistic, which is the case for high energy electrons. In some applications, this assumption may be questionable. The 40 MeV IR FEL linac, for example, has a injection energy of 10 MeV. At this energy the velocity of the electron is $0.9987c$. Other scenarios include beams with different velocities. In an earlier proposed CEBAF IR FEL, the nuclear physics beam and the FEL beam are accelerated simultaneously in the 45 MeV injector of the CEBAF accelerator. The injection energy for the physics beam is 5 MeV while for the FEL beam is 10 MeV. The β (v/c) values for these beams are 0.9948 and 0.9987 respectively. For such cases both the ultrarelativistic assumption and the slippage between the beams should be considered.

To evaluate the wakefield effects in a 40 MeV IR FEL driver linac, the wakefields for the cases of $\beta < 1$ needs to be calculated. Since the ultrarelativistic assumption and the causulity condition can not be used in such a case, analytical analysis of the high frequency wakefields is difficult. A numerical method is used to solve the Maxwell's equations in the time domain. Here, wakefield calculations are based on the code TBCI [12], which is the widely used numerical code for wakefield calculations. In order to use TBCI, several modifications have to be made. In the case of $v < c$, TBCI does not have the capacity of handling open boundary conditions for the open beam pipes. We implemented the Lindman boundary conditions to TBCI. The Lindman boundary condition optimizes the reflection coefficients of waves with different incident angles (or phase velocities). The reflection coefficients for incident angles from 1^0 to 89^0 are less than 1%. Implementing the Lindman boundary condition not only enables the code to deal with $v < c$ with proper open boundaries, it also provides a better open boundary approximation for the cases of $v = c$ than the one-dimension boundary condition, which assumes all phase velocities the speed of light, used in TBCI. For the cases of $v_t \neq v_s$, the slippage between the source and the test particles is included in the wake function integration. The integral for the wake function can only be carried out at the beam pipe radius since the problem is solved in a finite domain. A radial scaling algorithm for the wake function is needed in order to calculate the wake functions inside the beam pipe. We found that the scaling of the wake functions at different radial position can be obtained in terms of the weight function. The wake function at any radial position r is a weighted average of the wake function calculated at the pipe radius.

The smearing effect due to the low γ of the beam is studied. Conditions for applying the ultrarelativistic limit in the wake function calculation are discussed. Even though TBCI has been successful in calculating wakefields of many structures, problems are encountered in calculating the wakefields of the CEBAF cavity with very short bunch lengths. The wake functions calculated for $\sigma_z = 0.5$ mm bunch in the CEBAF five-cell cavity are obviously unphysical. It is found that the errors that cause the unphysical results are related to the truncation errors of the finite-difference algorithm that are frequency dependent. To reduce the truncation errors, a fourth-order accuracy finite-difference algorithm for solving the Maxwell's equations in the time domain is derived. The algorithm is implemented in a modified TBCI.

The modified TBCI is used for the wakefield calculations in this dissertation. Wakefields of cases of $v_s \neq v_t \neq c$ and $v_s = v_t \neq c$ are studied. If the slippage between particles is finite, the wake function seen by the test particle also slips in the frame of the source particle. In evaluating short range wakefield effects, the slippage is a important factor that needs to be included. The smearing effect is important at low energies and for short bunches. The quantity that measures the smearing effect is $R = \frac{\sigma_z \gamma}{a}$, where a is the pipe radius. Large R value corresponds to weak smearing. We found that smearing effects for $R > 1.5$ are, in general, small enough to be neglected. For example the CEBAF cavity has $a = 1.74$ cm, the R value for σ_z=3 mm and $E = 10$ MeV is 3.37, and the smearing effect is small; for $\sigma_z = 0.5$ mm and $E = 10$ MeV, R=0.65, and the smearing effect is strong.

The combined effects of the wakefields and the cavity multipole fields are studied in a 40 MeV IR FEL linac. The energy spread and the emittance growth due to the head-tail effects of the steering fields and the $x - y$ coupling of the cavity fields are evaluated. The energy spread compensation through the RF phasing and emittance behavior at off crest phase is studied.

Chapter 2

Numerical Simulation of the CEBAF 5-Cell Cavity

The CEBAF 5-cell superconducting cavity has five cylindrical symmetric cells and two end-couplers as shown in Fig. 2-3. One of the two couplers is the fundamental-power(FP) coupler which couples the RF power to the cavity. The other one is the higher-order-mode (HOM) coupler which is designed to couple the higher-order-mode fields, generated by the beam, to a RF power dump[14]. FP and HOM couplers do not have cylindrical symmetry. These asymmetric structures generate asymmetric fields in their adjacent regions, and the transverse fields on the axis are no longer zero. The particles will be deflected by these fields when passing through the cavity. A detail study of the field distributions in the CEBAF 5-cell cavity is presented in this chapter.

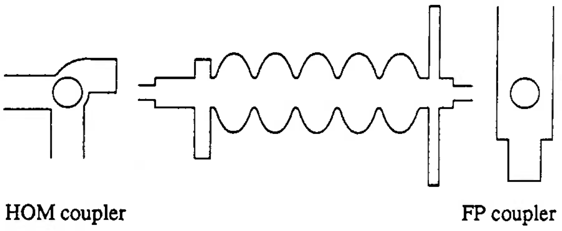

Figure 2-3: The CEBAF 5-cell cavity and the HOM and FP couplers.

The field of the CEBAF five-cell cavity is calculated by use of the 3-D code MAFIA [7]. To solve the Maxwell's equations, MAFIA uses 3-D cuboid meshes to discretize the problem. The boundary of the cavity is replaced by a number of discrete mesh points. The accuracy of reproducing the real boundary of the cavity is limited by the mesh size. Small mesh size is good for both fitting the curvature of the cavity and reducing the numerical error in the calculation. But the use of small meshes requires a large number of mesh points, which is limited by the computer memory. The cavity is not a isolated structure. It is connected with other cavities or structures by beam pipes and RF waveguides. A finite computational domain should be established to include only the cavity and part of the beam pipes and the waveguides, and appropriate boundary conditions should be applied to each side of the domain to simulate the unbounded structure. The version of MAFIA used in our calculations, however, can only deal with two kinds of boundary conditions; closed boundary (or the **E** boundary), $E_t = 0$ on the boundary, and open boundary condition (or the **H** boundary), $H_t = 0$ on the boundary. The fields that of interest are those of the fundamental mode. The frequency of this mode is 1497 MHz. The beam pipes and the HOM couplers have higher cutoff frequencies than 1497 MHz. The fundamental mode exponentially damps in these structures. These structures can be terminated at a position where the fields of the fundamental mode is negligible, so that **E** boundary condition can be applied.

The cutoff frequency of the 3.5 cm beam pipe is $\omega_c = 3281$ MHz which has a wave number $k_{3.5} = 68.71$. The cutoff frequency of the 1.74 cm beam pipe is 6599 MHz which has a wave number $k_{1.74} = 138.22$. The fundamental mode has a wave number $k_0 = 31.35$. On the HOM side, the 3.5 cm radius beam pipe, 13.932 cm long, is attached by the 1.74 cm radius beam pipe. The beam pipe is terminated at 12.5 cm from the end of the left cell. The fields of the fundamental mode are damped to $e^{-\sqrt{k_{3.5}^2 - k_0^2} \times 0.125} = 4.8 \times 10^{-4}$, which is small so that **E** boundary can be used. On the FP side, the 3.5 cm beam pipe is 3.37 cm long, and at the end of this pipe, the 1.74 cm beam pipe is attached. The beam pipe is terminated 12.5 cm away from the end cell, and the fundamental mode damps to $e^{-\sqrt{k_{3.5}^2 - k_0^2} \times 0.0337 - \sqrt{k - 1.74^2 - k_0^2} \times 0.0468} = 2.3 \times 10^{-4}$, which is also small enough to place the E boundary condition. In a cavity-pair, the space between the two adjacent end-cells of the cavities is 25 cm. Since the fields at the center of this beam pipe are small, there is essentially no interference between the two cavities for the fundamental mode. The modeling has the effective field region extended to 12.5 cm on each side of the cavity. The total length of the cavity is 75 cm. The actual computational region is chosen to be a little bit larger than 75 cm since the **E** and the **H** fields are not all defined at the mesh points.

The transverse dimension of the cavity is determined by the length of the couplers. The HOM coupler has a dimension of 7.899 cm×3.81 cm. The cutoff frequency of the coupler is 1898 MHz, which has a wave number of $k_{HOM} = 39.75$. If we terminate the HOM coupler at a length of 15.5 cm, the fundamental mode would damp to $e^{-\sqrt{k_{HOM}^2-k_0^2}\times 0.155} = 2.26 \times 10^{-2}$. If the **E** boundary condition is applied at this point, an error with this strength will be reflected back to the pipe region. Since the error also damps in the coupler, when it reaches the pipe region, the strength is reduced to the order of 5×10^{-4}, which is small and can be ignored. So, even if the HOM coupler can not damp the fields to a very small number at the termination, the error due to the enforced **E** boundary condition is considerably smaller. This is desirable so that a small computational region can be used. The length of the HOM coupler is chosen to be 15.5 cm.

The FP coupler is a 13.44 cm×2.5 cm rectangular structure. At one end, it is connected by a 7.899 cm×2.5 cm adapter. The adapter has a length of 9.65 cm and is terminated by metal material. The position where the adapter is connected is called stub position. This position determines the coupling between the cavity and the coupler. The other end of the FP coupler is connected to the power supply system (recirculator and klystron) through a waveguide. The fundamental wave propagates in the coupler in the form of a T_{10} mode. The fields do not damp in the FP coupler. Since the cavity has very high Q, the position of the termination of the coupler is not important as long as we only study the fields in the cavity region. It is important when the fields in the coupler-pipe region are of interest, which is the case of this work. So the length of the FP coupler should be chosen carefully. The idea is to find the position of the standing wave minimum. At that position, the **E** field has minimum value, ideally zero, and the **E** boundary condition can be applied. Since the wavelength of the fundamental mode is 20 cm in free space and 30 cm in the propagation direction of the FP coupler, the length of the termination is roughly estimated to be in the range of 20-30 cm. The termination of the FP coupler will be discussed in a later section.

The cross section of the cells is approximately elliptical. The three center cells are identical, with a major axis of 9.4 cm and a minor axis of 5 cm. The two end cells are slightly smaller than those center cells in order to have flat field distribution.

With the computational domain determined as above, the whole region is discretized in 3-D Cartesian coordinates with an average mesh size of 4 mm. The number of mesh points is about 1.3 million. Even with this mesh size, the elliptical shape cavity and cylindrical beam pipes cannot be perfectly fitted. This causes the volume of the cavity be slightly changed, which results in a frequency shift. The flat field distribution in the five cells can no longer be held due to the change of coupling between the cells. The coupling between the cavity and the coupler will also be changed. Since the field strength in the coupler region is directly related to the coupling strength and the gradient of the cavity, it is important to obtain the right coupling in order to study coupler steering effects.

The frequency shift and the flat field distribution can be tuned to the designed values by carefully maneuvering the shape of the cells. The right FP coupling strength can be obtained by adjusting the stub position. In the next sections, we will study how the boundary perturbations can be used for these adjustments.

2.1 The theory of resonant cavities

We wish to solve the Maxwell's equations within a volume bounded by certain surfaces.

$$\nabla \times \mathbf{E} + \frac{\partial \mathbf{B}}{\partial t} = 0 \tag{2-3}$$

$$\nabla \times \mathbf{H} - \frac{\partial \mathbf{D}}{\partial t} = \mathbf{J} \tag{2-4}$$

$$\nabla \cdot \mathbf{D} = \rho \tag{2-5}$$

$$\nabla \cdot \mathbf{B} = 0 \tag{2-6}$$

The solution will be in terms of a summation over certain modes, which possess orthogonality properties. To do that, we would like to find the orthogonal functions which satisfy certain boundary conditions. The electric and magnetic fields can be expanded in terms of these functions. The theoretical studies of resonant cavities presented in this chapter follow the treatment of Slater [15].

2.1.1 Orthogonal functions

Consider an arbitrarily shaped cavity with one opening as shown in Fig. 2-4. The surface is divided into two parts labeled S and S'. We will impose the short-circuited boundary condition on S, which requires that the tangential component of $\mathbf{E}$ and the normal component of $\mathbf{H}$ be zero, and the open-circuited boundary condition on S', which requires that the normal component of $\mathbf{E}$ and tangential component of $\mathbf{H}$ be zero. The spanning orthogonal functions can be found by solving the source free Maxwell's equations under these boundary conditions.

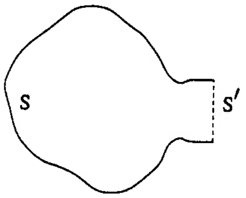

Figure 2-4: Cavity with one opening.

In general, there are two kinds of vector fields, the solenoidal, with zero divergence, and the irrotational, with zero curl. Let $\mathbf{E}_a$ and $\mathbf{H}_a$ be the orthogonal functions of the solenoidal fields and $\mathbf{F}_a$ be the orthogonal function of the irrotational fields. We will use $\mathbf{E}_a$ to expand the solenoidal part of $\mathbf{E}$, $\mathbf{F}_a$ to expand the irrotational part of E and use $\mathbf{H}_a$ to expand $\mathbf{H}$. $\mathbf{E}_a$, $\mathbf{H}_a$ and $\mathbf{F}_a$ satisfy the following boundary conditions

$$\mathbf{n} \times \mathbf{E}_a = 0 \text{ on } S, \quad \mathbf{n} \cdot \mathbf{E}_a = 0 \text{ on } S' \qquad (2-7)$$

$$\mathbf{n} \times \mathbf{H}_a = 0 \text{ on } S', \quad \mathbf{n} \cdot \mathbf{H}_a = 0 \text{ on } S \qquad (2-8)$$

$$\begin{aligned} \mathbf{n} \times \mathbf{F}_a &= 0 \text{ on } S \text{ and } S' \\ \psi_a &= 0 \text{ on } S \text{ and } S' \end{aligned} \qquad (2\text{-}9)$$

where k_a is the wave number, $\nabla\psi_a = k_a\mathbf{F}_a$. Assume $\mathbf{E}_a$ and $\mathbf{H}_a$ satisfy the following relation

$$k_a\mathbf{E}_a = \nabla \times \mathbf{H}_a, \quad k_a\mathbf{H}_a = \nabla \times \mathbf{E}_a \qquad (2-10)$$

$\mathbf{H}_a$ is the magnetic field scaled by $\sqrt{\mu/\epsilon}$. $\mathbf{E}_a$, $\mathbf{H}_a$ and ψ_a satisfy the wave equation

$$\nabla^2\mathbf{E}_a + k_a^2\mathbf{E}_a = 0 \qquad (2\text{-}11)$$

$$\nabla^2\mathbf{H}_a + k_a^2\mathbf{H}_a = 0 \qquad (2\text{-}12)$$

$$\nabla^2\psi_a + k_a^2\psi_a = 0 \qquad (2\text{-}13)$$

The $\mathbf{E}_a$s, $\mathbf{H}_a$s and $\mathbf{F}_a$s are normalized and readily shown to be orthogonal.

2.1.2 Maxwell's equations in a cavity

To solve the Maxwell's equations in a hollow cavity, the fields are expanded in terms of the orthogonal functions described in Sec. (2.1.1).

$$\mathbf{E} = \sum_a \left(\mathbf{E}_a \int \mathbf{E} \cdot \mathbf{E}_a dv + \mathbf{F}_a \int \mathbf{F} \cdot \mathbf{F}_a dv\right)$$

$$\begin{aligned}
\mathbf{H} &= \sum_a \mathbf{H}_a \int \mathbf{H}\cdot\mathbf{H}_a dv \\
\mathbf{J} &= \sum_a \left(\mathbf{J}_a \int \mathbf{E}\cdot\mathbf{E}_a dv + \mathbf{F}_a \int \mathbf{J}\cdot\mathbf{F}_a dv\right) \\
\rho &= \sum_a \psi_a \int \rho\psi_a dv
\end{aligned} \qquad (2\text{-}14)$$

Substituting (2-14) into Eq. (2-3) - (2-6) we have the following equations for the expansion coeficients

$$k_a \int \mathbf{E}\cdot\mathbf{E}_a + \mu\frac{d}{dt}\int \mathbf{H}\cdot\mathbf{H}_a dv = -\int_S (\mathrm{n}\times\mathbf{E})\cdot\mathbf{H}_a da \qquad (2-15)$$

$$k_a \int \mathbf{H}\cdot\mathbf{H}_a - \epsilon\frac{d}{dt}\int \mathbf{E}\cdot\mathbf{E}_a dv = \int \mathbf{J}\cdot\mathbf{E}_a dv - \int_{S'} (\mathrm{n}\times\mathbf{H})\cdot\mathbf{E}_a da \qquad (2-16)$$

$$-\epsilon\frac{d}{dt}\int \mathbf{E}\cdot\mathbf{F}_a dv = \int \mathbf{J}\cdot\mathbf{F}_a dv \qquad (2-17)$$

$$-k_a\epsilon\int \mathbf{E}\cdot\mathbf{F}_a dv = \int \rho\cdot\psi_a dv \qquad (2-18)$$

$\mathbf{B}$ is a solenoidal vector, so $\nabla\cdot\mathbf{B} = 0$ is automatically satisfied.

Among these equations, Eqs. (2-15) and (2-16) determine the solenoidal part of the fields. This is the part of the fields which shows the properties of wave propagation. We can combine Eqs. (2-15) and (2-16) to get separate equations for the coefficients $\int \mathbf{E}\cdot\mathbf{E}_a dv$ and $\int \mathbf{H}\cdot\mathbf{H}_a dv$

$$\begin{aligned}
\epsilon\mu\frac{d^2}{dt^2}\int \mathbf{E}\cdot\mathbf{E}_a dv + k_a^2\int \mathbf{E}\cdot\mathbf{E}_a dv &= -\mu\frac{d}{dt}\left(\int \mathbf{J}\cdot\mathbf{E}_a dv\right. \\
\left.-\int_{S'} (\mathrm{n}\times\mathbf{H})\cdot\mathbf{E}_a da\right) &- k_a\int_S (\mathrm{n}\times\mathbf{E})\cdot\mathbf{H}_a da
\end{aligned} \qquad (2\text{-}19)$$

$$\begin{aligned}
\epsilon\mu\frac{d^2}{dt^2}\int \mathbf{H}\cdot\mathbf{H}_a dv + k_a^2\int \mathbf{H}\cdot\mathbf{H}_a dv &= k_a\left(\int \mathbf{J}\cdot\mathbf{E}_a dv\right. \\
\left.-\int_{S'} (\mathrm{n}\times\mathbf{H})\cdot\mathbf{E}_a da\right) &- \epsilon\frac{d}{dt}\int_S (\mathrm{n}\times\mathbf{E})\cdot\mathbf{H}_a da
\end{aligned} \qquad (2\text{-}20)$$

$\int \mathbf{E}\cdot\mathbf{E}_a dv$ and $\int \mathbf{H}\cdot\mathbf{H}_a dv$ are functions of time. They satisfy the differential equation of a forced harmonic oscillation. The driving forces are the current in the cavity and the current on the cavity wall.

2.2 Frequency adjustment by means of boundary perturbation

Discretization of the cavity with finite mesh size in the MAFIA simulations will inevitably shift the frequency of the cavity away from the design value. Initial calculation of the CEBAF cavity shows that the resonant frequency of the fundamental mode is 1487.15 MHz which is 10 MHz lower than the designed value of 1497 MHz. It is preferable to adjust the resonant frequency to be as close as possible to 1497 MHz, as this allows beam dynamics codes to use one frequency for the capture, the buncher, and the cavities. In this section we will use the formulae developed in Sec. 2.1 to study the tuning of the frequency in MAFIA simulation. Let us estimate the frequency change when the boundary of the cavity is perturbed by pushing a small part of the wall in or out. Let the cavity wall be superconducting and $\mathbf{J} = 0$ inside the cavity. Let the wall be pushed into the cavity volume by a small amount. In the region between the original wall and the perturbed one, **E** and **H** will be zero. This is equivalent to having a surface current causing the discontinuity in the tangential component of **H**. A surface integral term $-\int(\mathbf{n}\times\mathbf{H})\cdot\mathbf{E}_a da$ needs to be added to the right hand side of Eqs. (2-19) and (2-20); that is

$$\begin{aligned}
-\int(\mathbf{n}\times\mathbf{H})\cdot\mathbf{E}_a da' &= -\int(\mathbf{n}\times\mathbf{H}_a)\cdot\mathbf{E}_a da'\int\mathbf{H}\cdot\mathbf{H}_a dv \\
&= -\int\mathbf{n}\cdot(\mathbf{E}_a\times\mathbf{H}_a)da'\int\mathbf{H}\cdot\mathbf{H}_a dv \\
&= -\int(\mathbf{H}_a\cdot(\nabla\times\mathbf{E}_a)-\mathbf{E}_a\cdot(\nabla\times\mathbf{H}_a))dv'\int\mathbf{H}\cdot\mathbf{H}_a dv \\
&= -k_a\int\mathbf{H}\cdot\mathbf{H}_a dv\int(H_a^2-E_a^2)dv' \qquad (2\text{-}21)
\end{aligned}$$

where a' and v' are the small surface and the corresponding volume of perturbation. Combine (2-21) with (2-20) we have

$$-\epsilon\mu\omega^2 + k_a^2 = -k_a^2\int(H_a^2 - E_a^2)dv' \qquad (2-22)$$

or

$$\omega^2 = \omega_a^2\left(1+\int(H_a^2 - E_a^2)dv'\right) \qquad (2-23)$$

This formula indicates that the frequency of the cavity will increase if the wall is pushed in at where the magnetic field is strong or is pulled out at where the electric field is strong. The initial calculation shows that for the fundamental mode the electric field is strong in the pipe region of the cavity whereas the magnetic field is strong at the top of the cells. It is preferred to adjust the top part of the cells inward to increase the frequency, since the perturbation then is far from the beam axis and the fields in the axis region are not perturbed. Several calculations have been made for different cell radii. The final result has a frequency of 1495.37 MHz which is fairly close to the designed value 1497 MHz. To obtain this frequency, the radii of the cells are reduced by about 1.8 mm.

2.3 Field distribution in multi-cell cavities

The initial calculation shows that the amplitude of the fields in the five cells of the cavity is not the same. This deviation is due to errors in the coupling of the end cells. In actual operation, the cavities have a field flatness of ±2.5% in the five cells.

In multi-cell cavities, the cells are coupled to each other. The coupling strengths between the cells determine the field distribution. The inner cells of the cavity are coupled to both the adjacent cells on each side whereas the end cells of the cavity are each coupled to one cell on one side and a coupler on the other side. For high Q cavities, like the CEBAF cavity, the coupler-cell coupling is much smaller than the cell-cell coupling. Let us examine the relation between the fields strength and the coupling

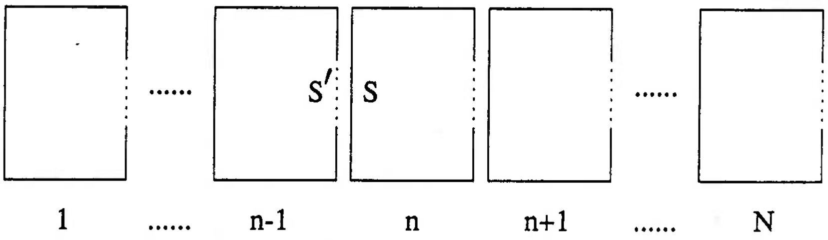

Figure 2-5: Multi-cell cavity.

strength in multi-cell cavities [16] as shown in Fig. 2-5. Consider cell n, which is coupled with cells (n-1) and (n+1). We arrange the cells so that the (n-1)th cell couples to the nth cell through its S' boundary and the (n+1)th cell couples to the nth cell through its S boundary. Let X_n represent the coefficient $\int \mathbf{E} \cdot \mathbf{E}_a dv$ of cell n. Apply equation (2-19) to the nth cell

$$\begin{aligned} \epsilon\mu \frac{d^2}{dt^2} X_n + k_a^2 X_n &= j\sqrt{\epsilon\mu}\frac{d}{dt}\int_{S'} (\mathbf{n} \times \mathbf{H}^{n+1}) \cdot \mathbf{E}_a^n X_{n+1} da \\ &- k_a \int_S (\mathbf{n} \times \mathbf{E}^{n-1}) \cdot \mathbf{H}_a^n X_{n-1} da \qquad (2\text{-}24) \end{aligned}$$

Recalling that X_n has an $e^{j\omega t}$ dependence, the coupled equations, in general, have the form

$$X_n(\omega^2 - \omega_0^2) + \frac{C\omega^2}{2}(X_{n-1} + X_{n+1}) = 0 \qquad (2-25)$$

where C is the coupling strength and is a function of ω. The end cells, e.g. n=0, only couple to one of the inner cells. The coupling equation is then

$$X_0(\omega^2 - \omega_{01}^2) + \frac{C\omega^2}{2} X_1 = 0 \qquad (2-26)$$

where ω is the overall frequency of the cavity, ω_0 and ω_{01} are the intrinsic frequencies of the inner cells and the end cells respectively. If $\omega_0 = \omega_{01}$, the coupling for the inner cells is about twice as large as that of the end cells. The coupling of the end cells can be compensated by adjusting the intrinsic frequency ω_{01}. Assuming that the couplings are the same, the solutions of Eqs. (2-25) and (2-26) are as follows,

$$\begin{aligned} X_n^{(q)} &= \cos(\frac{\pi q n}{N}) e^{j\omega_q t} \qquad (2\text{-}27) \\ \omega_q^2 &= \frac{\omega_0^2}{1 + C\cos(\pi q/N)} \qquad (2\text{-}28) \end{aligned}$$

where q =0,1,2,...N, with N the total number of cells. For q =N, the field distribution in the cavity has π mode pattern. The CEBAF cavity has N=4 and operates in the π mode. The coupling between the cells of a CEBAF cavity is an E coupling. The coupling strength is positive; $\omega^q > \omega_0$ for π mode.

In the π mode, $X_n = -X_{n+1}$. Eq. (2-25) then becomes

$$X_n(\omega^2 - \omega_0^2) + C\omega^2 X_{n+1} = 0 \qquad (2-29)$$

Comparing with (2-26), we see if the end-cell coupling is to be the same as the inner-cell coupling, one has

$$\omega_{01} = 0.5 \times (\omega^q + \omega_0) \qquad (2-30)$$

The intrinsic frequency of the end cell must be higher that the intrinsic frequency of the inner cells in order to have the same coupling. The field flatness adjustment thus becomes possible by tuning the frequency of individual cells.

The method used in Sec. 2.2 for tuning the overall frequency of the cavity can be applied to the end cells. The tuning process is now more subtle. Since the coupling between the end cell and the HOM coupler is not the same as the coupling between the end cell and the FP coupler, the two end cells must have slightly different sizes. We would like to make a slight change of the boundary cells to adjust the volume without changing their material properties (vacuum to metal, for example) by slightly changing the radius of the cavity or the position of the mesh lines. The result often comes out just the opposite; in discretizing the cavity, the mesh on the curved boundary of the cavity may be cut off to become vacuum or be kept as metal depending on what percentage of the cell is within the boundary of the cavity. Slightly changing the mesh lines may turn some of the vacuum mesh into metal or *vice versa*, leading to excessive volume increment or reduction. Care must be taken and many tries were needed for the tuning. Our final result has a ±2.5% field deviation in the five cells which is about the value achievable in accelerator operation.

2.4 The short position of the fundamental power waveguide

As stated earlier, the fundamental mode propagates in the fundamental power waveguide. The termination of the guide is not arbitrary, and we need to find the position where **E** field is minimum so that the waveguide can be terminated by a metal boundary. The position of minimal **E** field is called the short position. To find this position, we will start with the input impedance of the cavity, then couple the cavity impedance to a terminated waveguide impedance. We will find the frequency change of the system as a function of the termination position of the waveguide, from which the short position will be determined.

2.4.1 The input impedance of the cavity

Consider a cavity attached to a waveguide. S' is the plane where the open circuit boundary is applied to get the normal modes $\mathbf{E}_a$ and $\mathbf{H}_a$. The S' plane is chosen far enough up the waveguide from the cavity so that only propagating modes exist. On S' we will add a perturbation **H**. We will calculate the **E** field distribution under this perturbation in the cavity and the waveguide. We will take the ratio of the **E** and the **H** fields on S' to get the input impedance of the cavity.

$\mathbf{E}_a$ and the perturbation **H** on the S' plane can be expanded in terms of the waveguide mode $\mathbf{E}_{tn}$ and $\mathbf{H}_{tn}$

$$\mathbf{E}_a = \sum_n v_{an}\mathbf{E}_{tn} \qquad (2-31)$$

$$\mathbf{H} = \sum_n i_n Z_{1n}\mathbf{H}_{tn} \qquad (2-32)$$

where v_{an} and i_n are coefficients; v_{an} is independent of time while i_n varies as $e^{j\omega t}$, the time dependence of **H**, Z_{1n} is the characteristic impedance of the waveguide which is defined as $Z_{1n}\mathbf{H}_{tn} = \mathbf{k} \times \mathbf{E}_{tn}$; **k** here is the propagating vector pointing into the cavity. The unit vector of S' points outward. We have $\mathbf{n} \times \mathbf{H} = \sum_n i_n \mathbf{E}_{tn}$. The second integral in (2-19) can be evaluated as

$$\begin{aligned}\int_{S'} (\mathbf{n} \times \mathbf{H}) \cdot \mathbf{E}_a da &= \int_{S'} \sum_n i_n Z_{1n}(\mathbf{n} \times \mathbf{H}_{tn}) \cdot \mathbf{E}_a da \\ &= \int_{S'} \sum_n i_n \mathbf{E}_{tn} \cdot \sum_m v_{am}\mathbf{E}_{tm} da\end{aligned}$$

$$= \sum_n i_n v_{an} \tag{2-33}$$

For a superconducting hollow cavity, Eq. (2-19) yields

$$\int \mathbf{E}\cdot\mathbf{E}_a dv = \frac{i\mu\omega \sum_n i_n v_{an}}{-\epsilon\mu(\omega^2-\omega_a^2)} = \sum_n \frac{i_n v_{an}/\epsilon\omega_a}{j\left(\frac{\omega}{\omega_a}-\frac{\omega_a}{\omega}\right)} \tag{2 - 34}$$

The transverse **E** field on S' is

$$\begin{aligned}\mathbf{E}_t &= \sum_a \left(\int \mathbf{E}\cdot\mathbf{E}_a da\right)\mathbf{E}_a \\ &= \sum_n \left(\sum_m i_m \left(\sum_a \frac{v_{an}v_{am}/\epsilon\omega_a}{j\left(\frac{\omega}{\omega_a}-\frac{\omega_a}{\omega}\right)}\right)\right)\mathbf{E}_{tn} \\ &= \sum_n V_n \mathbf{E}_{tn} \end{aligned} \tag{2-35}$$

For the nth mode

$$\begin{aligned}(\mathbf{E}_t)_n &= V_n\mathbf{E}_{tn} \\ (\mathbf{H}_t)_n &= i_n Z_{1n}\mathbf{H}_{tn}\end{aligned}$$

The impedance for the nth mode Z_n is

$$\begin{aligned} Z_n &= \frac{\mathbf{k}\times(\mathbf{E}_t)_n}{(\mathbf{H}_t)_n} = \frac{V_n}{i_n} \\ &= \frac{1}{i_n}\sum_m i_m \sum_a \frac{v_{an}v_{am}/\epsilon\omega_a}{j\left(\frac{\omega}{\omega_a}-\frac{\omega_a}{\omega}\right)} \\ &= \frac{1}{i_n}\sum_m i_m Z_{nm} \end{aligned} \tag{2-36}$$

where Z_{nm} can be interpreted as the coupling impedance between mode n and mode m, $i_m Z_{nm}$ as the voltage contributed from mode m to mode n. The total voltage of mode n takes the summation over all of the waveguide modes. Eq. (2-36) gives the impedance looking into the cavity. The impedance looking out of the cavity is the negative of Z_n since **k** now is pointing outward, which leads to $\mathbf{n}\times\mathbf{H} = -\sum_n i_n\mathbf{E}_t$.

Assume that only the dominant mode propagates in the waveguide and define $1/Q_{ext,a1} = v_{a1}^2/\epsilon\omega_a Z_{01}$, where Z_{01} is the characteristic impedance of the guide for its dominant mode at the resonant frequency ω_a. The impedance has only the Z_{11} term, which is

$$Z_n = Z_{11} = Z_{01} \sum_a \frac{1/Q_{ext,a1}}{j\left(\frac{\omega}{\omega_a} - \frac{\omega_a}{\omega}\right)} \qquad (2-37)$$

$Q_{ext,a1}$ is a measure of coupling of the ath mode to the output through the dominant mode of the guide. If v_{a1} is large, the coupling is strong, and $Q_{ext,a1}$ is small.

2.4.2 The short position of the coupler

Let us now connect a terminated waveguide to the open surface S' of the cavity. The length of the guide is d. The impedance looking into the guide is

$$Z_{guide} = jZ_{01} \tan 2\pi d/\lambda_g \qquad (2-38)$$

where λ_g is the guide wavelength. This impedance must be the negative of Z_{11} of (2-37)

$$\tan \frac{2\pi d}{\lambda_g} = \sum_a \frac{1/Q_{ext,a1}}{\left(\frac{\omega}{\omega_a} - \frac{\omega_a}{\omega}\right)} \qquad (2-39)$$

or

$$d = \frac{\lambda_g}{2\pi} \tan^{-1} \sum_a \frac{1/Q_{ext,a1}}{\left(\frac{\omega}{\omega_a} - \frac{\omega_a}{\omega}\right)} + \frac{1}{2} n \lambda_g \qquad (2-40)$$

This gives a relation between d and ω (or λ_g). The curves determined by Eq. (2-40) are illustrated in Fig. 2-6. Far from the resonant frequency, the term associated with the summation over a in Eq. (2-40) is small, $d \approx n\lambda_g/2$, this gives the part of the curves close to the dashed lines. As the frequency goes through a resonant frequency, the dominant term in the summation, $Q_{ext,a}/(\omega/\omega_a - \omega_a/\omega)$, goes to infinity and changes sign; d increases by $\lambda_g/2$, and the curve crosses from one of the straight lines ($n\lambda_g/2$) to the next ($(n+1)\lambda_g/2$). A resonance occurs at approximately $d = (n + 1/2)\lambda_g/2$. In the case of the cavity on resonance, the electric field at the short position forms a standing wave minimum. The field in the waveguide is, in general, much smaller than the field

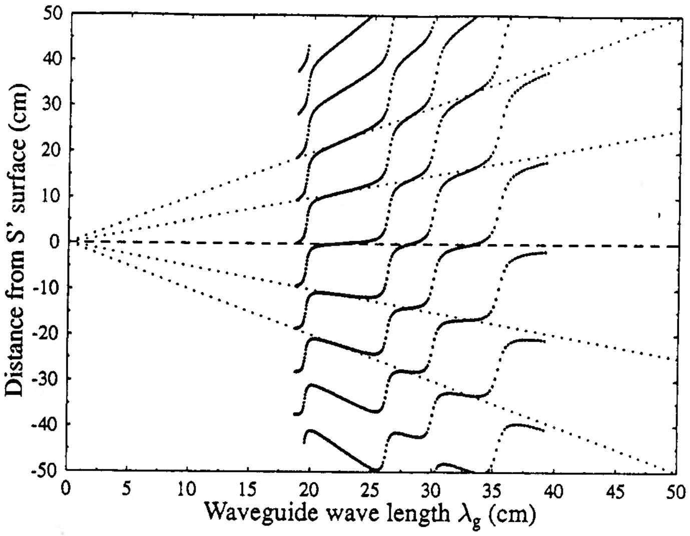

Figure 2-6: Frequency of the cavity *vs.* the short position d

in the cavity; a change of the short position has the least effect on the frequency. This corresponds to the vertical part of the curve. As the short moves farther away from the resonant position, the cavity is driven off resonance, and the field in the guide is comparably large. A change of the short position dramatically changes the frequency, which is shown as the straight part of the curves that coincide with $d = n\lambda_g/2$. In such case, the cavity is detuned.

2.4.3 The tuning curve of the CEBAF cavity

The tuning curves of the CEBAF cavity are obtained by running MAFIA at different coupler lengths. Five low frequency modes are shown in Fig. 2-7. The center curve corresponds to a resonant frequency of about 1497 MHz, which is the operating mode of the CEBAF cavity. The distance in the figure is measured from the axis of the cavity. The cavity is detuned for this mode if the short is placed at a distance of about 14 cm. The TE_{10} waveguide wavelength for 1497 MHz is 29.93 cm. Based on the above analysis, the short position for the cavity on resonance is at $d = 21.5$ cm.

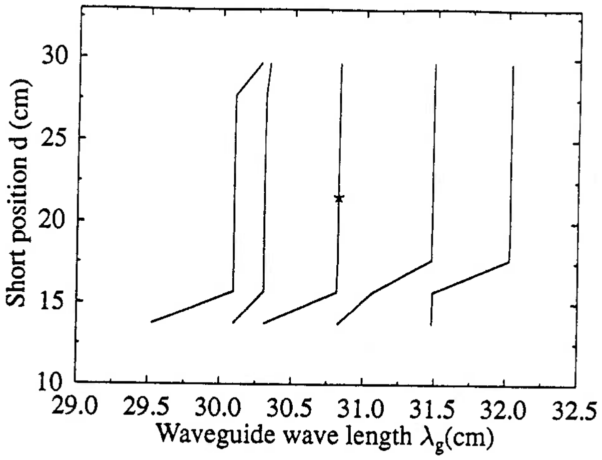

Figure 2-7: Tuning curve of the CEBAF cavity.

2.5 Numerical tuning of the coupling strength of the FP coupler

The coupling between the cavity and the waveguide determines the power flow as well as the field strength in the coupler region. The coupling strength is important in cavity steering studies. The finite mesh used in the simulation changes the coupling between the end cell and the FP coupler. To match the experimental condition of 5 MV/m gradient and 500 Watt input power (low beam current), the coupling must be adjusted. The tuning of the coupling strength can be accomplished by adjusting the stub position of the FP coupler.

The coupling is characterized by the external Q_{ext}, which is defined as the ratio of the energy stored in the cavity and the power flow in the coupler. For our purpose, Q_{ext} is not needed to be calculated, instead, we only need to know the ratio of the amplitude of the field in the waveguide and the field in the cavity. The FP waveguide is a rectangular structure. The dimension of the guide is (a=13.44cm × b=2.502cm). The cutoff frequency is $\omega_\lambda = \pi c/a = 2\pi \times 1.12 \times 10^9$. Assuming that the traveling wave in the waveguide is TE_{10} mode. From [17], the power flow in the waveguide is

$$P = \frac{c\mu}{2}\left(\frac{\omega}{\omega_\lambda}\right)\left(1 - \left(\frac{\omega_\lambda}{\omega}\right)^2\right)^{1/2} \int_A \psi^* \psi da \qquad (2-41)$$

where for TE mode $\psi = H_z = H_0 \cos(\pi x/a) e^{jk_z z - j\omega t}$. Integrate over the waveguide surface A we have

$$P = \frac{abH_0^2 c\mu}{4}\left(\frac{\omega}{\omega_\lambda}\right)\left(1-\left(\frac{\omega_\lambda}{\omega}\right)^2\right)^{1/2} \qquad (2-42)$$

The relations

$$\mathbf{H}_t = \frac{\pm 1}{Z}\mathbf{z_0}\times\mathbf{E}_t \qquad Z = \frac{\mu\omega}{ck} = Z_0\frac{k}{k_z} \qquad (2-43)$$

lead to

$$H_0 = \frac{1}{Z_0}\frac{\omega_\lambda}{\omega}E_{t0}$$

where $Z_0 = 376.8$ is the impedance of the vacuum and $k = \omega/c$ is the wave number. The power flow in terms of the amplitude of the electric field of the traveling wave is

$$P = \frac{abE_{t0}^2}{4Z_0}\left(1-\left(\frac{\omega_\lambda}{\omega}\right)^2\right)^{1/2} \qquad (2-44)$$

Evaluate P for the parameters given above we have

$$P = 1.4943\times 10^6 E_{t0}^2 \qquad (2-45)$$

where E_0 is in MV/m. For $P = 500$ Watt, $E_{t0} = 1.8292\times 10^{-2}$ MV/m. MAFIA output gives the amplitude of the standing wave E_{stand}. Thus $E_{stand} = 2E_{t0} = 3.6584\times 10^{-2}$ MV/m. In the cavity, to achieve a average gradient of 5 MV/m, the maximum amplitude in the center of the cells is $E_c = 1.99$ MV/m. The ratio of these two field is

$$\frac{E_{stand}}{E_c} = 1.838\times 10^{-2} \qquad (2-46)$$

The stub position of the FP coupler determines this ratio. The numerical result of this ratio versus stub position is shown in Fig. 2-8*a*. The stub position is measured from the axis. Shown in Fig. 2-8*b* is the maximum of the E_x component on the axis in the coupler region. The coupling strength has a minimum at about 11.5 cm. The coupling gets stronger if we move the stub both ways away from this point. There are two positions which have the right coupling. From the point view of cavity steering, it is preferable to place the stub farther away from the axis, as seen from Fig. 2-8*b*.

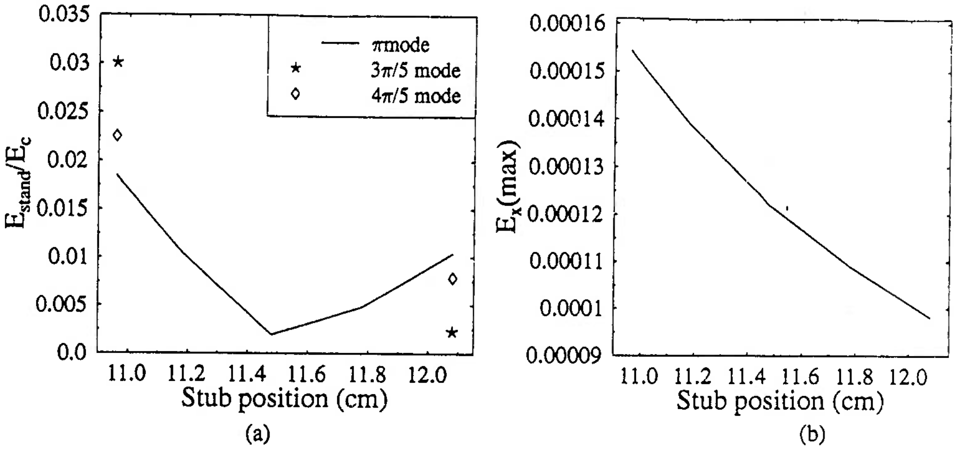

Figure 2-8: The coupling of the FP coupler *vs.* the stub position.

There is, however, another important factor need to be considered. The cavity has a few modes that have frequencies lower than the fundamental mode frequency as shown in Fig. 2-7 (only two are shown). These modes can be coupled out only through the FP coupler since the HOM coupler has higher cutoff frequency. Higher coupling strength is required for these modes. This can be obtained by placing the stub closer to the axis, as indicated in the figure. It is estimated that strong lower modes would cause greater damage to the beam than the cavity steering. It is therefore preferable to choose the stub position to be 10.96 cm. This choice more efficiently extracts the lower modes out of the cavity, even though the cavity steering is stronger.

2.6 Field distribution in the cavity

As the parameters of the cavity and the coupler are determined in the previous sections, the field of the cavity is evaluated. MAFIA solves the eigenvalue problem

$$(\nabla^2 + k^2)\mathbf{E} = 0 \qquad (2-47)$$

It first finds the eigenvalues $\{k_i\}$ (the frequencies), and then finds the eigenvector E. The frequency of the fundamental mode obtained from MAFIA for the CEBAF cavity is 1495.38 MHz. The accuracy of the numerical calculation is as the follows

$$\begin{aligned} \text{Frequency} &\rightarrow 1.0 \times 10^{-5} \\ (\nabla \cdot \mathbf{D} = 0) &\rightarrow 1.2 \times 10^{-8} \\ (\nabla \times \nabla \times \mathbf{E} = \mathbf{E}) &\rightarrow 1.3 \times 10^{-5} \\ (\nabla \cdot \mathbf{B} = 0) &\rightarrow 4.5 \times 10^{-13} \end{aligned}$$

Since there are modes that are close to each other, there is contamination among the eigenvectors. The contamination factor for our calculation is 2×10^{-3}. This factor determines the contamination of the actual vector under the worst assumption. The contamination is reasonably small. The overall accuracy of the simulation is good.

2.6.1 Multipole-field distributions, 3-D field expansion

Since the structure of the couplers is so irregular, we expect that the fields have multipole components. The multipole fields can be studied by 3-D field expansion. In a resonant cavity, the **E** and **B** fields satisfy the wave equation

$$\left(\nabla^2 + k^2\right) \begin{pmatrix} \mathbf{E} \\ \mathbf{B} \end{pmatrix} = 0 \qquad (2-48)$$

where $k = \omega/c$ is the wave number. Assuming the fields have an $e^{\pm j\zeta_z z}$ dependence, Eq. (2-48) becomes

$$\left(\nabla_\perp^2 - (\zeta_z^2 - k^2)\right) \begin{pmatrix} \mathbf{E}(r,\theta,z) \\ \mathbf{B}(r,\theta,z) \end{pmatrix} = 0 \qquad (2-49)$$

where $\nabla_\perp^2$ is the transverse Laplace operator.

TM modes:

For TM modes, the full **E** and **B** fields can be determined by $E_z(r,\theta,z)$, which satisfies

$$(\nabla_\perp^2 - (\zeta_z^2 - k^2))E_z(r,\theta,z) = 0 \qquad (2-50)$$

Let $L = 75$ cm be the total length of the cavity; $z = 0$ be the center of the cavity. $E_z(r, \theta, \pm L/2) = 0$ be the boundary condition. The general solution of (2-50) is

$$\begin{aligned} E_z &= I_m(\eta_n r)\Big(\cos(\zeta_n \cdot z)(A^E_{n,m}\sin(m\theta) + B^E_{n,m}\cos(m\theta)) \\ &\quad + \sin(\zeta_n \cdot z)(C^E_{n,m}\sin(m\theta) + D^E_{n,m}\cos(m\theta))\Big) \end{aligned} \tag{2-51}$$

where $\zeta_n = (2n-1)\pi/L$, $\eta_n^2 = \zeta_n^2 - (2\pi/\lambda)^2 > 0$, $I_m(\eta_n r)$ are the modified Bessel functions of the first kind. For $\eta_n^2 < 0$, $\eta_n = \sqrt{|\eta_n^2|}$ and $I_m(\eta_n r)$ is replace by $J_m(\eta_n r)$, the Bessel function of the first kind. The $\mathbf{E}_\perp$ and $\mathbf{H}_\perp$ are determined by the transverse derivatives of $E_z(r, \theta, z)$

$$\mathbf{E}_\perp = \pm j \frac{\zeta_n}{-\eta_n^2} \nabla_\perp E_z(r, \theta, z) \tag{2-52}$$

$$c\mathbf{B}_\perp = \frac{\pm k}{\zeta_n} \mathbf{z_0} \times \mathbf{E}_\perp \tag{2-53}$$

With the ± signs correspond to $e^{\pm j\zeta_z z}$, we have

$$(\pm j)\cos(\zeta_n z) = -\sin(\zeta_n z) \tag{2-54}$$

$$(\pm j)\sin(\zeta_n z) = \cos(\zeta_n z) \tag{2-55}$$

and the **B** field is $\pi/2$ phase ahead of the **E** field

$$e^{-(j\omega t + \pi/2)} = -j e^{-j\omega t} \tag{2 - 56}$$

The 3-D expansion of other field components are obtained. The following is a summary of the fields for the TM modes.

$$\begin{aligned} E_z &= I_m(\eta_n r)\Big(\cos(\zeta_n \cdot z)(A^E_{n,m}\sin(m\theta) + B^E_{n,m}\cos(m\theta)) \\ &\quad + \sin(\zeta_n \cdot z)(C^E_{n,m}\sin(m\theta) + D^E_{n,m}\cos(m\theta))\Big) \end{aligned} \tag{2-57}$$

$$\begin{aligned} E_r &= \frac{\zeta_n}{\eta_n^2}\frac{dI_m(\eta_n r)}{dr}\Big(\sin(\zeta_n \cdot z)(A^E_{n,m}\sin(m\theta) + B^E_{n,m}\cos(m\theta)) \\ &\quad - \cos(\zeta_n \cdot z)(C^E_{n,m}\sin(m\theta) + D^E_{n,m}\cos(m\theta))\Big) \end{aligned} \tag{2-58}$$

$$\begin{aligned}
E_\theta &= \frac{m\zeta_n}{\eta_n^2}\frac{I_m(\eta_n r)}{r}\Big(\sin(\zeta_n\cdot z)(A^E_{n,m}\cos(m\theta) - B^E_{n,m}\sin(m\theta)) \\
&\quad - \cos(\zeta_n\cdot z)(C^E_{n,m}\cos(m\theta) - D^E_{n,m}\sin(m\theta))\Big) && \text{(2-59)} \\
c\cdot B_r &= -\frac{\omega}{c\eta_n^2}\frac{mI_m(\eta_n r)}{r}\Big(\cos(\zeta_n\cdot z)(A^E_{n,m}\cos(m\theta) - B^E_{n,m}\sin(m\theta)) \\
&\quad + \sin(\zeta_n\cdot z)(C^E_{n,m}\cos(m\theta) - D^E_{n,m}\sin(m\theta))\Big) && \text{(2-60)} \\
c\cdot B_\theta &= \frac{\omega}{c\eta_n^2}\frac{dI_m(\eta_n r)}{dr}\Big(\cos(\zeta_n\cdot z)(A^E_{n,m}\sin(m\theta) + B^E_{n,m}\cos(m\theta)) \\
&\quad + \sin(\zeta_n\cdot z)(C^E_{n,m}\sin(m\theta) + D^E_{n,m}\cos(m\theta))\Big) && \text{(2-61)}
\end{aligned}$$

TE modes:

For TE modes, H_z satisfies the same equation as the E_z field in the TM modes. The 3-D expansion of the **H** field is calculated the same way as the **E** field in the TM modes. The transverse **E** field in the TE modes can be calculated from $\mathbf{B}_\perp$:

$$\mathbf{E}_\perp = -(\pm)\mathbf{z_0}\times(c\mathbf{B}_\perp) \qquad (2-62)$$

A summary of the 3-D expansion of the fields of the TE mode is listed as follows.

$$\begin{aligned}
c\cdot B_z &= I_m(\eta_n r)\Big(\cos(\zeta_n\cdot z)(A^B_{n,m}\sin(m\theta) + B^B_{n,m}\cos(m\theta)) \\
&\quad + \sin(\zeta_n\cdot z)(C^B_{n,m}\sin(m\theta) + D^B_{n,m}\cos(m\theta))\Big) && \text{(2-63)} \\
c\cdot B_r &= \frac{\zeta_n}{\eta_n^2}\frac{dI_m(\eta_n r)}{dr}\Big(\sin(\zeta_n\cdot z)(A^B_{n,m}\sin(m\theta) + B^B_{n,m}\cos(m\theta)) \\
&\quad - \cos(\zeta_n\cdot z)(C^B_{n,m}\sin(m\theta) + D^B_{n,m}\cos(m\theta))\Big) && \text{(2-64)} \\
c\cdot B_\theta &= \frac{m\zeta_n}{\eta_n^2}\frac{I_m(\eta_n r)}{r}\Big(\sin(\zeta_n\cdot z)(A^B_{n,m}\cos(m\theta) - B^B_{n,m}\sin(m\theta)) \\
&\quad - \cos(\zeta_n\cdot z)(C^B_{n,m}\cos(m\theta) - D^B_{n,m}\sin(m\theta))\Big) && \text{(2-65)} \\
E_r &= -\frac{\omega}{c\eta_n^2}\frac{mI_m(\eta_n r)}{r}\Big(\cos(\zeta_n\cdot z)(A^B_{n,m}\cos(m\theta) - B^B_{n,m}\sin(m\theta)) \\
&\quad + \sin(\zeta_n\cdot z)(C^B_{n,m}\cos(m\theta) - D^B_{n,m}\sin(m\theta))\Big) && \text{(2-66)} \\
E_\theta &= \frac{\omega}{c\eta_n^2}\frac{dI_m(\eta_n r)}{dr}\Big(\cos(\zeta_n\cdot z)(A^B_{n,m}\sin(m\theta) + B^B_{n,m}\cos(m\theta)) \\
&\quad + \sin(\zeta_n\cdot z)(C^B_{n,m}\sin(m\theta) + D^B_{n,m}\cos(m\theta))\Big) && \text{(2-67)}
\end{aligned}$$

It is found that the fundamental mode is a mixed mode. It has both TM and TE components instead of only the TM component, which is the case of without couplers. The m is the index of the angular distribution. The $m = 0$ terms are cylindrically symmetric, the $m = 1$ terms have dipole symmetry, and the $m = 2$ terms have quadrupole symmetry. The n is the index of the Fourier transform in the z direction, which determines the multipole distributions along the z axis. Individual multipole fields are obtained by summing over index n for fixed m.

The sampling points of the fields for the Fourier transform are defined on the $r = 0.5$ cm cylinder. The number of points is 291 in the z direction and 80 in the angular direction. The total number of terms for the z transform is 34, and the total number of terms for the angular transform is 5.

2.6.2 Fields of mode m=0

The m=0 mode is the acceleration mode. It has only the E_z, E_r and B_θ components. The distribution of fields at $r = 0.5$ cm are shown in Fig. 2-9 The field is normalized to 1 MeV energy gain. The E_z field has essentially the same strength in all of the five cells, as can be seen from the figure; the flatness of the E_z fields in the five cells is about $\pm 2.5\%$.

2.6.3 Dipole fields, m=1

The dipole fields are the fields of the m=1 mode. As shown in Fig. 2-10, the dipole fields are localized in the HOM and the FP coupler regions. Both the transverse and the longitudinal components of the fields have dipole moments. For the transverse fields, the non-zero components in the HOM coupler region are E_x, E_y, B_x and B_y. These fields give both x and y deflections to the charged particles. In the FP coupler region, there are only non-zero E_x and B_y fields. E_y and B_x vanish because the coupler is

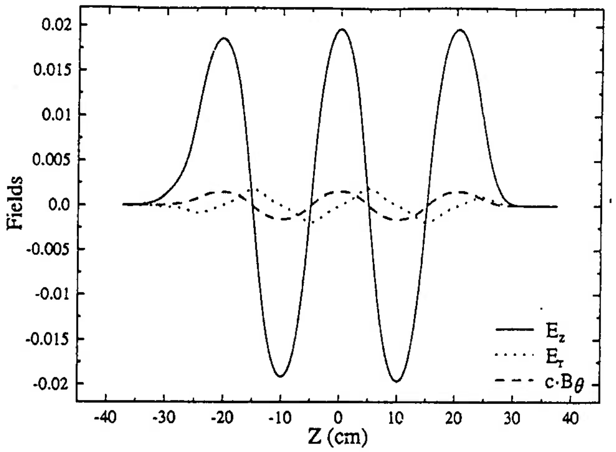

Figure 2-9: Fields of mode m=0.

symmetric about the $y = 0$ plane. The E_x and B_y fields give only x deflections, and $c \cdot B_\perp$ is larger than $E_\perp$. The steering effect in the x direction is therefore to be stronger than that in the y direction. The dipole strength of B_z is small. The dipole strength of E_z is comparable to the dipole strength of E_r. The effect of this dipole E_z field is to generate energy spread as the particles are accelerated at different azimuthal positions. Comparing the strength and the extent of the field region with the m=0 mode, this effect is small and can be ignored.

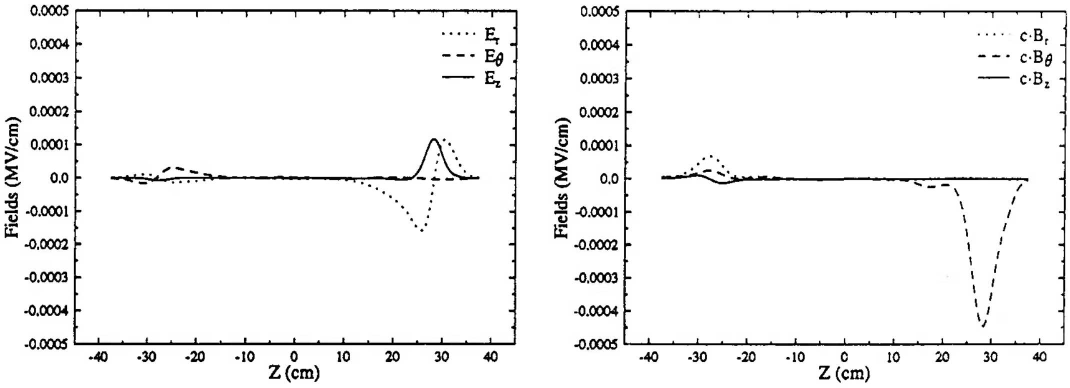

Figure 2-10: Fields of mode m=1.

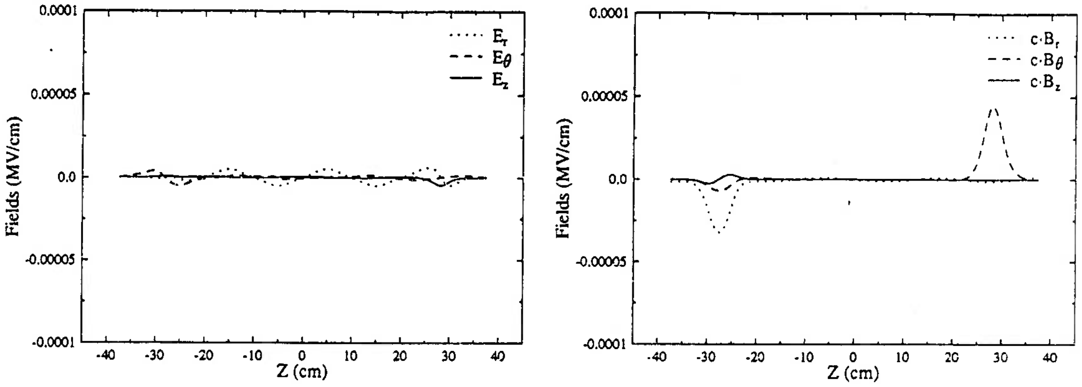

Figure 2-11: Fields of mode m=2.

2.6.4 Quadrupole fields, m=2

The quadrupole fields are related to the m=2 mode. Fig. 2-11 shows the quadrupole strength of the **E** and **B** fields at (r = 0.5 cm,θ = 0). The quadrupole effects are mainly contributed from the $B_\perp$ fields. The strength of $c \cdot B_\theta$ in the figure represents the strength of the normal quadrupole and $c \cdot B_r$ represents the skew quadrupole. The source of the normal quadrupole is located mainly in the FP coupler region while the source of the skew quadrupole is located purely in the HOM coupler region. This is anticipated since the FP coupler has one dimension symmetry, while the HOM coupler has none.

2.6.5 Fields of higher-order modes, m>2

The fields of higher-order modes, m>2, are small. Shown in Fig. 2-12 are the sextupole fields (m=3). These fields are much smaller then the dipole and quadrupole fields. The fields of m=4 or higher are also small. They can be ignored. In the cavity steering studies in the following chapters, we will only keep the terms up to m=2.

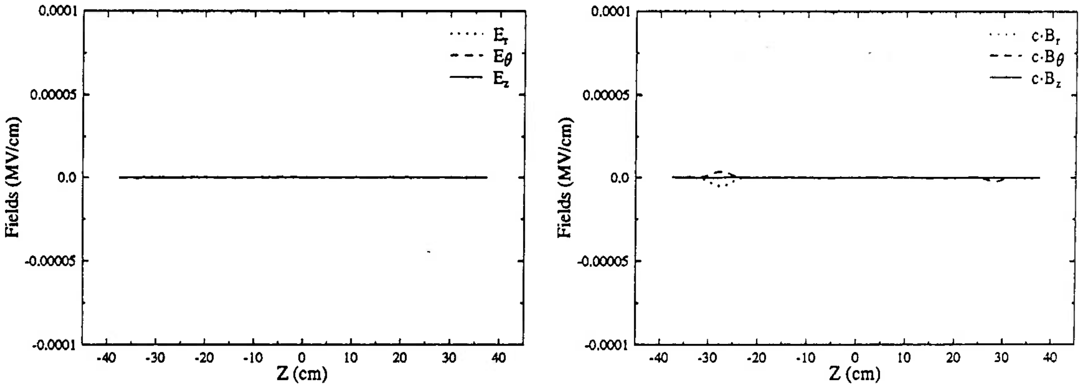

Figure 2-12: Fields of mode m=3.

Chapter 3

The effects of the Multipole Fields on Beam Dynamics

In the previous chapter, we studied the multipole field distributions of standing waves in the cavity. The actual fields vary as $e^{-j\omega t}$. As a charged particle traverses the cavity, its trajectory will be pushed and bent by these fields as result of acceleration and steering. The strength of these effects depends on both the initial RF phase of the fields when the particle enters and the velocity of the particle. If the velocity of the particle v is less than the phase velocity of the RF field, which is the speed of light (c) in our case, there will be a phase slippage while the particle is traversing the cavity. The acceleration will be different due to this slippage, and the phase of maximum acceleration for particles with different energies will be different. The steering will be affected by the slippage the same way. Moreover, the transverse force is the combination of eE_r and evB_θ. For $m = 0$ modes, E_r and cB_θ have the same amplitude throughout the cavity. For $v = c$, the transverse force from the E and the B terms totally cancel. For $v \neq c$, the remnant of the cancellation is finite, and the force is radial and cylindrically symmetric and is sensitive to v. This force produces the so-called azimuthal focusing. For the multipoles (m=1,2), the fields are well localized. The amplitudes of $E_\perp$ and $cB_\perp$ differ by a large amount. There are transverse forces either for $v = c$ or $v \neq c$ and the forces are not as sensitive to the phase slippage and the velocity of the particle as the m=0 mode. In this chapter, we present a quantitative study of the effects of the multipole fields on the beam dynamics.

3.1 Transverse momentum change due to the multipole fields

The transverse force experienced by a particle traversing an RF field is

$$\mathbf{f} = \frac{\mathbf{F}_\perp}{e} = \mathbf{E}_\perp + (\mathbf{v} \times \mathbf{B})_\perp \qquad (3-68)$$

Usually in accelerator beams, $v_\perp << v$ and $v_z \approx v$. For cases where H_z is small, as in the CEBAF cavity for example, Eq. (3-68) reduces to

$$\mathbf{f} = \mathbf{E}_\perp + v\mathbf{z}_0 \times \mathbf{B}_\perp \qquad (3-69)$$

Consider only the part which is related to $e^{j\zeta_n z}$. For TM modes

$$\begin{aligned} \mathbf{E}_\perp &= \frac{j\zeta_n}{k^2 - \zeta_n^2} \nabla_\perp E_z & \text{(3-70)} \\ \mathbf{H}_\perp &= \frac{jk}{Z_0(k^2 - \zeta_n^2)} \mathbf{z}_0 \times \nabla_\perp E_z & \text{(3-71)} \end{aligned}$$

and for TE mode

$$\begin{aligned} \mathbf{H}_\perp &= \frac{j\zeta_n}{k^2 - \zeta_n^2} \nabla_\perp H_z & \text{(3-72)} \\ \mathbf{E}_\perp &= -\frac{jZ_0k}{k^2 - \zeta_n^2} \mathbf{z}_0 \times \nabla_\perp H_z & \text{(3-73)} \end{aligned}$$

We have the transverse force

$$\begin{aligned} \mathbf{f} &= \frac{j\zeta_n}{k^2 - \zeta_n^2} \nabla_\perp E_z + \frac{jk\mu v}{Z_0(k^2 - \zeta_n^2)} \mathbf{z}_0 \times \mathbf{z}_0 \times \nabla_\perp E_z \\ &\quad - \frac{jZ_0k}{k^2 - \zeta_n^2} \mathbf{z}_0 \times \nabla_\perp H_z + \frac{j\zeta_n \mu v}{k^2 - \zeta_n^2} \mathbf{z}_0 \times \nabla_\perp H_z \\ &= \frac{j}{k^2 - \zeta_n^2} \left(\zeta_n - \frac{k\mu v}{Z_0} \right) \nabla_\perp E_z \\ &\quad + \frac{j}{k^2 - \zeta_n^2} \left(\zeta_n \mu v - Z_0 k \right) \mathbf{z}_0 \times \nabla_\perp H_z & \text{(3-74)} \end{aligned}$$

The momentum change for mode m due to this force is

$$\Delta \mathbf{P}_{m\perp} = \frac{1}{v} \sum_n \int dz \mathbf{F} \qquad (3-75)$$

We can evaluate the momentum change by substituting the E_z and H_z given in the previous chapter, Eqs. (2-50, 2-63). For the purpose of a general analysis of the steering effect in this section, we will, instead, use a more general expression of the longitudinal field. We will extend the expansion period to infinity ($L \rightarrow \infty$). The spectrum of ζ_n then becomes continuous (ζ_z). The summation over n is replaced by an integral. The θ dependence of the expansion is unchanged. Considering that the time dependence of the fields is $e^{j\zeta_n - j\omega t}$ and assuming that the energy of the particle is high ($\beta \approx 1$), integrating Eq. (3-75) over t and ζ_z from $-\infty$ to $+\infty$ leads to

$$\Delta \mathbf{P}_{m\perp} = -\frac{je}{\omega} \nabla_{\perp} E_z(r, \theta, m) \qquad (3-76)$$

Only the TM mode contributes to the transverse kick. The general form of E_z for mode m with wave number ζ_z is

$$E_z(r, \theta, z, \zeta_z) = \sum_{m=0}^{\infty} A_m J_m(\eta_r r) \cos(m\theta) e^{j\zeta_z z} + \sum_{m=0}^{\infty} B_m J_m(\eta_r r) \sin(m\theta) e^{j\zeta_z z} \quad (3-77)$$

where $\eta_r^2 + \zeta_z^2 = k^2 = \frac{\omega^2}{c^2}$, $J_m(\eta_r r) = \sum_{\ell=0}^{+\infty} \frac{(-1)^\ell}{\ell!(\ell+m)!} \left(\frac{\eta_r r}{2}\right)^{2\ell+m}$ is the Bessel function. We have

$$\begin{aligned} \Delta \mathbf{P}_{\perp} &= -\frac{je}{\omega} \sum_{\ell=0}^{+\infty} \frac{(-1)^\ell (2\ell+m)}{\ell!(\ell+m)!} \left(\frac{\eta_r}{2}\right)^{2\ell+m} r^{2\ell+m-1} (A_m \cos(m\theta) + B_m \sin(m\theta)) \mathbf{r}_0 \\ &\quad + \frac{je}{\omega} \sum_{\ell=0}^{+\infty} \frac{(-1)^\ell m}{\ell!(\ell+m)!} \left(\frac{\eta_r}{2}\right)^{2\ell+m} r^{2\ell+m-1} (A_m \sin(m\theta) - B_m \cos(m\theta)) \boldsymbol{\theta}_o (3-78) \end{aligned}$$

To first order in r

$$\begin{aligned} \Delta \mathbf{P}_{\perp} &= -\frac{je}{\omega} \left(-\frac{\eta_r^2 A_0}{2} (x\mathbf{x}_0 + y\mathbf{y}_0) + \frac{\eta_r A_1}{2} \mathbf{x}_0 + \frac{\eta_r B_1}{2} \mathbf{y}_0 \right. \\ &\quad \left. + \frac{\eta_r^2 A_2}{4} (x\mathbf{x}_0 - y\mathbf{y}_0) + \frac{\eta_r^2 B_2}{4} (y\mathbf{x}_0 + x\mathbf{y}_0) \right) \qquad (3\text{-}79) \end{aligned}$$

Now it is clear that the $m = 0$ (A_0) term is cylindrically symmetric which causes azimuthal focusing, the $m = 1$ (A_1 and B_1) terms are the dipole moments which result in steering in the x and y planes, and the $m = 2$ (A_2 and B_2) terms are the quadrupole and the skew quadrupole moments which produce both focusing and $x-y$ coupling. The normal quadrupole is related to $\cos(2\theta)$ and the skew quadrupole is related to $\sin(2\theta)$ in the E_z expansion.

Since $\eta_r^2 = k^2 - \zeta_z^2 = -\frac{\omega^2}{v^2\gamma^2}$ goes to zero as γ goes to infinity, from a first glance at Eq. (3-79) one would conclude that the transverse momentum change closely depends on the energy of the particle. This is not the case for high energy particles. In the case of small η_r, $J_m(\eta_r r)$ is proportional to η_r^m. From the multipole studies in the previous chapter, the field has finite value for each of the modes $m = 0, 1, 2$. This suggests that $\eta_r^m A_m$ and $\eta_r^m B_m$ is independent of γ. So the dipole and quadrupole terms in $\Delta \mathbf{P}_\perp$ become finite constants for large γ while the azimuthal focusing varies as $\frac{1}{\gamma^2}$.

The above results were obtained under the assumption that the trajectory of the particle is a straight line, which is equivalent to a thin lens approximation. This is true for the dipole and the quadrupoles terms since the fields of these modes are well localized in the coupler regions. For the $m = 0$ mode, there is a thick lens effect and a more accurate description of the cavity focusing can be obtained by taking into account the variation of the particle trajectory[20, 21]. For TM and $m = 0$ mode, Eqs. (2-57)-(2-61) to first order in r are

$$E_z(r,z,t) = E_z(z)\cos(\omega t + \phi_0) \tag{3-80}$$

$$E_r(r,z,t) = -\frac{r}{2}\frac{dE_z(z)}{dz}\cos(\omega t + \phi_0) \tag{3-81}$$

$$B_\theta(r,z,t) = -\frac{r\omega}{2c^2}E_z(z)\sin(\omega t + \phi_0) \tag{3-82}$$

where the sinusoidal time relation is included and ϕ_0 is the phase offset of the particle relative to the phase of maximum acceleration. All of the fields are in terms of the longitudinal field $E_z(z)$. The radial momentum change due to these fields is

$$\Delta P_r(z) = e\int_{-\infty}^{z}\left(-\frac{r(z)}{2}\frac{dE_z(z)}{dz}\cos(\omega t + \phi_0) + \frac{\omega v_z r(z)}{2c^2}E_z(z)\sin(\omega t + \phi_0)\right)\frac{dz}{v_z} \tag{3-83}$$

Let $G_z(z) = eE_z(z)/mc^2$, and integrate the first term on the right hand side by parts.

We have at position z

$$\begin{aligned}
\gamma(z)\beta_r(z) &= \gamma(-\infty)\beta_r(-\infty) - \frac{r(z)}{2\beta_z(z)}G_z(z)\cos\Big(\omega t(z) + \phi_0\Big) \\
&+ \int_{-\infty}^{z} \frac{r'(z')}{2\beta_z(z')}G_z(z')\cos\Big(\omega t(z') + \phi_0\Big)dz' \\
&- \int_{-\infty}^{z} \frac{r(z')}{2\gamma^3(z')\beta_z^3(z')}G_z^2(z')\cos^2\Big(\omega t(z') + \phi_0\Big)dz' \\
&- \int_{-\infty}^{z} \frac{\omega r(z')}{2c\gamma^2(z')\beta_z^2(z')}G_z(z')\sin\Big(\omega t(z') + \phi_0\Big)dz' \qquad \text{(3-84)}
\end{aligned}$$

Since $r'(z) = \frac{\gamma(z)\beta_r(z)}{\gamma(z)\beta_z(z)}$, at high energies, we have

$$r(z) = r(a) + \frac{\beta_r(-\infty)}{\beta_z(-\infty)}(z-a) - \int_a^z \frac{r(z')}{2\gamma(z')\beta_z^2(z')}G_z(z')\cos\Big(\omega t(z') + \phi_0\Big)dz' \qquad (3-85)$$

where $G_z(z) = 0$ for $z \leq a$ is assumed. Substituting $r(z)$ into Eq. (3-84), to the second order of γ we have for the final momentum of the particle after traversing the cavity

$$\begin{aligned}
\gamma(\infty)\beta_r(\infty) &= \gamma(-\infty)\beta_r(-\infty)\left(1 + \frac{I_{01}}{\gamma} + \frac{I_{02} - I_{03}}{\gamma^2}\right) \\
&\quad -r(a)\left(\frac{I_{11}}{\gamma} + \frac{I_{12} - I_{13} + I_{14}}{\gamma^2}\right) \qquad \text{(3-86)}
\end{aligned}$$

where

$$\begin{aligned}
I_{01} &= \frac{1}{2}\int_{-\infty}^{\infty} G_z(z')\cos\Big(\omega t(z') + \phi_0\Big)dz' \\
I_{02} &= \frac{1}{4}\int_{-\infty}^{\infty}\left(G_z(z')\cos\Big(\omega t(z') + \phi_0\Big)\int_{-\infty}^{z'} G_z(z'')\cos\Big(\omega t(z'') + \phi_0\Big)dz''\right)dz' \\
I_{03} &= \frac{1}{4}\int_{-\infty}^{\infty}(z'-a)G_z^2(z')\cos^2\Big(\omega t(z') + \phi_0\Big)dz' \\
I_{11} &= \frac{1}{4}\int_{-\infty}^{\infty} G_z^2(z')\cos^2\Big(\omega t(z') + \phi_0\Big)dz' \\
I_{12} &= \frac{1}{8}\int_{-\infty}^{\infty}\left(G_z(z')\cos\Big(\omega t(z') + \phi_0\Big)\int_{-\infty}^{z'} G_z^2(z'')\cos^2\Big(\omega t(z'') + \phi_0\Big)dz''\right)dz' \\
I_{13} &= \frac{1}{8}\int_{-\infty}^{\infty}\left(G_z^2(z')\cos^2\Big(\omega t(z') + \phi_0\Big)\int_{-\infty}^{z'} G_z(z'')\cos\Big(\omega t(z'') + \phi_0\Big)dz''\right)dz' \\
I_{14} &= \frac{\omega}{2c}\int_{-\infty}^{\infty} G_z(z')\sin\Big(\omega t(z') + \phi_0\Big)dz'
\end{aligned}$$

Terms I_{01}, I_{02} and I_{03} are the higher-order terms of the adiabatic damping. Terms I_{11}, I_{12}, I_{13} and I_{14} are related to the azimuthal focusing. For high energy particles, the dominate term for the azimuthal focusing is I_{11}. It is positive for all phase offsets. Thus the field is focusing for all phases, and the focusing is proportional to $\frac{1}{\gamma}$. Rewrite I_{11} in the following form

$$\frac{1}{4}\left(\cos(2\phi_0)\int_{-\infty}^{+\infty} E_z^2(z)\cos^2(\omega z/c)dz + \sin^2(\phi_0)\int_{-\infty}^{+\infty} E_z^2(z)dz\right), \qquad (3-87)$$

which shows that the amplitude of the focusing is modulated by the phase offset (ϕ_0) with a double frequency. If the energy is low, the second order terms becomes important. Those terms are not always positive, and defocusing may exist for some RF phases.

3.2 Particle tracking

Numerical integrations were performed to study the beam dynamics in the superconducting cavities. To evaluate the RF fields in the cavity for the particle tracking, the original MAFIA output can be used to calculate the 3-D fields by means of interpolation. Alternatively, the Fourier expansions developed in chapter 2 can be used. Since the 3-D interpolation involves fewer mathematical manipulations than the Fourier expansions, execution will be faster for the first choice.

In the modeling, only the fields close to the axis are included to save computer memory. The mesh in this region is uniform in both the x and y planes. The mesh size is 4 mm. The fields of the mesh points with indices -5 to 4 in the x and the y directions and 1 to 197 in the z direction are included. This mesh covers a physical region of -2.0 to 1.6 cm in the x and y axes and -37.5 to 37.5 in the z axis. Since the fields are not all defined on the mesh points (Fig. 3-13), the actual region covered by the modeling in the x and the y direction is -1.6 to 1.6 cm.

3.2.1 Subroutine for evaluating the fields

Subroutine CAVFLD is written for the field evaluations. It contains five $10 \times 10 \times 197$ arrays to store the five 3-D field components, namely E_x, E_y, E_z, B_x and B_y, of the

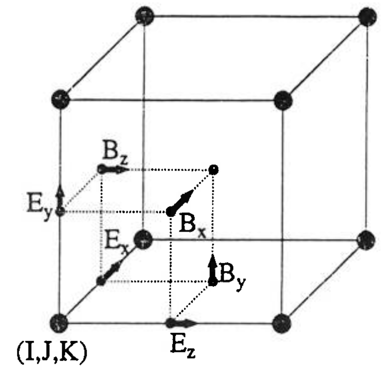

Figure 3-13: The fields defined at mesh point (I,J,K).

MAFIA output. B_z is small. The transverse velocity $v_\perp$ is small, and $v_\perp \times B_z$ is negligible.

The IMSL subroutine Q3DVL is used for the 3-D interpolations. The interpolation function used in Q3DVL is a 3-D quadratic function, and a $3 \times 3 \times 3$ grid lattice is used for the interpolation.

There more than 300 identical cavities in the CEBAF accelerator. These cavities have different orientations in terms of the direction and the location of their FP power couplers. Two parameters, the polarity and the position of the FP coupler, are defined in the code to specify the orientations of the cavities. The polarity of a cavity is defined as positive "+" if direction of the FP coupler is oriented such that the power is fed into the cavity from the positive x direction and it is "-" if the power is fed in from the negative x direction. The position of the FP coupler is called downstream if the FP coupler is at the downstream end of the cavity and it is called upstream if the FP coupler is at the upstream end of the cavity. The MAFIA modeling is for the cavity with positive polarity and downstream FP coupler. The fields of other cavities can be obtained in terms of coordinate transforms.

In a cavity-pair, the first cavity has a downstream FP coupler and the second cavity has a upstream coupler (the FP couplers are in the middle of the two cavities). The two cavities have the same polarities. The cavity-pair has a rotational symmetry about the x axis (180^0).

A cryomodule contains four cavity-pairs. The first and the fourth cavity-pairs have the same polarities (negative) and the two cavity-pairs in the middle have positive polarities. The cavity-pairs with different polarities have rotational symmetry about the z axis (180^0).

The fields transform as vectors under rotations. In the code, the field point (x, y, z) in the lab coordinate is transformed into the local coordinate system used in MAFIA. The fields are calculated in the MAFIA coordinate and then are transformed back to the lab system for particle tracking simulations.

3.2.2 Codes for beam dynamics

Two codes are used to study the beam dynamics in the cavity. CAVFOURIER is written for studying the effects of a single cavity. It performs Fourier transforms to decompose the transverse momentum change into multipoles. PARMELA is modified to include the CEBAF cavity subroutines. It is used to study the effects of multi-cavities in a beam line. CBFCAV3DIMP is the beam dynamics routine for both CAVFOURIER and PARMELA. It numerically integrates the Lorentz force

$$\mathbf{F} = e\left(\mathbf{E}(x,y,z)\sin(\omega t(z)+\phi_0) + \mathbf{v}\times\mathbf{B}(x,y,z)\cos(\omega t(z)+\phi_0)\right) \qquad (3-88)$$

$$\Delta\mathbf{P} = \int_{z=37.5}^{z=37.5} \mathbf{F}\frac{dz}{v_z} \qquad (3-89)$$

where ϕ_0 is the initial phase of the RF field and $t(z) = \int_{-37.5}^{z} \frac{z'}{v(z')} dz'$ is the time elapsed in the cavity. The momentum of the particle is accumulated. At the end of the cavity, the longitudinal momentum change determines the acceleration of the cavity and the transverse momentum change determines the steering.

CAVFOURIER

The purpose of this code is to get the coeficients of Eq. (3-79). From these coefficients, the dipole strength and the focal length of the azimuthal focusing and the quadrupoles can be obtained. Rewrite Eq. (3-79) in the component form

$$\Delta P_x = a_x + b_x x + c_x y \tag{3-90}$$

$$\Delta P_y = a_y + b_y y + c_y x \tag{3-91}$$

In this expression, the focusing coefficient is $\frac{1}{2}(b_x + b_y)$ and the quadrupole coefficient is $\frac{1}{2}(b_x - b_y)$. The skew quadrupole coefficients are c_x and c_y and they must be equal. The x and y in Eqs. (3-90,3-91) are defined as the coordinate at the entrance of the cavity.

A number of particles are initiated uniformly on a circle of radius a at $z = -37.5$. The initial transverse momenta of the particles are zero. The momenta changes calculated at the end of the cavity ΔP_x and ΔP_y are only functions of the azimuthal angle θ. The coefficients are obtained by the following integrals

$$a_x = \frac{1}{2a\pi}\int_0^{2\pi} \Delta P_x d\theta \qquad a_y = \frac{1}{2a\pi}\int_0^{2\pi} \Delta P_y d\theta$$

$$b_x = \frac{1}{a\pi}\int_0^{2\pi} \Delta P_x \cos(\theta) d\theta \qquad b_y = \frac{1}{a\pi}\int_0^{2\pi} \Delta P_y \sin(\theta) d\theta$$

$$c_x = \frac{1}{a\pi}\int_0^{2\pi} \Delta P_x \sin(\theta) d\theta \qquad c_y = \frac{1}{a\pi}\int_0^{2\pi} \Delta P_y \cos(\theta) d\theta$$

Modified PARMELA

PARMELA[18] is a versatile multi-particle code in which a beam, represented by a collection of particles, may be transformed through a linac and/or transport system specified by the user. It was originally developed by Don Swenson[19] at MURA in 1963. It has been modified by various users to deal with their special elements. PARMELA was modified to include subroutines dealing with special CEBAF elements such as CEBAF capture section and CEBAF buncher. Later on, 3-D CEBAF cavity subroutines CBFCAV3DIMP and CAVFLD were added to the CEBAF version PARMELA by the author. The new version PARMELA is capable of simulating the entire CEBAF beam line. PARMELA works as a ray-tracing program. For simpler elements, it uses the transport matrix to map the coordinates of the particles. For complicated elements like CEBAF cavities, numerical integration is used. PARMELA can perform space charge simulations, emittance and betatron function calculations, etc.

3.3 Beam dynamics in the CEBAF cavity

Before investigating the beam dynamics in the cavity, we need to address one problem that was left unanswered in chapter 2. In section 2.6 we mentioned that there are mutual contaminations among the adjacent modes. If there is no contamination, the eigenvalue (or the frequency) and the eigenvectors (or the fields) satisfy the Maxwell's equations with optimally small deviation. The contamination among the modes induces inconsistency among the fields and the frequency. The frequency and the fields will no longer match well to Maxwell's equations. Even though the error caused by the contamination is expected to be small since the contamination index (2×10^{-3}) is small, the effect of the inconsistency may cause some problems in beam dynamics simulations. Since the fields are contaminated, in principle, one can correct the fields to minimize the error induced to the Maxwell's equations, but it is impractical. On the other hand, one can also modify the frequency to match the fields so that the Maxwell's equations can be satisfied with minimum error.

A good place to look at this effect of the mismatched frequency is the azimuthal focusing. At high energies, the azimuthal focusing goes to zero. To first order of r, the B field is proportional to the E field and the frequency. If the frequency is inconsistent with the fields, the balance between the forces from the E and the B fields will be destroyed. The azimuthal focusing for very high energy particles will have finite strength instead of zero as predicted from the analytical analysis. The results of the azimuthal focusing with the contaminated fields and frequency is shown in Fig. 3-14, the solid line is for

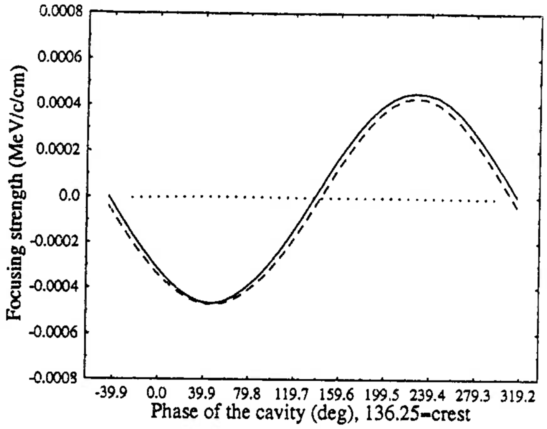

Figure 3-14: Azimuthal focusing for E=1 and 10 GeV with original frequency and fields from MAFIA.

energy 10 GeV and the dashed line is for 1 GeV. There is no $\frac{1}{\gamma}$ relation between this two curves. However, the small difference between the curves suggests that the azimuthal focusing at these energies is small. Thus the finite focusing for 10 GeV is mainly due to the frequency error.

To first order of r, the fields that satisfy the Maxwell's equations have the form of Eqs. (3-80)-(3-82). We have at high energies

$$\begin{aligned}\Delta P_r \cdot c &= \int_{-\infty}^{\infty}\left(-\frac{r}{2}\frac{dE_z(z,\omega_1)}{dz}\cos(\omega_1 t+\delta)+\frac{r\omega_1\beta}{2c}E_z(z,\omega_1)\sin(\omega_1 t+\delta)\right)\frac{dz}{\beta}\\ &= \frac{A}{\gamma} \end{aligned} \tag{3-92}$$

If a different frequency ω is used and the amplitudes of the fields are kept the same, we have

$$\begin{aligned}\Delta P_r \cdot c &= \int_{-\infty}^{\infty}\left(-\frac{r}{2}\frac{dE_z(z,\omega_1)}{dz}\cos(\omega t+\delta)+\frac{r\omega_1\beta}{2c}E_z(z,\omega_1)\sin(\omega t+\delta)\right)\frac{dz}{\beta}\\ &= \int_{-\infty}^{\infty}\left(-\frac{r}{2}\frac{dE_z(z,\omega_1)}{dz}\cos(\omega t+\delta)+\frac{r\omega\beta}{2c}E_z(z,\omega_1)\sin(\omega t+\delta)\right)\frac{dz}{\beta}\\ &\quad+\int_{-\infty}^{\infty}\frac{(\omega_1-\omega)r}{2c}E_z(z,\omega_1)\sin(\omega t+\delta)dz\\ &= \frac{A}{\gamma}+\frac{(\omega_1-\omega)r}{2c}E_g\sin(\delta) \end{aligned} \tag{3-93}$$

where E_g is the maximum energy gain in one cavity. It is shown that the error induced in the momentum linearly depends on the difference of the frequency. The sine dependence on the RF phase offset is also shown.

The maximum energy gain in Fig. 3-14 is 2.5 MeV. The amplitude of the ΔP deviation is 0.46×10^{-3} MeV/c/cm.

$$\Delta F = \frac{c\Delta P}{\pi E_g} = 1.756 \text{ MHz} \qquad (3-94)$$

The optimal frequency for the CEBAF cavity is, 1495.38+1.756, 1497.1 MHz. With application of this frequency to code CAVFOURIER, the result for the azimuthal focusing for 10 GeV is shown by the dotted line in Fig. 3-14. The focusing strength is zero through out 360^0 of RF phase.

3.3.1 The effects of the cylindrical symmetric fields (m=0)

Acceleration

The m=0 mode is the acceleration mode. The energy change of the particle for a given momentum change ΔP is

$$\Delta E = \gamma m_0 c^2 (\sqrt{1 + \frac{2P_0\Delta P + \Delta P^2}{(\gamma m_0 c)^2}} - 1) \qquad (3-95)$$

where P_0 is the initial momentum. The energy gain of the low energy particle depends on its initial energy, and relativity is certainly a factor. Another factor is due to the velocity of the particle being slower then the phase velocity of the RF wave, which is the speed of light. The particle is not accelerated at a fixed RF phase. For example, a particle initially accelerated on crest will be shifted off crest while going through the cavity and be less accelerated. For high energy particles, the energy gain $\Delta E = \Delta Pc$ is independent of initial energy. Fig. 3-15 shows the energy gain of the particles with different initial energies as functions of the initial phase of the cavity. The gradient of the cavity is 5 MV/m. The effective length of the cavity is 0.5 m. The maximum acceleration for a high energy particle is 2.5 MeV. The maximum acceleration for low

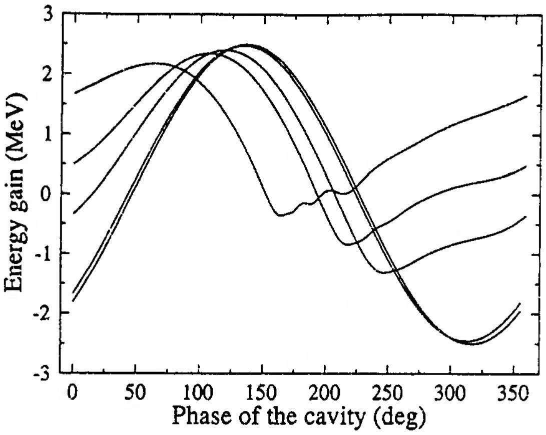

Figure 3-15: Energy gain *vs.* initial RF phase for different initial energies. Gradient=5 MV/m. From the left to the right: E_0 =0.5, 1.0, 1.5, 5.0 and 10^3 MeV.

energy particles is smaller due to the phase slippage. For initial energy of 0.5 MeV, the energy gain is 2.17 MeV. The maximum acceleration RF phase, crest phase, is different for different initial energies. For example, the crest phase for 100 MeV is 136.3^0, 10 MeV is 135.6^0, 5 MeV is 133.8^0 and 0.5 MeV is 64.5^0. The acceleration curve is symmetric if the initial energy is high and asymmetric if the initial energy is low. A 5 MeV electron is already quite relativistic, and the acceleration curve is almost the same as that of the 10^3 MeV electrons.

Azimuthal focusing

The strength of the azimuthal focusing in terms of the transverse momentum change for initial energies of 1000, 100, 40, 20, 10 MeV are shown in Fig. 3-16*a* and those for
3 Mev ✓
5 MeV 2.5 MeV and 0.5 MeV are shown in Fig. 3-16*b*. Positive strength corresponds to defocusing and negative strength corresponds to focusing. The diamond markers indicate the phases of the maximum acceleration. The gradient of the cavity for these simulations is 5.0 MV/m. At high energies, 100, 40, 20 MeV, the curves clearly show the $\frac{1}{\gamma}$ dependence and the double frequency modulation. At 10 MeV and 5 MeV, the curves begin to show asymmetric focusing about the crest phase. Higher-order terms of Eq. (3-86) become important at low energies. At energies higher than 5 MeV, it is

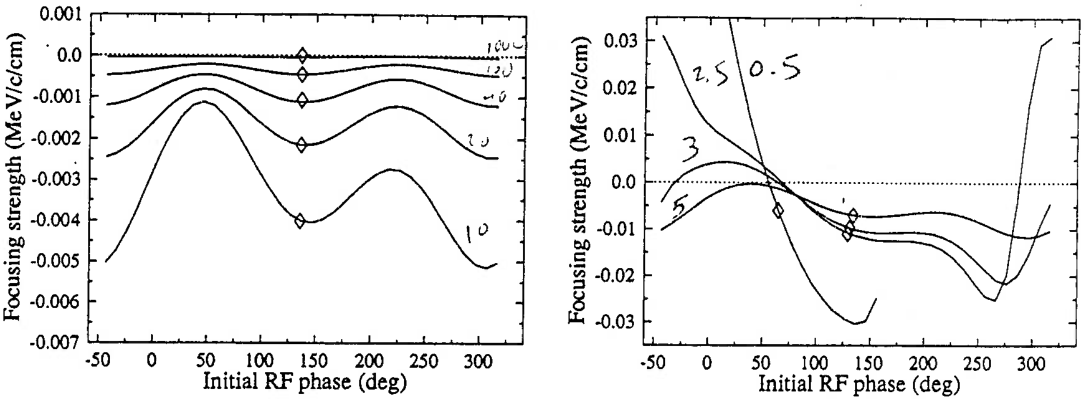

Figure 3-16: The strength of azimuthal focusing *vs.* the initial RF phase for different initial energies. Gradient=5 MV/m.

Table 3-1: The focal length of azimuthal focusing.

Initial energy (MeV)	f (m)
0.5	-4.46
2.5	-4.50
5	-10.71
10	-31.17
100	-2213.82

focusing at all phases. At low energies, 3 MeV, 2.5 MeV and 0.5 MeV, there are phases that have defocusing forces. Knowing the output energy of the particle E_{out} in MeV, one can get the focal length

$$f(\text{cm}) = \frac{E_{out}}{\text{Focusing strength}} \qquad (3-96)$$

Table 3-1 shows the focal lengths on the crest phase for electrons with different initial energies. The azimuthal focusing is independent of the polarity ($\pm x$) and the position (upstream FPC or downstream FPC) of the couplers.

3.3.2 Cavity steering, the effects of the m=1 fields

The m=1 mode is the mode of cavity steering. The effect of this mode is to steer the beam off the designed beam centroid. The CAVFOURIER results of the x component of the steering for energies of 1 GeV, 100 MeV, 40 MeV, 20 MeV and 10 MeV are shown in Fig. 3-17*a* and for energies of 5 MeV, 3 MeV, 2.5 MeV and 0.5 MeV are shown in Fig. 3-17*b*. The results for the y component are shown in Figs. 3-18(a, b). In these simulations, the FP coupler is downstream, the power is fed in from the negative x direction, and the gradient is 5.0 MV/m. The phase relation of the dipole strength depends on the polarity and the position of the FP coupler. If the polarity of a cavity is changed from negative to positive, the corresponding curve of the dipole strength can be obtained by multiplying "-1" to the curve. If the position of the FP coupler is changed from downstream to upstream, the dipole curve can be obtained by reflecting the curve about the crest phase and multiplying the curve by "-1" (since there is 180^0 phase difference in the fields).

As shown in Figs. 3-17*a* and 3-18*a*, at high energies, the dipole strength is independent of energy. At low energies (Figs. 3-17*b* and 3-18*b*), the dipole strengths become energy dependent. The amplitude of the dipole steering in the x plane is about five times larger than in the y plane. The phase relation of the dipoles are determined by the RF phases of the couplers. The maximum x steering is about 60^0 ahead of crest phase and the maximum y steering is about 130^0 ahead of the crest.

We can make an equivalence between the strength of cavity steering with the strength of a dipole magnet. For a given momentum change ΔP, the equivalent dipole strength of the cavity steering is calculated as

$$\int B d\ell (\mathrm{Tesla \cdot m}) = \frac{\Delta P(\mathrm{GeV/c})}{0.2998} \qquad (3-97)$$

Table 3-2 lists the strengths of the dipole steering in term of the equivalent strength of dipole magnets at some selected energies.

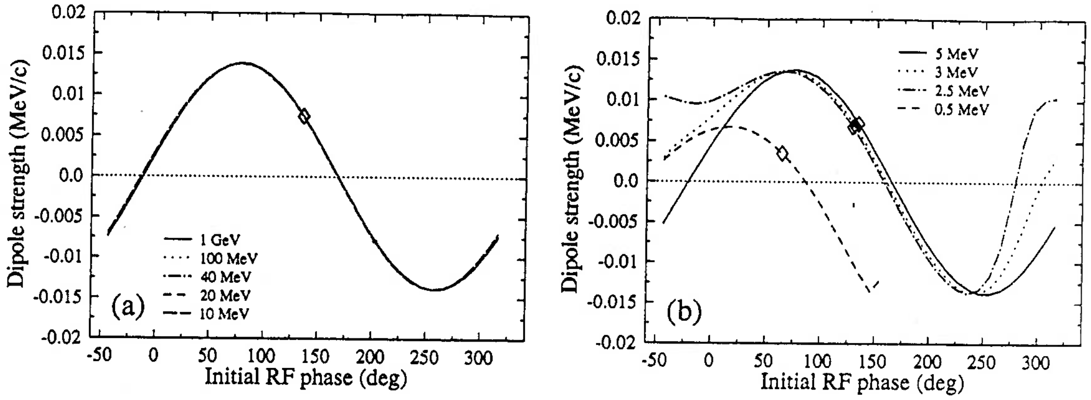

Figure 3-17: The strength of cavity steering in the x plane *vs.* the initial RF phase for different initial energies. Gradient=5 MV/m.

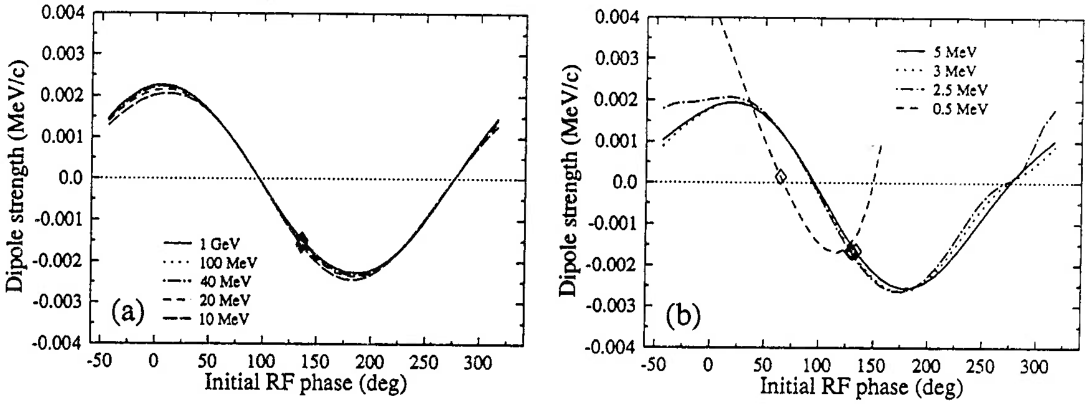

Figure 3-18: The strength of cavity steering in the y plane *vs.* the initial RF phase for different initial energies. Gradient=5 MV/m.

3.3.3 Quadrupoles, the effects of the m=2 fields

The m=2 mode has normal and skew quadrupole components. The effect of the normal quadrupole is to focus. The effect of the skew quadrupole is to rotate the beam, which causes $x-y$ coupling. The CAVFOURIER results for the strengths of the normal and the skew quadrupoles are shown in Figs. 3-19 and 3-20 respectively. The maximum strength of the normal quadrupole is about five times smaller then the maximum strength of the dipole. The strength of the skew is about half of the strength of the normal quadrupole. For the normal quadrupole, a positive strength means defocusing in the x plane. The phase dependence of the skew quadrupole is the same as

Table 3-2: Equivalent strength of dipole magnet.

Initial energy (MeV)	x plane, $\int Bd\ell$ (Tesla·m)	y plane, $\int Bd\ell$ (Tesla·m)
0.5	1.17×10^{-5}	4.67×10^{-7}
2.5	2.27×10^{-5}	-5.50×10^{-6}
5	2.40×10^{-5}	-5.50×10^{-6}
10	2.46×10^{-5}	-5.34×10^{-6}
1000	2.46×10^{-5}	-4.90×10^{-6}

Table 3-3: Equivalent strength of quadrupole magnet.

Initial energy (MeV)	normal quad, $d(\int Bd\ell)/dr$ (Tesla·m)/cm	skew quad, $d(\int Bd\ell)/dr$ (Tesla·m)/cm
0.5	1.17×10^{-6}	-1.00×10^{-7}
2.5	3.00×10^{-6}	-4.27×10^{-6}
5	3.57×10^{-6}	-4.24×10^{-6}
10	3.94×10^{-6}	-4.04×10^{-6}
1000	4.17×10^{-6}	-3.67×10^{-6}

that of the y dipole. They both are solely due to the fields of the HOM coupler. The phase dependence of the normal quadrupole is close to that of the x dipole, but the whole curve is shifted to the left by about 10^0. The normal quadrupole is affected by both HOM and FP couplers, and the contribution from the FP coupler is dominant.

Similarly, we can make an equivalence between the strength of the quadrupole moment to the gradient of a quadrupole magnet. For a given momentum change ΔP, the equivalent quadrupole gradient is

$$\frac{d(\int Bd\ell)}{dr}(\mathrm{Tesla\cdot m/cm}) = \frac{\Delta P(\mathrm{GeV/c/cm})}{0.2998} \qquad (3-98)$$

We show in Table 3-3 the strengths of the quadrupole fields in terms of the equivalent strengths of quadrupole magnets at different energies

The phase relation of the quadrupole strength depends only on the position of the FP coupler. The curves shown in Figs. 3-19 and 3-20 are for the case with a downstream

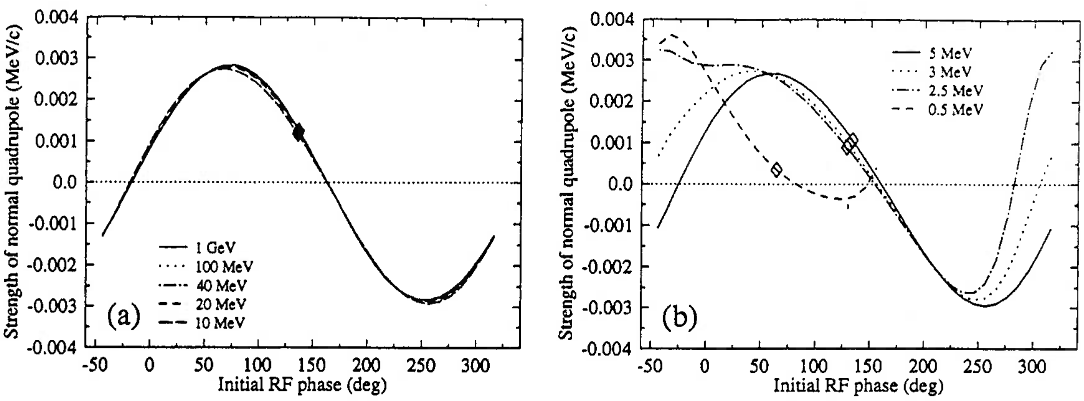

Figure 3-19: The strength of normal quadrupole *vs.* the initial RF phase for different initial energies. Gradient=5 MV/m.

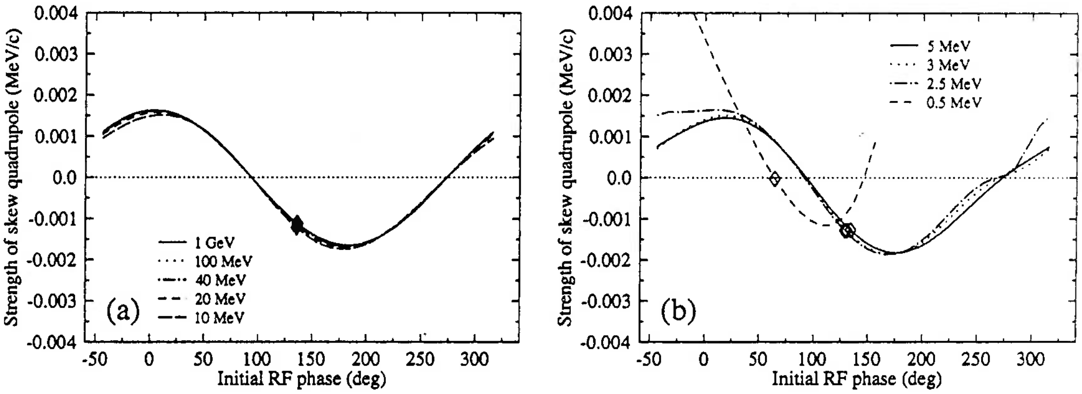

Figure 3-20: The strength of skew quadrupole *vs.* the initial RF phase for different initial energies. Gradient=5 MV/m.

FP coupler. If the FP coupler is at the upstream of the cavity, the curve for the normal quadrupole can be obtained by reflecting the curve in Fig. 3-19 about the crest phase and multiplying the curve by "-1", while the curve for the skew quadrupole can be obtained by simply reflecting the curve in Fig. 3-20 about the crest phase.

Chapter 4

Experimental Measurement of the Cavity Steering Effects

The multipole fields of a cavity act on the beam in different ways. The dipole field gives the beam, as a whole, a transverse momentum offset. As the beam propagates down the beam line, it will drift off the reference orbit. The magnitude of the steering is a function of the RF phase. It can be measured by measuring the change of the beam position at some distance down stream from the cavity as the RF phase of the cavity is changed. The focusing fields of the cavity change the betatron functions of the beam line and cause x-y coupling. They do not steer the beam as long as the beam is on axis. If the beam has an offset from the cavity axis, the focusing force will bend the beam toward or away from the axis depending on whether the force is focusing or defocusing. The strength of the focusing can be determined by measuring the change of the relative position of two initially parallel beams as the cavity is turned on and off. Experiments were performed on the CEBAF accelerator to measure the multipole effects of the cavities. Comparison between numerical simulation and the experimental results are presented. Misalignments of cavities are also a source of cavity steering. This steering has different phase relation than the multipoles. It can be extracted from the experimental data by use of the phase relations. Thus, cavity misalignment can also be studied by measuring cavity steering. The evaluation of misalignments is presented in the later part of this chapter.

4.1 Experimental measurement of dipole steering

Cavity steering was measured on the CEBAF 45 MeV injector. A sketch of the injector is shown in Fig. 4-21. The injector starts with a 100 keV gun, followed by chopper and buncher sections. The beam is accelerated up to 0.5 MeV by a capture section. A 1/4-cryomodule, which contains two superconducting cavities, accelerates the beam to 5 MeV. The beam is transported to two cryomodules through a beam line consisting of several quadrupoles. Each of the cryomodules comprises eight superconducting cavities, or four identical cavity pairs with different fundamental power coupler orientations. The nominal gradient of all cavities is 5 MV/m; the total energy of a particle coming out of the second cryomodule is 45 MeV. There are quadrupoles at the entrance and the exit of each cryomodules; the beam proceeds downstream to the north linac through a quadrupole telescope and an injection chicane. At the location of each quad, there are a pair of small dipoles, called correctors, which are oriented in the x and in the y directions respectively, a viewscreen and/or a BPM. The correctors are used to steer the orbit of the beam centroid. The viewscreens and/or BPMs are used to monitor the beam. The quadrupoles in the injector section (below 45 MeV) of the accelerator were not used since the cavity focusing is strong enough to control beam size. They are generally used for beam centering only. The center of the quadrupoles define the center of the beam line. One set of upstream correctors is used for beam centering; if the beam is in the center of the quadrupole, changing the quadrupole excitation does not change the beam position downstream. If the beam is not centered, the upstream correctors must be adjusted until the beam is centered. There are three kinds of beam monitors that can be used to measure the beam position: viewscreens, harps and electronic Beam Position Monitors (BPM). The "Instamatic" program uses viewscreens to measure beam position. This software uses a video camera to take a picture of the beam spot on the screen. Digitized data are analyzed and the beam position is found. The accuracy of Instamatic is about a half millimeter [23]. The harp is a device made up of two or three thin wires. The profile of the beam is measured by pulling the harp traversing the beam. The signal is fitted by a gaussian curve, and the beam position is then obtained. The diameter of the wires is about 50 μ, and the accuracy of the harp is about the diameter of the wires. The harp is good to measure relative positions, but it was not calibrated for absolute position measurement at the time of these experiments were carried out. The BPMs were not functional at the time these experiments were performed. Instamatic and harps were therefore used. The energy of the beam and the gradient of the cavity were measured by use of a 45 MeV spectrometer.

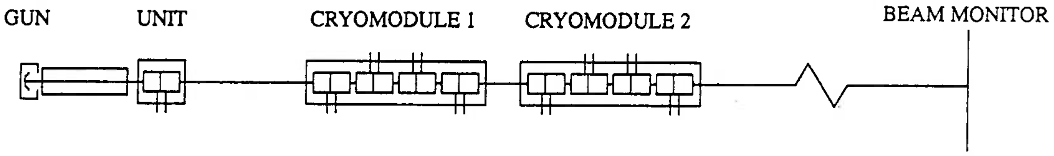

Figure 4-21: The CEBAF 45 MeV injector.

Cavity steering kicks the beam off the reference orbit; the strength of the kick is a function of the RF phase. The beam positions downstream from the cavity are measured in these experiments. Given the distance between the kicker and the beam position monitor, the position deviations can be converted to the steering angles. Comparisons then can be made with numerical calculations.

4.1.1 System setup

The seventh cavity in the second cryomodule was used for the cavity steering study. The beam used in the experiment was pulsed and low current. The beam size was required to be small, and any 60 Hz noise should be suppressed. To measure dipole steering, it is important to place the beam on the beam axis. Otherwise the effects of higher-order multipoles will come in. To minimize the noise generated prior to the cavity being measured, a moderate energy is preferred. The cavities in the two cryomodules run at low gradient of about 1.5 MV/m except for steering cavity, which runs at a maximum gradient of about 5 MV/m. The initial energy of the beam at the entrance of the steering cavity is about 20 MeV.

The energy of the beam is measured by the 45 MeV spectrometer. The crest phase of the cavities are found by finding the maximum energy of the beam while adjusting the RF phase. The gradient of the steering cavity is measured by measuring the energy difference between the energies with the cavity on crest and 180^0 off crest. The effective length of the cavity is 0.5 m, and thus the gradient equals to the energy difference. Since the cavity steering varies with the RF phase, in order to have an accurate energy measurement, the beam should be centered at all times at the exit of the second cryomodule by use of the upstream correctors while the phase of the cavity is changed. The spectrometer is turned off after the energy and gradient measurements. Cavities are phased on crest. Beam is steered straight to the center of the beam monitor, which is about 17 m downstream from the cavity, where the beam position is measured. The RF phase of the steering cavity is then changed and the beam position is measured using the beam monitors. During these measurements, all of the parameters on the beam line except the RF phase of the steering cavity are kept fixed.

4.1.2 Experimental results on cavity steering

Two sets of data were taken. The RF phase δ of the steering cavity was scanned from -90^0 to 90^0 relative to the crest phase with a step size of 10^0. The first set of data was measured by Instamatic. Fig. 4-22a shows the beam position as a function of the RF phase. The initial beam energy for this measurement is 18.42 MeV. The gradient of the steering cavity is 5.26 MV/m. Each data point was measured three times. The deviation between these measurements is about ±0.2 mm. Shown in the figures are the averaged displacement relative to the beam position of the crest phase. The uncertainty of the position measurement is about 0.5 mm. The uncertainty of RF phase is about

2^0, which, in terms of position uncertainty, is 0.36 mm in the x plane and 0.05 mm in the y plane. The total uncertainty on the position measurement is 0.6 mm and 0.5 mm in the x and y planes respectively.

The second set of data was measured by harp, which is shown in Fig. 4-22*b*. The initial energy for this measurement is 17.28 MeV. The gradient is 5.26 MV/m. The harp has a accuracy of about 42 μ in position measurement for a point-like beam. If the beam is finite and the distribution is not a standard gaussian distribution, the mean center of the beam found by the gaussian fitting may deviate from the weighted center of the beam (the beam centroid in our definition). This deviation depends on the distribution of the particles and is in this case smaller than 0.5 mm since the beam is close to a gaussian distribution. The RF phase deviation is the same as in the previous experiment. The uncertainty in position measurement is comparable to that using Instamatic.

It is worth pointing out that the phase offset convention on the CEBAF accelerator is different from the numerical simulation. On the machine, the phase relation is $\cos(\phi - \phi_0)$; it is $\cos(\phi + \phi_0)$ in the numerical code.

The measurement error estimated above does not include the error due to the instability of the machine. We have observed, during the experiment, the instability of the beam, which can be seen in Fig. 4-22*b*. This error could not be quantified. These experiments were carried out on the old injector, and the new injector is expected to have better performance.

4.1.3 Error corrections

There are errors caused by the cavity misalignment, the correctors, and the earth's magnetic field. The earth's field can be compensated by the corrector fields. The remnant fields of the correctors steer the beam with strength which is inversely proportional to the momentum of the particle. As the phase of the cavity is changed, the momentum of the particle is also changed. The steering of the residual field is symmetric about the crest phase. There are two types of cavity misalignments that contribute to cavity steering, with different phase dependences. The tilt misalignment of the cavity projects a fraction of the axial E_z component of the cavity to the transverse plane. The steering from this transverse field has the same RF phase dependence as the acceleration, which is symmetric about the crest phase. The axial-offset misalignment causes the beam to be steered by forces of the azimuthal focusing and quadrupole fields. The azimuthal focusing is approximately symmetric about the crest phase at energies around 20 MeV. The phase dependence of the quadrupole steering is close to the dipole steering.

The symmetric parts of the error can be eliminated by symmetrizing the measured data about the crest phase. Notice that the maximum coupler kicks are about 58^0 off the crest in the x plane and 48^0 in the y plane. The coupler steering has the form of approximately $\cos(\delta + \phi_0)$, where ϕ_0 is the phase offset. Symmetrizing cancels the symmetric part and leaves the net contribution from the couplers.

The asymmetric errors due to axial-offsets in the cavity misalignment can not be eliminated by doing the symmetrizing. We can, however, estimate their magnitudes. The maximum misalignment of the cavity is of the order of 1 mm. According to Figs. 3-17, 3-18, 3-19 and 3-20, the maximum error induced by the 1 mm misalignment is about 4×10^{-4} MeV/c. This error induces relative errors to the dipole steering measurement in the x and the y planes of about ±2% and ±10% respectively.

The symmetrized results of Fig. 4-22 are converted into transverse momentum by the following formula

$$\Delta P(\delta) = (E_0 + 0.5 G_0 \cos(\delta)) \frac{D}{L} \qquad (4-99)$$

where D is the x or y displacement and L is the distance from the cavity to the beam-position detector. L=18.42 for Fig. 4-22*a* (viewscreen) and L=17.28 for Fig. 4-22*b* (harp). The results after the error correction are shown in Fig. 4-23. The uncertainty in momentum in these figures is 0.7×10^{-3} MeV. Also shown for comparison in the figures are the PARMELA results. The experimental results agree with the numerical modelling.

4.2 Experimental measurement of focusing effects

4.2.1 System setup

The focusing effects, which include the azimuthal focusing, normal quad, and the skew quad, were measured on the north linac of the CEBAF accelerator [25]. Two cavities were used in this experiment. With all of the cavities off in the linac, a 42 MeV beam was centered along the beam line. Two beam orbit correctors upstream of the linac were used to create a pair of parallel orbits separated by 10 mm in the x plane. The cavities were turned on with different RF phase settings and the beam spots measured at the beam monitor 34 meters downstream. The beam position was measured by a Beam Position Monitor. Since the dipole steering is insensitive to the beam position, the relative changes of these beams at the beam monitor exhibit the effects of the cavity focusing. A schematic drawing of the system is shown in Fig. 4-24.

As the cavities are connected head-to-head in a cavity pair, the focusing effects add or cancel depending on the phase relation of the cavities. At an energy of about 40 MeV, the azimuthal force is focusing at all phases. The normal quadrupoles cancel if the cavities are both in maximum acceleration or deceleration mode, and they add if the two have opposite phases (maximum acceleration and deceleration). The total normal quad is positive for the second case if the first cavity is accelerating and is negative if the first cavity is decelerating (a positive normal quad defocuses in the x plane). The skew quadrupoles add if the cavities are both in maximum acceleration or deceleration mode, and cancel if the cavities have opposite phases. By measuring the cavity focusing at different cavity settings, the individual component can be singled out by use of the phase relations.

Table 4-4: Experimental data of cavity focusing.

	Cavities off		Cavities on	
	Δx_0 (mm)	Δy_0 (mm)	Δx (mm)	Δy (mm)
Accel-Accel	10.5	0.0	8.95	-1.24
Decel-Accel	10.29	0.0	6.67	0.14
Accel-Decel	10.29	0.0	7.97	0.24

The energy of the beam out of the injector was measured by the 45 MeV spectrometer. The gradients of the two cavities were obtained from the control system read-backs. The phases of the cavities were set by the autophasing scheme. The uncertainty of the gradient calibration is about 5% and about 10~20 degrees in the crest phase.

4.2.2 Experimental results on cavity focusing

The cavities were powered to 5 MV/m. The control system read-backs of the gradients are GSET=5 MV/m and GMES=4.969 MV/m and 5.007 MV/m respectively for the two cavities. GSET is the set value and GMES is the measured value. The initial beam energy is 42 MeV. The cavities were arranged in Acceleration-Acceleration, Deceleration-Acceleration, and Acceleration-Deceleration modes. Data taken for each of these three settings are shown in Table 4-4. In the Accel-Accel mode, the normal quadrupoles cancel. The change in Δx is solely due to the azimuthal focusing. The change in Δy is due to the skew quad coupling. Converted into the transverse momentum, we have for the azimuthal focusing at 45 MeV for one cavity F=1.07×10^{-3} MeV/c/cm and the skew quadrupole S=-0.86×10^{-3} MeV/c/cm.

In the Decel-Accel mode, the normal quadrupoles add and are focusing in the x plane. The change in Δx is a combined result of the azimuthal focusing and the normal quad focusing. The total transverse kick is $\Delta P = 2.2 \times 10^{-3}$ MeV/c/cm. The azimuthal focusing is in this case approximately the same as in the previous one. The strength of the normal quad for one cavity is Q=1.17×10^{-3} MeV/c/cm. The skew quadrupoles

Table 4-5: Results of the numerical simulation and the experimental measurements of the cavity focusing at 42 MeV.

	Numerical simulation (10^{-3} MeV/c/cm)	Experimental measurement (10^{-3} MeV/c/cm)
Azimuthal focusing	-1.08	-1.07
Normal quadrupole	1.25	1.17
Skew quadrupole	-1.15	-0.86

cancel in this setting as expected.

In the Accel-Decel mode, the normal quadrupoles add and are defocusing in the x plane. The azimuthal force is focusing. At about 42 MeV, the amplitudes of the azimuthal focusing and the normal quad are comparable but with different signs. The cancellation between them should hold Δx at the beam monitor position approximately the same as before the cavities were turned on. The data in Table 4-4 do not show this. Compared with the Accel-Accel case, the norm quad is shown focusing. This is contrary to the result of Decel-Accel and is contrary to the numerical simulation. Even though the multipoles are functions of phase, a 10 degree phase offset from the crest phase would not change the sign of the normal quad. In the Accel-Decel mode, cancelling exists between the azimuthal focusing and the normal quad. Δx measured at the beam monitor should not be smaller than in the Accel-Accel case. The cause of this inconsistency is not known. Further investigations are planned. Despite the inconsistency in the normal quad focusing in this set of data, the data for the skew components show cancellation as expected.

The cavity azimuthal focusing and quadrupole (normal and skew) strengths were calculated from the experimental data given in Table 4-4. Since the data for the Accel-Decel mode are questionable, this set was not used in the calculation. Table 4-5 shows the results of numerical simulation of the focusing effects of the cavity at initial energy of 42 MeV and the experimental results. The experimental results for the azimuthal focusing and the normal quad agree with the numerical simulation to within 7%. The skew quad agrees to within 25%.

The uncertainty of the position measurement is approximately 0.15 mm. This corresponds to a transverse momentum of 0.18×10^{-3} MeV/c/cm. The $\pm 10^0$ RF phase uncertainty induces errors to the multipoles are $\Delta F = \pm 2.5\%$, $\Delta Q = \pm 34\%$, and $\Delta S = \pm 19\%$. The uncertainties of the measurements are $\delta F = 17\%$, $\delta Q = 38\%$, and $\delta S = 25\%$. The discrepancy between the experimental results and the numerical simulation is within the accuracy of the measurement. Admittedly, one set of the experimental data appears spurious. Unfortunately, the experimental run was limited by programatic constraints so no further experimental data available.

4.3 Cavity Misalignment Evaluations

The misalignments of the cavity can be measured by measuring the cavity steering versus the RF phase. The impact of either tilt or offset misalignments on the beam is the same, that is, to steer the beam off axis. The offset-misalignment steers the beam via the cavity focusing and it is small as long as the offset is small. The tilt-misalignment projects the axial acceleration field onto the transverse plane. The steering from this transverse field is significant when the tilt angle reaches the order of milli-radians. The steering is proportional to the tilt angle and is a function of the RF phase. We will evaluate, in the following sections, the tilt misalignment of the cavities from the data presented in section 4.1.2. We will refer hereafter to the tilt-misalignment as the misalignment.

The steering angle of the misalignment along has the following form

$$\xi(\phi) = \frac{0.5\alpha G_0 \cos(\phi)}{E_0 + 0.5 G_0 \cos(\phi)} \qquad (4-100)$$

where E_0 is the initial energy, G_0 is the gradient, ϕ is the RF phase ($\phi = 0$ corresponds to maximum acceleration, or on crest), and α is the misalignment of the cavity.

$\xi(\phi)$ is symmetric about the crest phase. Knowing $\xi(\phi)$ at the crest phase, the cavity misalignment is then obtained as

$$\alpha = \frac{E_0 + 0.5G_0}{0.5G_0}\xi(0) \qquad (4-101)$$

Things become more complicated in the CEBAF 5-cell cavity where the coupler fields also steer the beam. In this case, the measured data are the combined effects of cavity misalignment and coupler steering. If both had the same RF phase dependence, one would not be able to isolate the effect of the misalignment. However, numerical simulation and experimental measurement demonstrate that the coupler steering is about 58^0 off crest. This phase difference enables us to separate the misalignment steering from the coupler steering.

Coupler-steering is well localized. The angle of coupler steering is, at moderately high energy, approximately

$$\zeta(\phi) = \frac{D_0 \cos(\phi + \phi_0)}{E_0 + 0.5G_0 \cos(\phi)} \qquad (4-102)$$

where ϕ_0 is the phase offset of the coupler steering, and D_0 is the dipole strength of the steering. Let $\psi(\phi)$ be the experimental result of the cavity steering. The contribution from the misalignment is

$$\xi(\phi) = \psi(\phi) - \frac{D_0 \cos(\phi + \phi_0)}{E_0 + 0.5G_0 \cos(\phi)} \qquad (4-103)$$

Eq. (4-103) shows the ideal case for finding ξ. In reality, the numerical simulation has a small discrepancy from the experimental result, and Eq. (4-103) does not give a purely symmetric $\xi(\phi)$. Careful adjustment is needed to find the symmetric part of ξ. Based on experience with the numeric modelling of the cavity, the discrepancy is likely be the result of errors in the boundary condition applied to the FP coupler. MAFIA calculations show that the strength of the coupler fields is sensitive to the boundary condition applied to the open side of the coupler, while the phase dependence of the coupler fields is not as sensitive. In Fig. 4-25 are shown the two curves of the dipole strengths with different coupler lengths, or short positions. The maximum strength defers by an amount of 30% due to the different coupling strengths for different shorts. The phases are within a 2^0 deviation. The phase relation is well defined because of the dimension of the coupler in the z direction is small. The numerical simulation has good accuracy on the RF phase dependence of the steering, even if the boundary condition is not appropriately imposed on the open end of coupler. Since the numerical result agrees with experiment to better than 30%, the phase deviation of the numerical simulation should be much smaller than 2^0. The discrepancy between the numerical and the experimental results is mainly due to the boundary condition error. The error induced by the boundary error mainly affects the amplitude of the steering. This justifies scaling the numerical values in Eq. (4-103) to make the difference $\xi(\phi)$ a symmetric function of ϕ.

4.3.1 Misalignment of the seventh cavity in the second cryomodule of the injector

The misalignment of the seventh cavity in the second cryomodule of the injector is evaluated from the experimental data shown in Fig. 4-22. Since the data presented in the figures are the positions of the beam relative to the position of the crest phase, the calculated $\xi(\phi)$ will have a vertical offset, but this offset does not affect the misalignment calculation. Since there is no steering due to the cavity misalignment at RF phases $\pm 90^0$ away from the crest phase, the offset can be determined and the $\xi(\phi)$ curve can be corrected. The symmetric $\xi(\phi)$ functions are obtained by scaling the numerical data in Eq. (4-103) by a factor of 1.123 for Fig. 4-22*a* and 1.047 for Fig. 4-22*b*. The results are shown in Fig. 4-26. The curves are fitted with cosine curves, shown in dashed lines. The misalignment angles calculated for the two measurements are 1.65 mrad and 1.93 mrad respectively.

4.3.2 Errors in the misalignment evaluation

There are several uncertainties in the experimental measurements which may cause errors in the evaluation of the misalignment.

Instamatic measurement of the beam position has an error of about 0.5 mm. This contributes to a misalignment error of about 0.2 mrad.

The phasing of the cavity by use of the 45 MeV spectrometer has an uncertainty of about $\pm 2^0$. Let $\Delta\phi$ be the phase error in the experimental measurement. The actual cavity steering $\zeta_0(\phi)$ and the experimental result of the steering $\zeta_1(\phi)$ have the following form

$$\begin{aligned} \zeta_0(\phi) &= \frac{D_0 cos(\phi+\phi_0)}{E_0+0.5G_0\cos(\phi)} && \text{(4-104)} \\ \zeta_1(\phi) &= \frac{D_0 cos(\phi+\phi_0+\Delta\phi)}{E_0+0.5G_0\cos(\phi+\Delta\phi)} && \text{(4-105)} \end{aligned}$$

The scaling method used to find the symmetric ξ in the previous section requires

$$\begin{aligned} s\cdot\zeta_0(-90^0) &= \zeta_1(-90^0) \\ s\cdot\zeta_0(90^0) &= \zeta_1(90^0) \end{aligned}$$

The scaling factor can be obtained as

$$s = \frac{\sin(\phi_0+\Delta\phi)}{\sin(\phi_0)} \qquad (4-106)$$

The error in the misalignment calculation is directly related to the difference $\zeta_0(\phi) - s\cdot\zeta_1(\phi)$ and it is

$$\zeta_1(\phi) - s\cdot\zeta_0(\phi) = -\frac{D_0\cos(\phi)\sin(\Delta\phi)}{(E_0+0.5G_0\cos(\phi))\sin(\phi_0)} \qquad (4-107)$$

which has the same form as the steering angle of the misalignment. The equivalent misalignment due to this error is

$$\Delta\alpha = \frac{E_0+0.5G_0}{0.5G_0}(\zeta_1(0)-s\cdot\zeta_0(0)) = -\frac{D_0\sin(\Delta\phi)}{0.5G_0\sin(\phi_0)} \qquad (4-108)$$

At the gradient of 5 MV/m, the maximum dipole strength D_0 is 0.0139 MeV/c. For $\Delta\phi = 2^0$, $\Delta\alpha$ is about 0.22 mrad.

The beam offset in the cavity cannot be determined within to 1 mm. If the particle is not on the axis of the cavity, the effects of the fields of the higher-order components of the cavity are included in the experimental data $\psi(\phi)$. The transverse momentum impulse to the beam from the deflection in the x plane can be written as

$$\Delta P(\phi) = D(\phi) + F(\phi)x + Q(\phi)x + S(\phi)y \qquad (4-109)$$

where D, F, Q, and S are coefficients of the dipole, azimuthal focusing, quadrupole, and the skew quadrupole components, and they are independent of energy if the energy is high enough save for F, which varies as $\frac{1}{E}$. The maximum of D, D_{max}, is about an order of magnitude larger then the maximum values of the remaining coefficients. To be exact, if x and y are in centimeters, D_{max} is about 5 times larger than Q_{max}, 8 times larger than S_{max} and, for $E = 20MeV$, 8.5 times larger than the maximum and minimum difference of F as shown in Figs. 3-16, 3-17, 3-19, and 3-20 in chapter 3. If the beam is off axis, the quadrupole fields act the same way as the dipole fields. The only difference is that the steering in the quadrupole is proportional to the offset. If the RF phase dependence is the same as the dipole, the offset of the beam will only cause error in the magnitude of the dipole steering and it will not introduce any error to the calculation of the misalignment. As the numerical simulation indicates that there is a -11^0 phase shift, the mechanism discussed above introduces error to the evaluated misalignment. Even though the phase shift is large, the error is small since the steering effect is smaller for the quadrupoles. The maximum quadrupole kick is $2.8 \times 10^{-3}x$ MeV/c. From Eq. (4-108), $\Delta\alpha = 0.25x$ mrad. For $x = 0.1$ cm, the error is 0.03 mrad.

The azimuthal focusing $F(\phi)$ is approximately symmetric about the crest phase at 20 MeV; F_{max} occurs at the crest phase and F_{min} occurs at $\pm 90^0$ off crest. Its phase relation is similar to the misalignment steering. The difference of F_{max} and F_{min} induces an error which, at 20 MeV, is $F_{max} - F_{min} = 1.35 \times 10^{-3} x$ MeV/c. The error is therefore in general $\frac{F_{max} - F_{min}}{0.5 G_0} = 0.54x$ mrad. For $x = 0.1$ cm, the error is 0.05 mrad.

The normal quadrupole and the azimuthal focusing terms are correlated. For the case of a downstream FP coupler and power fed from the negative x direction, the misalignment contributions of these two terms add. The total effect of the normal quadrupole and the azimuthal focusing for $x = 0.1$ cm is 0.08 mrad.

The skew quadrupole steering is due to the y displacement of the beam. The phase dependence of $S(\phi)$ is very different from $D(\phi)$. To estimate the maximum effect of the skew quadrupole, we assume that this contribution is symmetric about the crest phase with a maximum S_{max} of $1.7 \times 10^{-3} y$ MeV/c. The induced misalignment error is about $0.7y$ mrad. For $y = 0.1$ cm, the error is 0.07 mrad.

The total uncertainty on the misalignment calculation is about ± 0.32 mrad.

The correctors used to center the beam are not well calibrated. The strengths of the correctors were not well known at the time of this measurement. Non-zero correctors cause problems in the evaluation of the misalignment. The kicks from these correctors depend on the momentum of the particles and are symmetric about the crest phase. They are not separable from misalignment effects. The misalignment estimated in section 4.3.1 must include the effects of errors in the correctors.

As a rough estimate of the corrector contribution to the misalignment, we noticed that the beam was initially offset at the location of the viewscreen by about -5.5 mm in the x axis when on crest. This offset was set to prevent the beam from moving off the view screen while the RF phase is scanned. Noting that the coupler steering makes about a 7 mm offset at a distance of about 17 meters at crest phase, the corrector is estimated to have a strength of 12 mm, in terms of beam offset. The energy of the beam drops by 10% as the phase is changed from the crest to zero acceleration. The deviation of the corrector steering is equivalent to a cavity misalignment of 0.5 mrad, and it is the same sign as the misalignment obtained in section 4.3.1. The misalignment given in section 4.3.1 may therefore have been over estimated by about one half milli-radian.

4.3.3 Conclusions

Numerical simulation of cavity steering and focusing agree with the experimental results. This confirms that numerical modelling of the CEBAF 5-cell cavity is a valid representation of the actual cavity. The misalignment of the cavity estimated is within the assembly specification of the cavities in the cryomodule – a couple of milli-radians ($1.65 \pm 0.32 - 0.5$ mrad) for the cryomodules built for the injector prior to upgrade.

The above studies are based on a limited amount of experimental data available on cavity steering and focusing. Further experiments have been planned to measure the cavity steering and misalignment of selected cavities in the CEBAF north linac. The correctors will be calibrated and higher-resolution beam monitors will be used for the position measurements; this will improve the accuracy of the calculated misalignments.

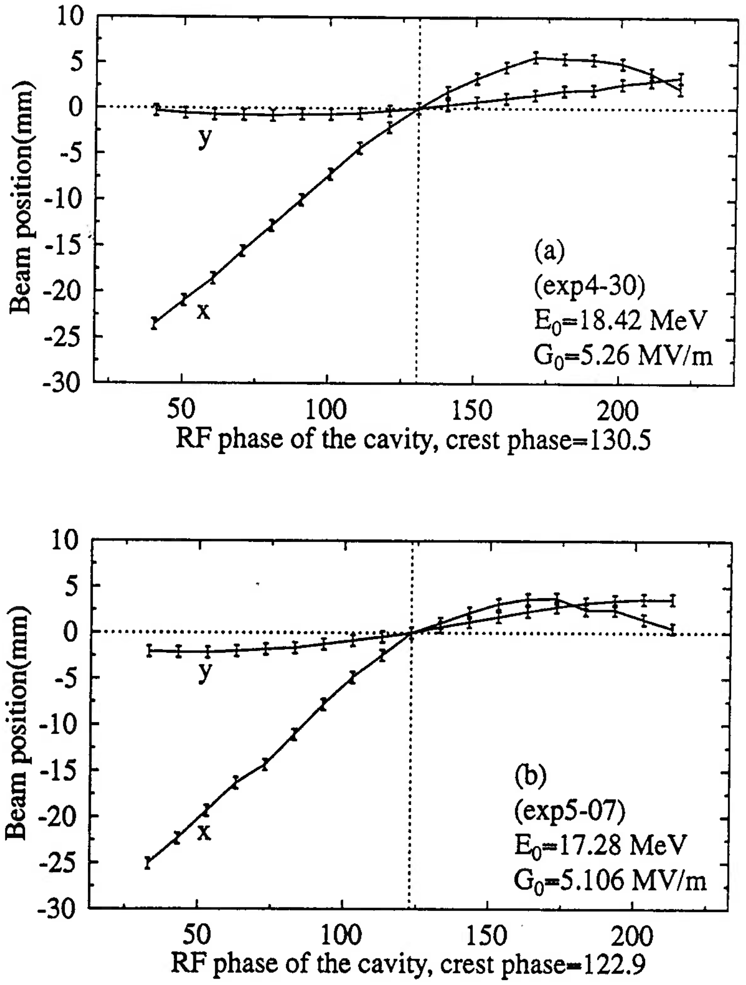

Figure 4-22: The experimental results of the cavity steering. a) (exp4-30) E_0=18.42 MeV, G_0=5.26 MV/m; b) (exp5-07) E_0=17.28 MeV, G_0=5.106 MV/m.

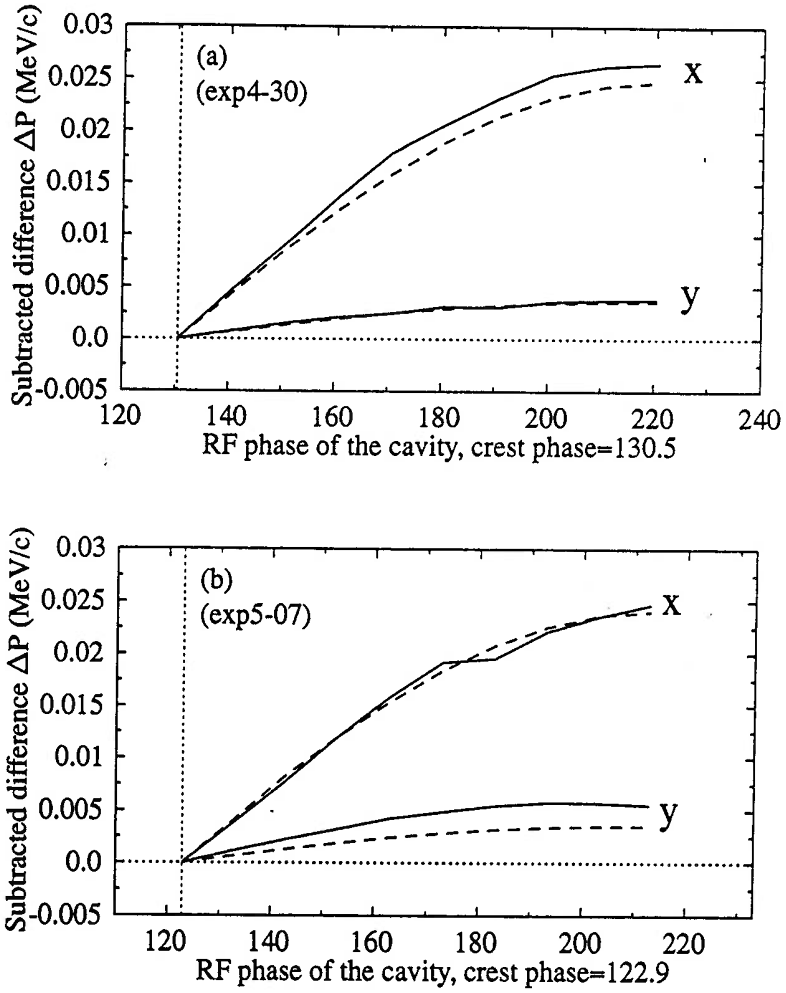

Figure 4-23: The experimental results (solid lines) after correction and the results of the PARMELA simulations (dashed lines). a) (exp4-30) E_0=18.42 MeV, G_0=5.26 MV/m; b) (exp5-07) E_0=17.28 MeV, G_0=5.106 MV/m

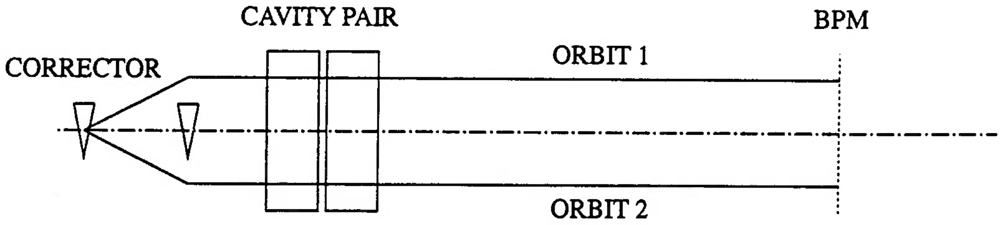

Figure 4-24: The reference orbits for the cavity-focusing measurements.

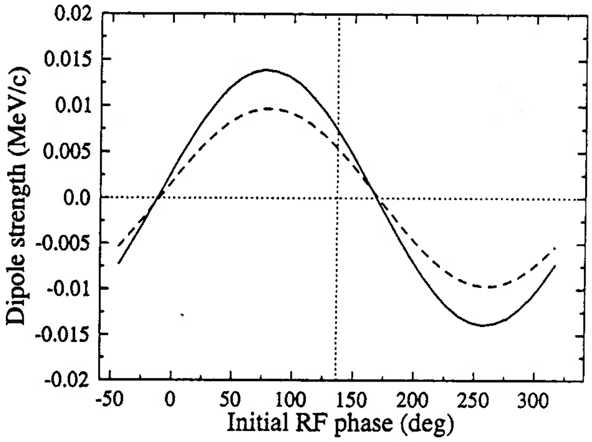

Figure 4-25: Numerical results for different boundary conditions imposed on the open end of the coupler

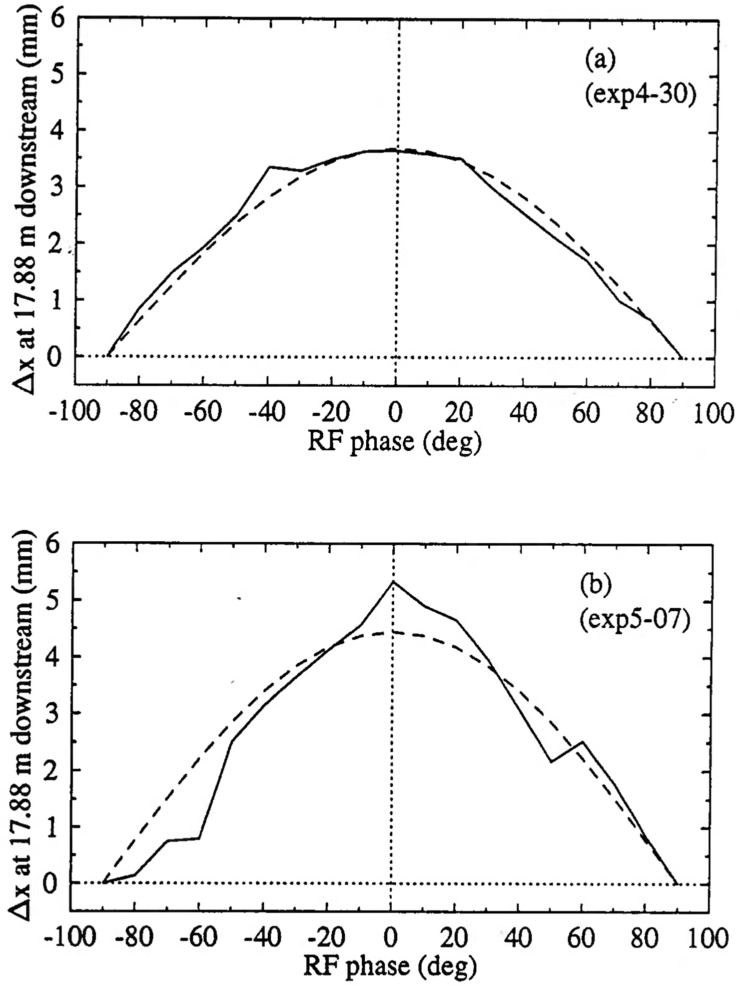

Figure 4-26: Beam displacement due to the steering effect of the cavity misalignment. Solid lines: experimental data; Dashed lines: Cosine curve fitting. a) (exp4-30) Calculated misalignment is 1.65 mrad; b) (exp5-07) Calculated misalignment is 1.93 mrad.

Chapter 5

Beam Dynamics in the CEBAF Linacs

In chapter 3 we studied particle beam dynamics in a single cavity. In this chapter, we will study beam dynamics of a bunch of particles in the CEBAF linacs, which consist of a train of superconducting cavities and optical elements such as quadrupoles and dipoles. The bunch is finite in both the transverse and the longitudinal directions. Individual particles experience different RF fields since the fields are functions of position and the RF phase. To study the collective motion of the particles we observe their dynamics in phase space and study their "trajectories" in term of β functions. Each particle at any point along the beam line is represented by a point in the six-dimensional phase space with coordinates $(x,\ p_x,\ y,\ p_y,\ \ell,\ \delta)$. Liouville's theorem states that under the influence of conservative forces, the density of the particles stays constant in this phase space. Often our interests are the phase sub-spaces of the transverse planes. The six-dimensional phase space is projected into two-dimension phase sub-spaces-namely $(x,\ p_x)$, $(y,\ p_y)$. The emittance of the beam is defined as the area of the phase sub-space divided by π. The emittances defined in the $(x,\ p_x)$ and $(y,\ p_y)$ planes are called normalized emittances (ϵ_n). As a convention, in calculating the normalized emittance, $\beta\gamma x'$ is used instead of the momentum (β here is v/c). An alternative definition of the emittance is in the $(x,\ x')$ and $(y,\ y')$ planes. The emittances defined in these planes are called geometric or unnormalized emittances (ϵ_{un}). Since $x' = p_x/p_z$ and $y' = p_y/p_z$, the unnormalized emittance damps as $1/\gamma$. In this chapter, we will use the normalized emittance unless otherwise specified. The β functions (not to be confused with v/c) are the properties of the beam lines. In the storage rings, they are uniquely defined.

In transport lines, the β functions are defined by both the lattice and the initial beam conditions. The motion of the particles in a bunch are confined within an envelope defined by $\sqrt{\epsilon_{un}\beta}$.

The emittances and the β functions may be perturbed by multipole fields of the cavities. In "uncoupled" cases, the emittances in the (x, p_x) and (y, p_y) planes are constant through out the beam line. In the case of having "cross-plane coupling", the emittances are no long conserved. There are two kinds of coupling in the CEBAF cavities. Dipole steering, which couples the longitudinal to the transverse due to the finite longitudinal spread of the beam, creates a head-tail effect. The particles at different longitudinal positions experience different transverse steering, and the projected emittance increases. Head-tail emittance degradation is proportional to the bunch length. The skew component of the cavity fields, on the other hand, generates $x-y$ coupling. Particles offset on one axis are steered by the skew fields in the direction of the other axis, which increases the projected emittance. It is clear that the skew coupling emittance growth depends on the transverse dimension of the beam. The normal cavity quadrupole field and the cavity azimuthal focusing provide extra focusing to the beam, and do not degrade the emittance. These effects can be compensated by adjusting the strength of the lattice elements.

The emittance is a very important parameter of the beam. The emittance specification for the CEBAF accelerator is 0.1 cm·mrad rms at 4.045 GeV. Since cross-plane coupling and cavity focusing exist, we wish to know the emittance growth due to the couplings as well as the impact of the cavity focusing on the lattice functions in the CEBAF linacs. The numerical simulations in this chapter are performed by use of the modified version of PARMELA.

5.1 Head-tail effects

During normal operation, the phase offset of the dipole steering from the crest phase generates differential kicks within the bunch with the strength of 2.14×10^{-4} MeV/c/degree in the x plane and 3×10^{-5} MeV/c/degree in the y plane. The differential movement of the head relative to the tail of the bunch results in an effective emittance growth.

In a cavity-pair, the dipole steering to the center of the bunch cancels in the x direction and adds in the y direction while the head-tail effect adds in the x direction and cancels in the y direction. This is illustrated in Fig. 5-27. Expressing the transfer function of the cavity in terms of a matrix [27], we have in the (x, p_x, ℓ) space

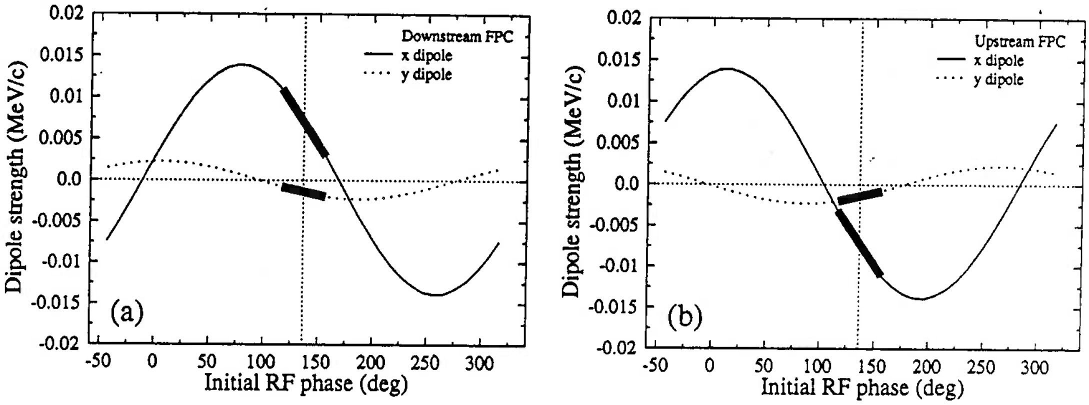

Figure 5-27: Differential steering of a bunched beam in cavities with different FP coupler locations. a) Downstream FP coupler; b) Upstream FP coupler. Gradient=5 MV/m.

$$M = \begin{pmatrix} 1 & a & 0 \\ -\frac{1}{f} & 1 & \alpha \\ 0 & 0 & 1 \end{pmatrix} \qquad (5-110)$$

where

$$a = \frac{cL}{\Delta E}\ell n[\frac{E_0 + \Delta E + cp_z(L)}{E_0 + cp_z(0)}]$$

and $\alpha = 2.14\times10^{-4}\times\frac{G_0}{5}$ MeV/c/degree in the x plane and $3\times10^{-5}\times\frac{G_0}{5}$ MeV/c/degree in the y plane. For a cavity-pair

$$M_{1,2} = M_1 \cdot M_2 = \begin{pmatrix} 1 - \frac{a_2}{f_1} & a_1 + a_2 & a_2\alpha_1 \\ -\frac{1}{f_1} - \frac{1}{f_2} & 1 - \frac{a_1}{f_2} & \alpha_1 + \alpha_2 \\ 0 & 0 & 1 \end{pmatrix} \qquad (5-111)$$

The emittance growth due to the head-tail effect is approximately

$$\Delta\epsilon = \frac{\sigma_l^2}{2\epsilon_0}(\sigma_x^2(\alpha_1 + \alpha_2)^2 + \sigma_{x'}^2(a_1 + a_2)^2(\alpha_1 + \alpha_2)^2) \qquad (5-112)$$

where σ_l is the rms bunch length.

In a cryomodule, the cavity-pairs with different FP coupler polarities have opposite head-tail differential steering, and they tend to cancel. Under the thin lens approximation (for example at high energies), the transfer matrix of one cryomodule is

$$M = \begin{pmatrix} 1 & 0 & 0 \\ -\sum \frac{1}{f_i} & 1 & \sum \alpha_i \\ 0 & 0 & 1 \end{pmatrix} \qquad (5-113)$$

where, under nominal operation,

$$\begin{aligned} \sum \alpha_i &= \alpha_1 + \alpha_2 - \alpha_3 - \alpha_4 - \alpha_5 - \alpha_6 + \alpha_7 + \alpha_8 \\ &= \frac{2.14 \times 10^{-4}}{5}(G_1 + G_2 - G_3 - G_4 - G_5 - G_6 + G_7 + G_8) \qquad \text{(5-114)} \end{aligned}$$

in the x plane and

$$\begin{aligned} \sum \alpha_i &= \alpha_1 - \alpha_2 - \alpha_3 + \alpha_4 - \alpha_5 + \alpha_6 + \alpha_7 - \alpha_8 \\ &= \frac{3 \times 10^{-5}}{5}(G_1 - G_2 - G_3 + G_4 - G_5 + G_6 + G_7 - G_8) \qquad \text{(5-115)} \end{aligned}$$

in the y plane. The head-tail effect at high energies depends only on the uniformness of the gradient of the cavities. If the weighted average, Eqs. (5-114) and (5-115), is small, the head-tail effect may be negligible. If the cavities in the cryomodule are not powered uniformly, the head-tail related emittance growth may occur. Should this happen, it is suggested to adjust the gradients of the cavities to reduce the quantities in Eqs. (5-114) and (5-115). At low energies, the cavities should be treated as thick lenses, and the cavity focusing reduces the cancellation of the head-tail effects between the cavity-pairs.

5.2 Skew coupling

The skew fields of the cavity couple the x motion of the particle to the y motion and vise versa. A particle with offset of y in the y direction in the skew fields with skew strength of S will get a momentum gain of $\Delta p_x = S \cdot y$ or $\Delta x' = \frac{S \cdot y}{p_z}$ in the x direction. The unnormalized rms emittance, defined as

$$\epsilon_{un} = \sqrt{< x^2 >< x'^2 > - < xx' >^2} \qquad (5-116)$$

becomes

$$\begin{aligned} \epsilon_{1,un} &= \sqrt{\epsilon_{0,un}^2 + \left(\frac{S}{p}\right)^2 < \sigma_x^2 >< \sigma_y^2 >} \\ &= \sqrt{\epsilon_{0,un}^2 + \left(\frac{S}{p}\right)^2 \epsilon_{x,0}\epsilon_{y,0}\beta_x\beta_y} \qquad (5\text{-}117) \end{aligned}$$

The $x - y$ coupling effect on the emittance is sensitive to the betatron functions in the cavity.

During normal operation, the skew component does not depend on the polarity of the FP couplers. The skew strength has the same sign all the way through the whole linac. However, they do not always add. The collective effect of the skew coupling in multiple cavities not only depends on the β functions, but also on the betatron phase advance of the lattice, which is defined as

$$\psi = \int \frac{1}{\beta} ds \qquad (5-118)$$

The focal length of the skew, which is approximately

$$f_{skew} = 9p \qquad (5-119)$$

where p is the momentum of the particle in MeV/c and f is in meters, is in general large in the CEBAF linacs. For example at 45 MeV, the focal length is about 400 meters. Observing an individual particle which under goes betatron oscillations along the beam line, the trajectory without skew perturbation is

$$\begin{pmatrix} u \\ u' \end{pmatrix} = \begin{pmatrix} \sqrt{\frac{\beta}{\beta_0}}(\cos(\psi) + \alpha_0 \sin(\psi)) & \sqrt{\beta\beta_0}\sin(\psi) \\ \frac{\alpha_0 - \alpha}{\sqrt{\beta\beta_0}} \cos(\psi) - \frac{1 + \alpha\alpha_0}{\sqrt{\beta\beta_0}} \sin(\psi) & \sqrt{\frac{\beta_0}{\beta}}(\cos(\psi) - \alpha \sin(\psi)) \end{pmatrix} \begin{pmatrix} u_0 \\ u'_0 \end{pmatrix} \tag{5 - 120}$$

If the wavelength of the betatron oscillation is smaller than the focal length of the skew fields, the skew kick on one axis due to the offset on the other axis changes sign when the phase advance exceeds 90^0, and the accumulated skew effect begins to cancel. This is expected in the first pass of the north linac where the phase advance is strong, which is 60^0 per cryomodule or 120^0 per FODO period. In the higher energy passes, the phase advances are small. The skew effects generally add up.

To higher order, head-tail effect also couples to the x and y planes. This coupling is small. The 3-D cavity modeling in PARMELA takes account of all these effects.

5.3 Beam optics in the injector

The injector starts with a 100 keV DC electron gun. The chopper, buncher and the capture sections segment the beam into bunches and accelerate it to 500 keV. The bunches are in the order of 1^0 RF phase long. The cryounit, which consists of two superconducting cavities, accelerates the beam up to 5 MeV. Through a transport line about 13 meters in length, the beam enters two full cryomodules, each of which consists of 8 superconducting cavities. The beam is accelerated to 45 MeV. It is then transported through a quadrupole telescope and an injection chicane to the entrance of the north linac, about 64 meters downstream.

The cryounit consists of two cavities, each of which has its own power supply system for operational flexibility. They are connected to each other on their FP coupler side with a 9.393 cm niobium adapter. The distance between the nearest end-cells of the cavities is 25 cm, which is one and a quarter of wave lengths. The two fundamental couplers have the same orientation. This configuration cancels the x dipole steering when the cavities are in maximum acceleration, but enhances the head-tail effect. The head-tail effect is strong in the unit since there is no local sources to provide local cancellation of the head-tail effect generated by the cavity-pair.

The cryomodule consists of four cavity-pairs or cryounits. The separation between the cavity-pairs is 1.911 meters from center to center. The two end cavity-pairs have the same polarity; both have power fed in from the negative x direction. The power to the two middle cavity-pairs is fed in from the positive x direction. This feed geometry is arranged so as to reduce the emittance degradation from the head-tail effect [26].

Our simulation starts from the entrance of the cryounit, which is the first superconducting unit in the beam line. The beam energy at this point is 500 keV. The design beam parameters are

$$\beta_x = 24.385 \text{ m} \qquad \alpha_x = -7.659$$
$$\beta_y = 31.391 \text{ m} \qquad \alpha_y = -12.152$$

The electron gun produces a normalized rms emittance of 0.018 cm$\cdot$ mrad which is more than five times smaller than the specification at the end of the linac. The full, $4\sigma_z$, bunch length is 1.6^0. The RF phase of the first superconducting cavity of the cryounit is set back by 7.5^0 from the crest phase of 84.023^0, to adjust the transverse focusing, so that the beam requires no downstream quadrupole matching. This feature has been observed in the experiments [11]. This backphasing also provides some bunching power to the beam. At the entrance of the cryomodule, the bunch length was shrunk to 0.9^0.

The β functions and the normalized emittances in the injector are shown in Fig. 5-28. It is shown that the emittances in both planes grow by more than 70% in the cryounit. In the cryounit, the head-tail effects of the two cavities add. The fact that the geometric emittance is large at 2.5 MeV reduces the effect of head-tail emittance growth. At the location of the two FP couplers, $p = 2.5$ MeV/c, $\beta_x = 43.7$ meters, $\alpha_x = -7.48$, the 4σ

uncoupled geometric emittance is $\epsilon_4 = 0.0144$ cm·mrad. The maximum x' in the phase space is

$$x' = \sqrt{\frac{\epsilon_4(1+\alpha_x^2)}{\beta_x}} = 0.43 \text{ mrad} \qquad (5-121)$$

For a 1.5^0 bunch, the total $\delta x'$ due to the head-tail effect at $p = 2.5$ MeV is

$$\Delta x' = 1.5 \times \frac{1.25 \times 10^{-4} G_1 + 2.14 \times 10^{-4} G_2}{5P} = 0.20 \text{mrad} \qquad (5-122)$$

which produces about 24% of emittance growth.

Since the beam in the cryounit is large, 1 cm full width, the skew effect is expected to be strong. The skew strength in the first cavity at 7.5^0 backphasing is about 0.0005 MeV/c/cm and it is -0.0015 MeV/c/cm in the second cavity. The average β functions are β_x=43 m and β_y=58 m in the cryounit. The output energy is 5 MeV. From Eq. (5-117), the emittance growth due to the skew coupling is approximately 41%.

The β functions are small in the cryomodules which results in weak skew coupling and large phase advance. These two factors reduce the accumulated skew coupling. The head-tail effects also undergo cancellation amoung the cavity-pairs in the modules. The emittance growth in the two cryomodules is small, about 13% in both planes.

If the design injection betatron envelope function values are not provided at the entrance of the cryounit, the β functions in the injector will be changed. The skew-coupling emittance growth, which is sensitive to the β functions will change as well. Since the azimuthal focusing of the cavity depends linearly on, and is sensitive to, the RF phase in the vicinity of crest at 500 keV (Fig. 3-16), some of the mismatch may be corrected by adjusting the RF phase of the first cavity in the cryounit. Since the azimuthal focusing focuses in both planes, the correctable mismatch must also be symmetric. Asymmetric mismatches can be corrected by employing the quadrupoles downstream from the cryounit, which are normally turned off due to the strong focusing of the cavity. Here we examine the cases with symmetrically mismatched beams and the corrections of the emittance growth by changing the RF phase of the cavity.

The first two examples are of mismatches of initial αs, assuming the initial βs are matched. It is shown that for an initially less divergent beam with $\alpha_{x,0} = -3.8$, $\alpha_{y,0} = -6.1$, the emittances grow in the two cryomodules by a factor of 3.5, (Fig. 5-29*b*(*i*)). The β functions in the first cryomodule are large, (Fig. 5-29*a*(*i*)). Skew coupling is strong in the first cryomodule. To reduce the β functions in the first cryomodule, more backphasing is needed. Fig. 5-29*a*(*ii*) and 5-29*b*(*ii*) show the corrected results by phasing the cavity at 73.023^0, which is backphased 11^0 from the crest phase of 84.023^0. The β functions and the emittances are improved. Figs. 5-30*a*(*i*) and 5-30*b*(*i*) show the β functions and the emittances for another case of mismatched beam with $\alpha_{x,0} = -11$, $\alpha_{y,0} = -17$. The emittance growth in the two cryomodules in this case is small, however, the β_y function is large at the exit of the second cryomodule. By adjusting the RF phase of the cavity to 78.523^0, 5.5^0 backphased, the β_y function is reduced. The β functions and the emittances with the new RF phase are shown in Figs. 5-30*a*(*ii*) and 5-30*b*(*ii*).

For a beam initially mismatched with smaller β functions, $\beta_{x,0} = 12.385$ m, $\beta_{y,0} = 16.391$, the emittances grow in the two cryomodules by a factor of 2, Fig 5-31*b*(*i*). The cavity focusing is shown not large enough in this case, which results in large β functions in the cryomodules. Fig. 5-31*a*(*i*). The RF phase of the cavity can be adjusted to get more focusing. At an RF phase of 80.023^0, which is backphased 4^0 from the crest phase of 84.023^0, the β functions and the normalized emittances are obtained as shown in Figs. 5-31*a*(*ii*) and 5-31*b*(*ii*). The β functions are smaller in the cryomodules and the emittance growth is reduced.

For a beam initially mismatched with larger βs, $\beta_{x,0} = 36.385$ m, $\beta_{y,0} = 45.391$, the focusing in the cryounit is strong. The waist forms too early and the beam enters the cryomodule with a strong divergence. The β functions in the cryomodule drop down more slowly than in the nominal case. The emittance growth is strong, as shown in Figs. 5-32*a*(*i*) and 5-32*b*(*i*). The emittances grow in the two cryomodules by a factor of

2.4. Reducing the focusing of the cavity by phasing it at 74.523^0,which is backphased 9.5^0 from the crest phase of 84.023^0, the new β functions and the emittances are shown in Figs. 5-32$a(ii)$ and 5-32$b(ii)$. The emittance growth in the two cryomodules is reduced to nearly zero.

Experiments [28] have shown that the geometric emittance at 45 MeV is five times smaller than that at 5 MeV instead of nine times smaller as would be expected from the adiabatic damping, which indicates a 100% emittance increment in the two cryomodules. This is explainable by the mismatched condition of the beam or by the inappropriate phasing of the first cavity in the cryounit.

To correct the emittance growth due to the asymmetric mismatch of the beam, quadrupoles may be needed to provide proper β functions in the cryomodules. We will not address this circumstance here.

5.4 Beam optics in the north linac

The linac system at CEBAF consists of two linac segments, each capable of supplying a nominal energy gain of 400 MeV, in which up to five beams are accelerated simultaneously. Each linac segment consists of 20 cryomodules. Each cryomodule can supply an acceleration of 20 MeV. Between the cryomodules are room temperature regions 1.3 m in length, each of which contains a set of orbit correcting elements, beam monitors, and a quadrupole. The quadrupoles form a FODO focusing lattice. A FODO period consists of two cryomodule sections. The phase advance in a period is 120^0 for the first pass. The 445 MeV beam from the first pass of the north linac segment is bent 180^0 by the east arc and injected to the south linac where the beam gets another 400 MeV energy increment. The beam is again transported to the north linac through the west arc. The beam is accelerated through five turns in this race-track accelerator. The final energy of the beam is 4.045 GeV. The north and the south linacs are basically the same. In this section, we will study the beam optics of the five passes in the north linac only.

The linac segments contain only full cryomodules, which provide certain cancellation for the head-tail effects. The bunch length in the linac is also small, less than 1^0, or 0.5 mm. The head-tail effects are therefore expected to be small. The accumulated effect of skew coupling depends on the β functions and the phase advance along the beam line. Since the quadrupoles have fixed strength, the β functions and the phase advances are different for each pass because the energy of the beam is increased for each successive pass. Different cross-plane couplings are therefore expected in different passes.

First pass

The injection energy for the first pass is 45 MeV. The initial beam parameters are

$$\beta_x = 41.277 \text{ m} \qquad \alpha_x = 0$$

$$\beta_y = 2.977 \text{ m} \qquad \alpha_y = 0$$

The quadrupole strength to form the FODO lattice with 60^0 phase advance for each cryomodule is $K_q = 1.20913$ with K_q defined as

$$K_q = \frac{B_0/a}{B\rho_0} = 0.2998\frac{\partial B/\partial r[\text{T/m}]}{p[\text{GeV/c}]} \qquad (5-123)$$

The gradient of the quadrupoles is then

$$\frac{\partial B}{\partial r} = 333.556 K_q p \quad \text{G/cm} \qquad (5-124)$$

where P is the momentum of the particle in GeV/c. The first quadrupole in the linac is focusing in the x plane.

Without the effect of the acceleration, the quadrupoles with strengths given by Eq. (5-124) form a FODO lattice. The presence of acceleration changes the situation. The acceleration damps the transverse divergence of the particles by the factor of the ratio of E_{in} and E_{out}. The quadrupole steering is also damped by the same amount. The effective quadrupole strength in the FODO lattice thus becomes

$$K_{q,effect} = K_q \frac{E_{in}}{E_{out}} \qquad (5-125)$$

This damping is strong in the low energy accelerating sections. Use of uniform strength quadrupoles in the accelerating structure will, in general, not yield the designed FODO lattice.

There are exceptions if the accelerating fields are RF fields. The azimuthal focusing of the RF fields may compensate the damped focusing of the quadrupoles. In the first cryomodule of the north linac, the energy increases from 45 MeV to 65 MeV. The effective strength of the first quadrupole is 45/65=0.69 times of the physical value, which is 30% lower than the required. At 45 MeV, the cavity azimuthal focusing has a equivalent of quadrupole strength of 4.17×10^{-2} G·m/cm for one cavity. The integrated focal strength of a cryomodule is 0.334 G·m/cm. The strength of the first quadrupole in terms of field gradient at 45 MeV is 18.15 G/cm. The integrated strength of half the length (7.5 cm) of the quadrupole is 1.36 G·m/cm. The cavity focusing in the first cryomodule is 25% of the strength of the first quadrupole. This is nearly the amount of focusing needed to compensate the damping. The quadrupole fields of the cavity also contribute certain focusing. Given the compensation of the damped quadrupole strength by the focusing provided by the cryomodule, the FODO lattice for the CEBAF linac actually works almost nominally without any modifications. The β functions of the first pass with the uniform K_q FODO lattice in the north linac is shown in Fig. 5-33*a*. The normalized emittance in the linac is shown in Fig. 5-33*b*. There is no significant emittance growth. This is because of the cancellation resulting from the large betatron phase advance. In the first pass, the phase advance is 120^0 per period, which is quite high (Fig. 5-34). From Eq. (5-120), as the phase increases by 90^0, some of the particles will move from one side of the axis to the other side. The skew effects on these particles begin to cancel.

To demonstrate the damping effect of the acceleration, we calculated the β_x functions with the cavity focusing turned off, dotted line in Fig. 5-35. The β function becomes large. By increasing the strength of the first quadrupole strength by 30%, the β function is recovered to the designed FODO lattice function, solid line in Fig. 5-35.

The skew effect does not pose any problem for the first pass beam as long as it is matched to the linac. If the beam is not matched, the β functions will become larger in some portions of the beam line, which will increase the skew coupling and reduce the cancellation. We present here several cases of mismatches to show their impact on the emittance growth.

For an initially diverging beam with $\alpha_{x,0} = \alpha_{y,0} = -1$, the emittance shown in Fig. 5-36 increases by about 40%. The peaks in the β functions generate stronger $x - y$ coupling. The residual cancellation contributes to the emittance growth. A similar situation is found for an initially converging beam. Fig. 5-37 shows the results of an initially converging beam with $\alpha_{x,0} = \alpha_{y,0} = +1$. The emittance growth for this case is about 39%.

Figs. 5-38 and 5-39 show the cases of mismatched β functions. The β functions and the emittance growths in these two cases show relatively less sensitivity to the initial values of $\beta_{x,0}$ and $\beta_{y,0}$ compared to the cases of mismatched αs. It appears important to form waists in both the x and y planes at the center of the first quadrupole to reduce the $x - y$ coupling in the first pass north linac.

Higher passes

The beam is accelerated five times in both the north and the south linacs. The initial energies of the higher passes at the entrance of the north linac are 845 MeV, 1645 MeV, 2445 MeV and 3245 MeV respectively. The beam envelope initial conditions for these beams are $\beta_x = \beta_y = 80$ m, $\alpha_x = \alpha_y = 0$ for 845 MeV and $\beta_x = \beta_y = 100$ m,

$\alpha_x = \alpha_y = 0$ for all other energies.

The FODO lattice was designed for the first pass beam to have 120^0 phase advance per period. As the energy gets higher and higher, the quadrupole focusing and the cavity focusing get smaller and smaller. The β functions for theses passes will not resemble that of the first pass. The betatron oscillation is not as strong and the phase advance will be small. The skew coupling will add.

The β functions and the normalized emittances of these four passes are shown in Figs. 5-40-5-43. The emittances in these four passes grow in the range of 25-38%. For the 845 MeV beam, the emittance rolls up and reaches a maximum at about 110 m and then falls down to a minimum at 160 m and then up again. For the 1645 MeV beam, the emittance has a maximum at 160 m. For the 2445 MeV and 3245 MeV beams, there is no cancellation of the skew couplings. These effects are due to the variation in phase advances, Fig. 5-44, amoung the four passes. The phase advance for the 845 MeV beam through the full linac is over 200^0. When the phase becomes more than 90^0, skew cancellation begins. When the phase advance is over 180^0, the addition again overtakes the cancellation. For the 1645 MeV pass, skew coupling has a turning point at the 90^0 phase advance. For higher energy passes, the phase advances are less than 90^0. The emittance grows without cancellation.

The emittance growth for mismatched beams was also studied. For the higher energy passes, the results are similar. We present here the results for the 845 MeV beam, which are shown in Fig. 5-45. For an initially diverging beam, the $x - y$ coupling is stronger than in the nominal case. The emittances grow by a factor of 2.28 for $\alpha_{x,0} = \alpha_{y,0} = -1$. For an initially converging beam, the emittance growth is small. With $\alpha_{x,0} = \alpha_{y,0} = +1$, the emittance growth is nearly zero.

Emittance growth due to the β function mismatch is smaller in comparison to the α mismatched cases. The emittances with ±50% mismatched β functions grow only about 38% as shown in Fig. 5-45.

Remarks

In ideal cases, beam envelopes are matched to the linac lattice. The emittance growth in the north linac for the first pass is then nearly zero, and is 25-38% for the higher energy passes. The total emittance growth in the whole machine depends on the phase advance in the arcs and the linacs. A rough estimation gives a factor of two emittance degredation. Since the initial emittance of the beam is several times smaller than the specified final emittance, the diluted emittance remains within tolerances.

If the beams are mismatched, the emittance in each pass depends on the mismatch conditions. It is shown in the simulation that the emittances are more sensitive to α mismatches than β mismatches. In the first pass, an α mismatch on either side of the waist results in emittance growth. It is important for the beam to form a waist at the center of the first quadrupole. In the higher energy passes, the emittance growth is larger for divergent beams and it is smaller for convergent beams. As far as the emittance growth is concerned, convergent beams are preferable to divergent beams.

Should skew coupling becomes a problem in meeting the final emittance specification, there are various corrections. Inserting skew quadrupoles in the beam line is certainly a cure. Appropriately changing the beam matching is also a way of reducing coupling in the higher passes of the linac.

5.5 Beam dynamics in the IR FEL linac

The IR FEL driver linac [29] consists of one full cryomodule, led and followed by quadrupole doublets. The quadrupoles are not activated. The transverse motion of the beam is controlled solely by the cavity focusing. The quadrupoles are included to provide additional operational flexibility. The injection energy is 10 MeV. The gradient of the cavities in the cryomodule is 7.75 MV/m. The linac provides a 30 MeV energy gain. The 40 MeV beam is transported through a 180^0 recirculation arc to the beam matching section which produces waists in the center of the wiggler with $\beta_{x,y} = 0.74$ m and $\alpha_{x,y} = 0$.

The injection conditions to the linac are as the following

$$\begin{aligned} \beta_{x,y} &= 5\,\mathrm{m} \\ \alpha_{x,y} &= 0 \end{aligned}$$

The following beam parameters are used in the simulation [30]

$$\begin{aligned} \sigma_z &= 0.5\,\mathrm{mm} \quad \text{or} \quad \sigma_t = 1.6\,\mathrm{ps} \\ \sigma_e &= 3 \times 10^{-2} \\ \epsilon_{norm} &= 1\pi\ \mathrm{cm \cdot mrad} \end{aligned}$$

The β functions and the emittances in the FEL linac are shown in Fig. 5-46. The emittance growth in the linac is about 60%. The emittance growth is mostly due to the skew coupling. The head-tail effects are small.

Beam dynamics for mismatched cases have been studied. For the cases of mismatches in β functions (Figs. 5-47 and 5-48), one can still get small β functions in the wiggler region. The emittance growth shows a small increment for smaller initial βs and a slight decrement for larger initial βs. For cases of mismatches in αs (Figs. 5-49 and 5-50), the perturbation on β functions is more noticeable. Emittance growth for the initially diverging beam is huge. Emittance growth for the initially converging beam is slightly larger than the nominal case. The most unfavorable mismatch condition is a divergent beam.

To reduce the 60% emittance growth in the linac, a skew quadrupole can be used to cancel the skew effects of the cavities. To have effective cancellation, the skew quadrupole should be placed at the entrance of the linac, where the beam energy is low and the β functions are large. The skew strength for a single cavity is

$$S_{cavity} = -4.04 \frac{\mathrm{G \cdot cm}}{\mathrm{cm}} \tag{5-126}$$

The skews add up in the eight cavities. The total skew strength of the linac is

$$S_{linac} = -32.32 \frac{\mathrm{G \cdot cm}}{\mathrm{cm}} \tag{5-127}$$

Since the $\beta_{x,y}$ functions in front of the linac are larger than the average $\beta_{x,y}$ functions in the linac, the skew quadrupole strength needed to correct the cavity skew effects will be slightly smaller than S_{linac}. For a 15 cm long quadrupole, numerical simulation shows that a strength of 1.857 G/cm is required. In Fig. 5-51 are shown the corrected results. The emittance growth is reduced to less than 10%.

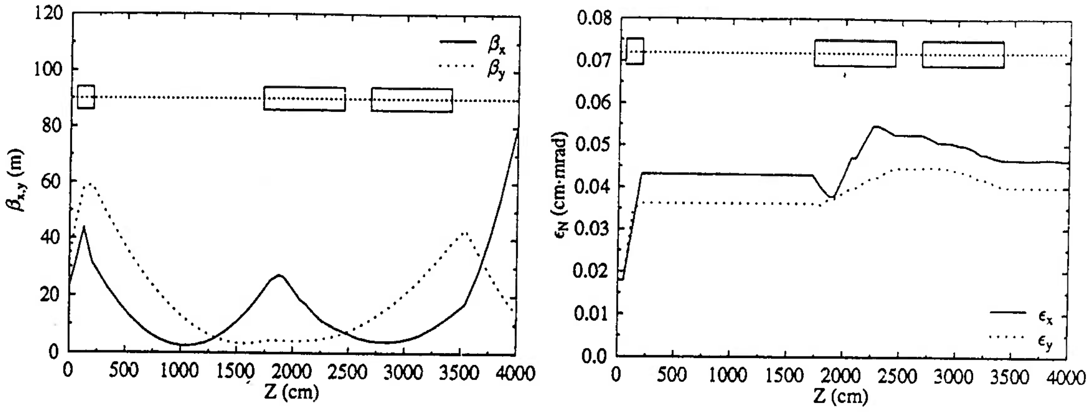

(a) (b)

Figure 5-28: Betatron functions in the injector. $\beta_{x,0}$ = 24.385 m, $\alpha_{x,0} = -7.659$, $\beta_{y,0}$ = 31.391 m, $\alpha_{y,0} = -12.152$, $\epsilon_{x,0} = \epsilon_{y,0}$=180 nm.

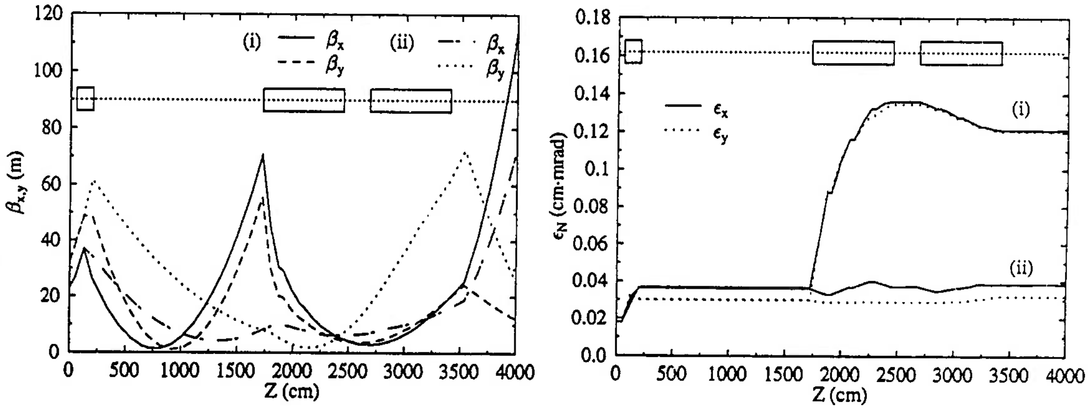

(a) (b)

Figure 5-29: Betatron functions with mismatched αs, $\alpha_{x,0} = -3.8$, $\alpha_{y,0} = -6.1$. (i) mismatched; (ii) after correction by adjusting the RF phase of the first cavity in the cryounit to 73.023^0.

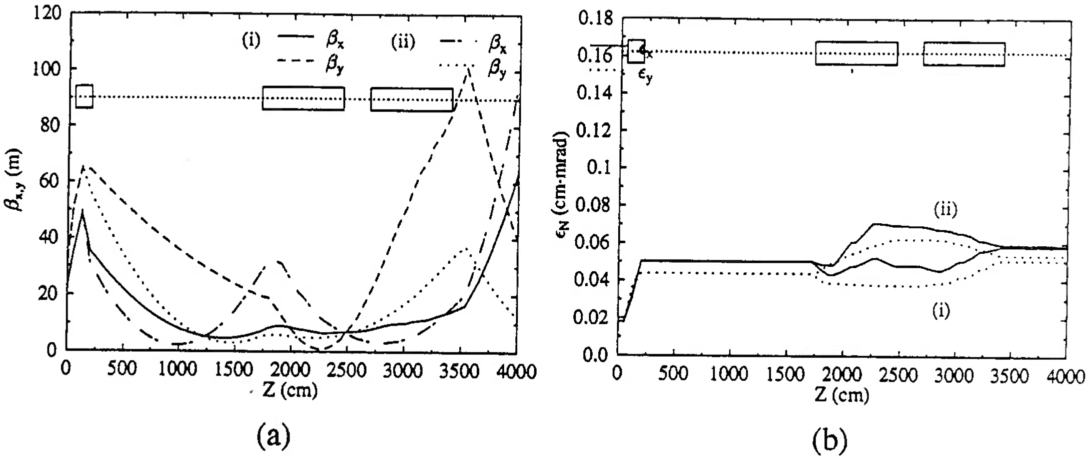

Figure 5-30: Betatron function with mismatched αs, $\alpha_{x,0} = -5.1$, $\alpha_{y,0} = -8.1$. (i) mismatched; (ii) after correction by adjusting the RF phase of the first cavity in the cryounit to 74.523^0.

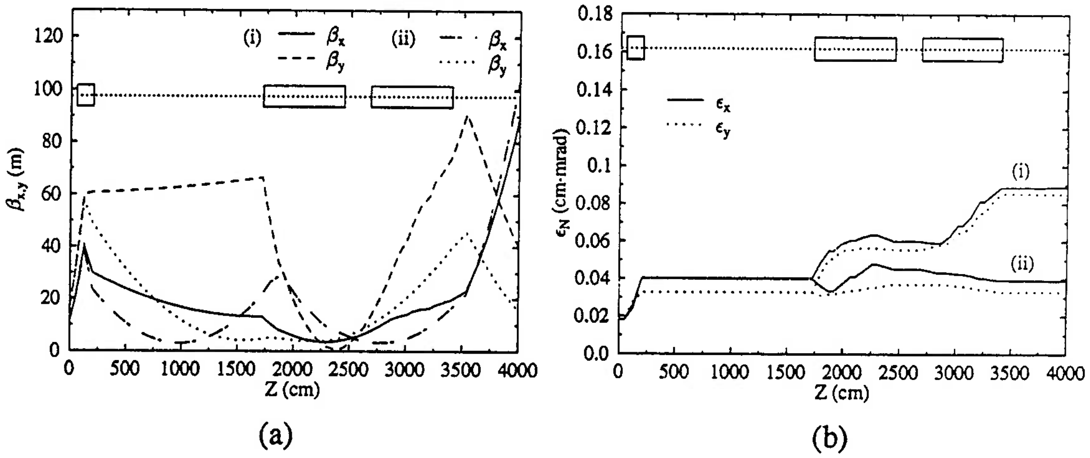

Figure 5-31: Betatron function with mismatched βs, $\beta_{x,0} = 12.385$, $\beta_{y,0} = 16.391$. (i) mismatched; (ii) after correction by adjusting the RF phase of the first cavity in the cryounit to 80.023^0.

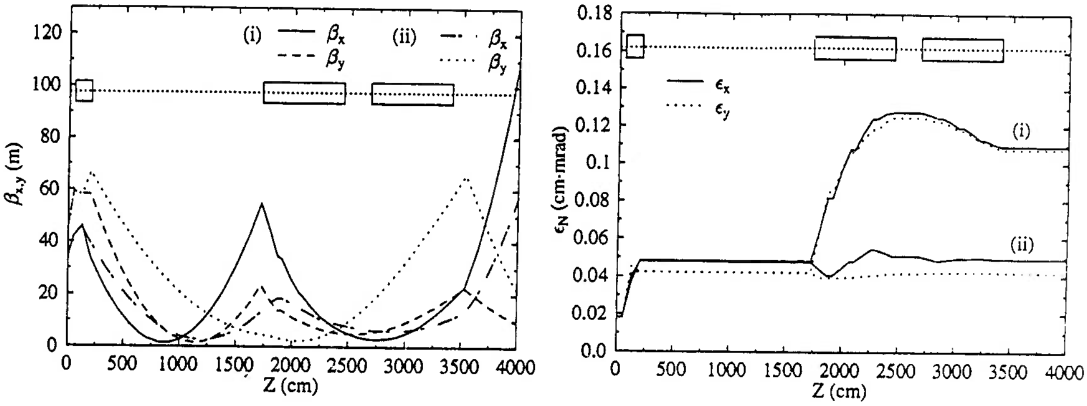

(a) (b)

Figure 5-32: Betatron functions with mismatched βs, $\beta_{x,0} = 36.385$, $\beta_{y,0} = 45.391$. (i) mismatched; (ii) after correction by adjusting the RF phase of the first cavity in the cryounit to 74.523^0.

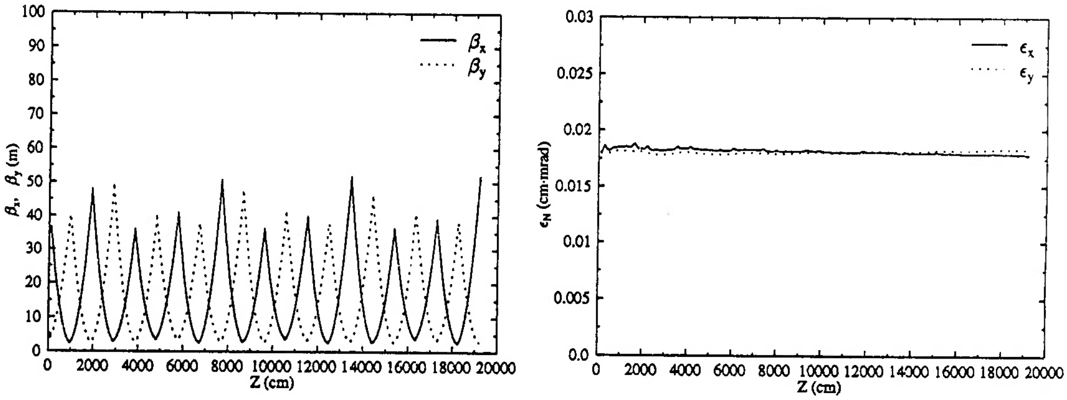

(a) (b)

Figure 5-33: Betatron functions in the first pass of the north linac. $\beta_{x,0}$=41.277 m; $\beta_{y,0}$=2.977 m. $\alpha_{x,0} = \alpha_{y,0}$ =0.0.

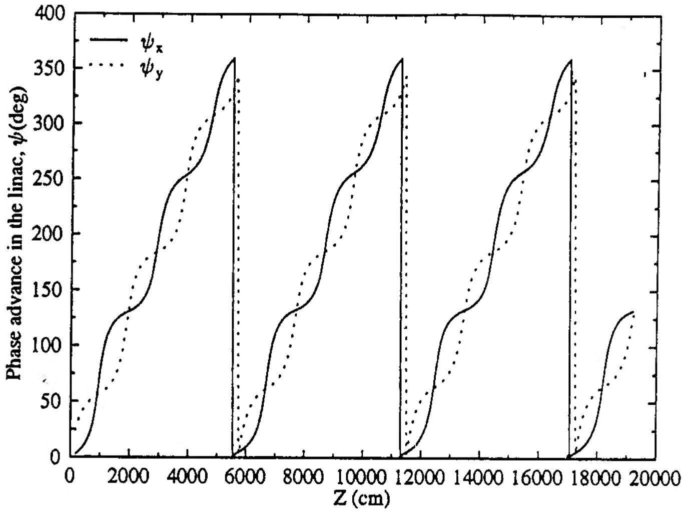

Figure 5-34: Phase advance in the first pass of the north linac, 120^0 per period (two cryomodules).

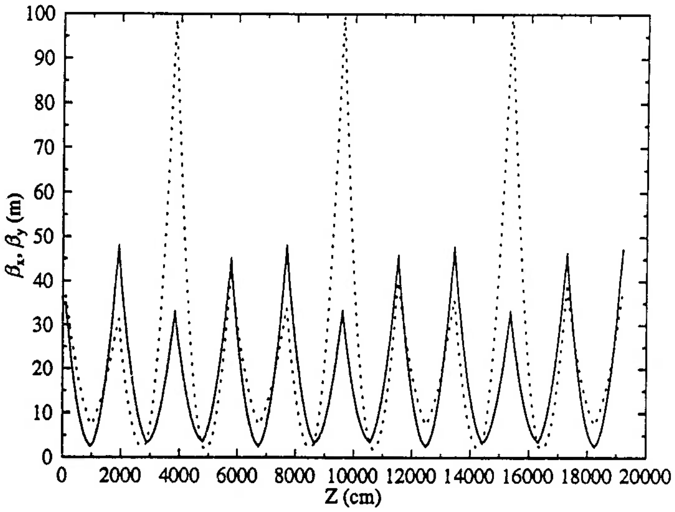

Figure 5-35: The β_x functions in the first pass of the north linac. $\beta_{x,0}$=41.277 m; $\beta_{y,0}$=2.977 m. $\alpha_{x,0} = \alpha_{y,0} = 0.0$. Dotted line: no cavity focusing, original quad strength; Solid line: no cavity focusing, the strength of the first quad increased by 30%.

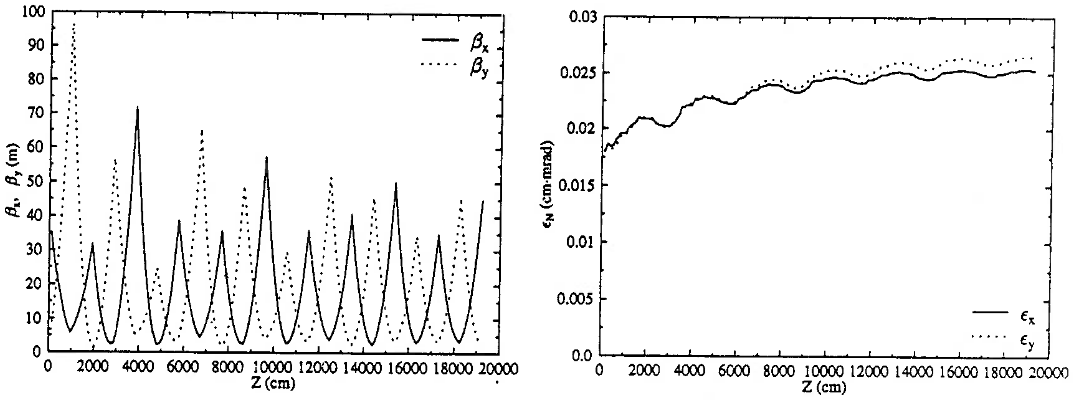

(a) (b)

Figure 5-36: Betatron functions in the first pass of the north linac with mismatched αs. $\alpha_{x,0} = \alpha_{y,0}$ =-1. The emittance grows by 40%.

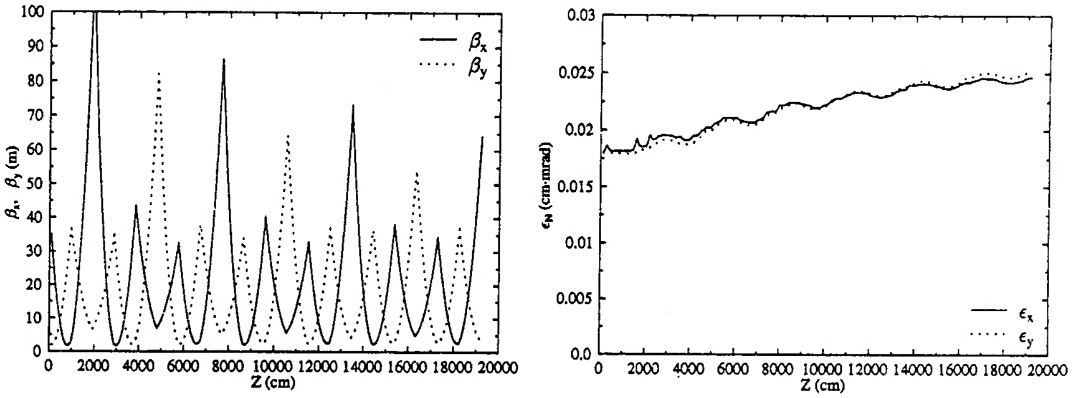

(a) (b)

Figure 5-37: Betatron functions in the first pass of the north linac with mismatched αs. $\alpha_{x,0} = \alpha_{y,0}$ =+1. The emittance grows by 39%.

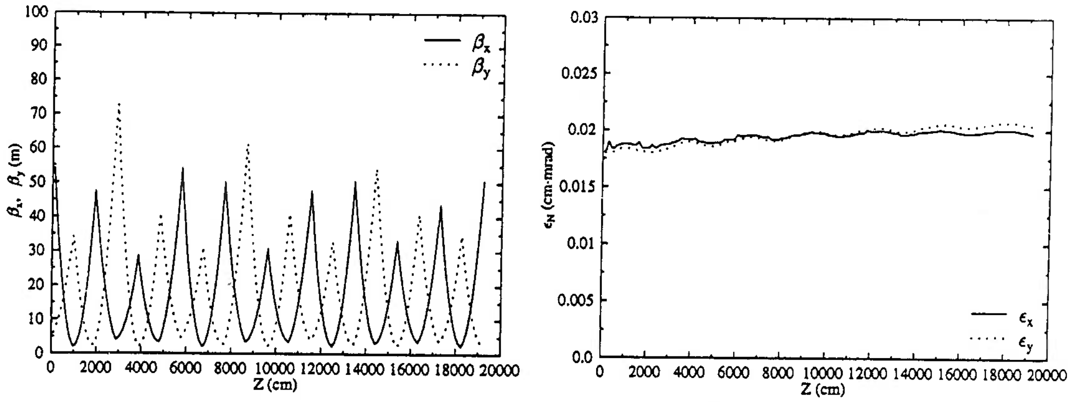

(a) (b)

Figure 5-38: Betatron functions in the first pass of the north linac with mismatched βs. $\beta_{x,0} = 80$ m, $\beta_{y,0} = 4$ m.

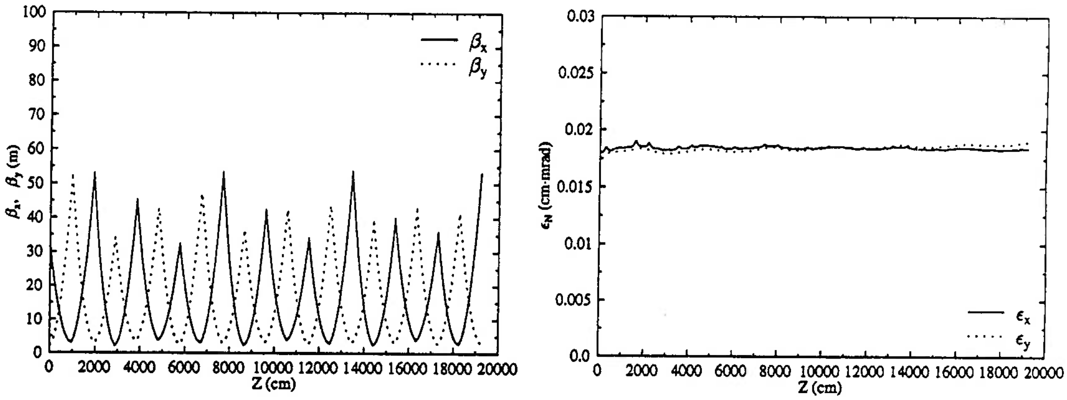

(a) (b)

Figure 5-39: Betatron functions in the first pass of the north linac with mismatched βs. $\beta_{x,0} = 30$ m, $\beta_{y,0} = 2$ m.

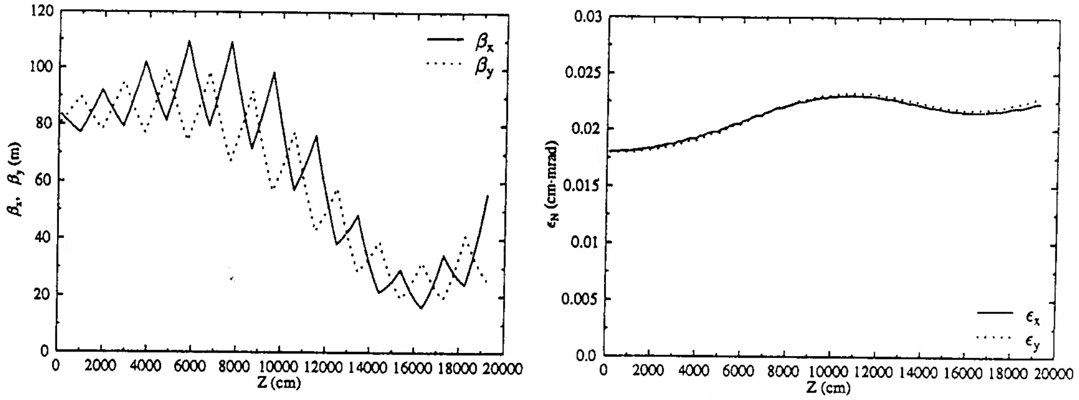

(a) (b)

Figure 5-40: Betatron functions in the second pass of the north linac with $\beta_{x,0} = \beta_{y,0} =$ 80 m, $\alpha_{x,0} = \alpha_{y,0} = 0$. The emittance grows by 25%.

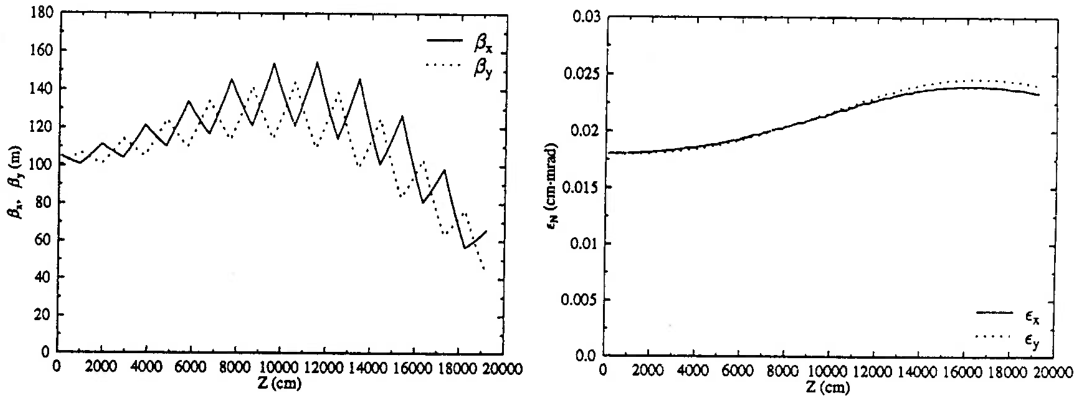

(a) (b)

Figure 5-41: Betatron functions in the third pass of the north linac with $\beta_{x,0} = \beta_{y,0} =$ 100 m, $\alpha_{x,0} = \alpha_{y,0} = 0$. The emittance grows by 30%.

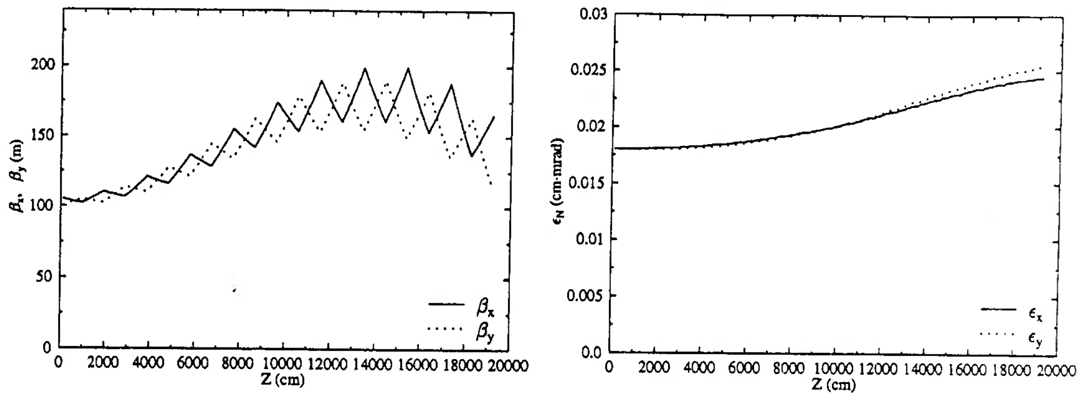

(a) (b)

Figure 5-42: Betatron functions in the fourth pass of the north linac with $\beta_{x,0} = \beta_{y,0} =$ 100 m, $\alpha_{x,0} = \alpha_{y,0} =0$. The emittances grow by 38%.

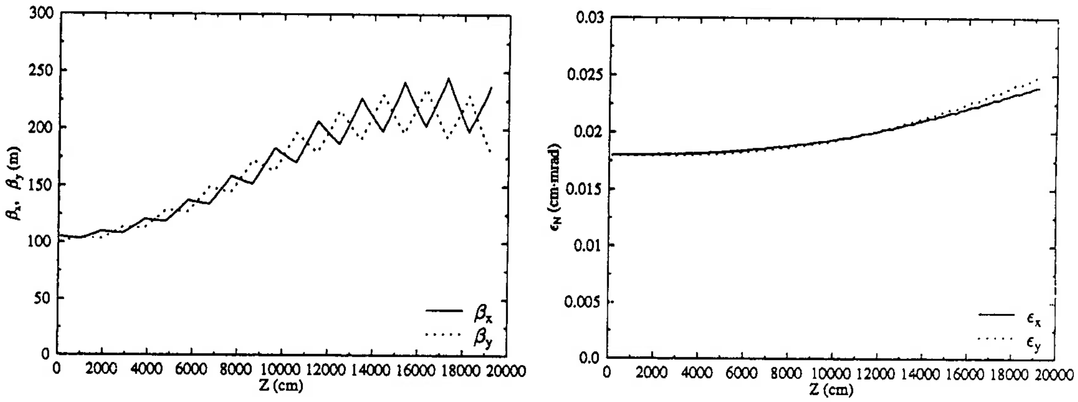

(a) (b)

Figure 5-43: Betatron functions in the fifth pass of the north linac with $\beta_{x,0} = \beta_{y,0} =$ 100 m, $\alpha_{x,0} = \alpha_{y,0} =0$. The emittance grows by 33%.

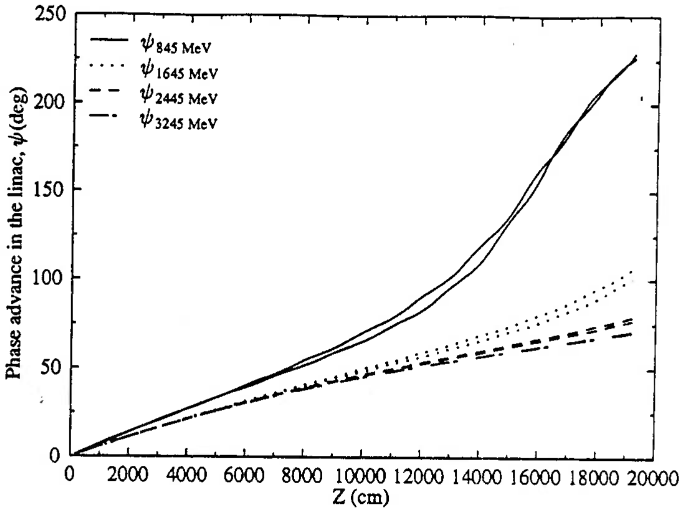

Figure 5-44: Phase advances in the higher passes of the north linac. $\psi = \int \frac{1}{\beta} ds$.

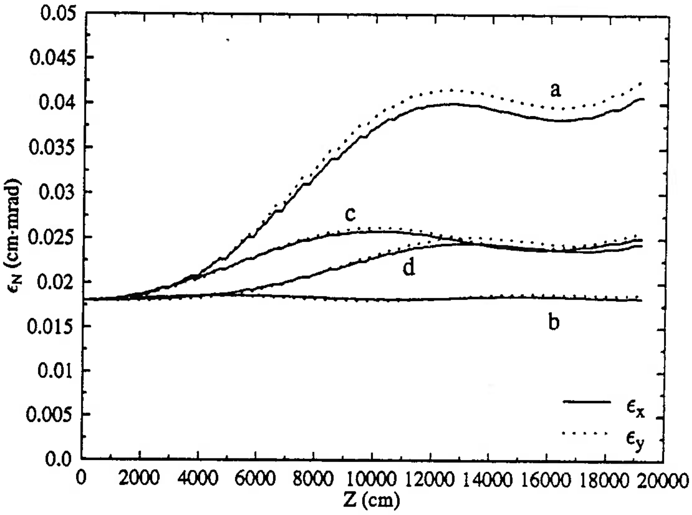

Figure 5-45: The normalized emittances of the second pass in the north linac with initially mismatched αs and βs. a) Mismatched αs, $\alpha_{x,0} = \alpha_{y,0} = -1$; b) Mismatched αs, $\alpha_{x,0} = \alpha_{y,0} = +1$. The $x - y$ coupling is strong for diverging beam. c) Mismatched βs, $\beta_{x,0} = \beta_{y,0} = 120$ m; d) Mismatched βs, $\beta_{x,0} = \beta_{y,0} = 40$ m. The $x - y$ coupling is less dependent on β mismatches.

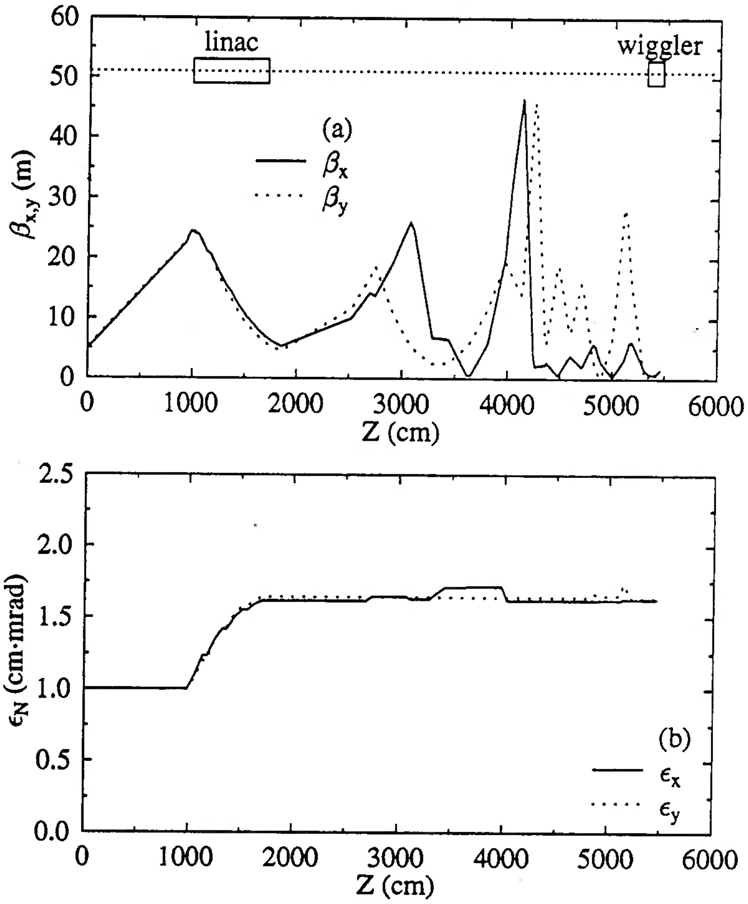

Figure 5-46: PARMELA simulation of the FEL linac. $\beta_{0,x,y} = 5$ m; $\alpha_{0,x,y} = 0$; Bunch length $\sigma_z = 0.5$ mm.

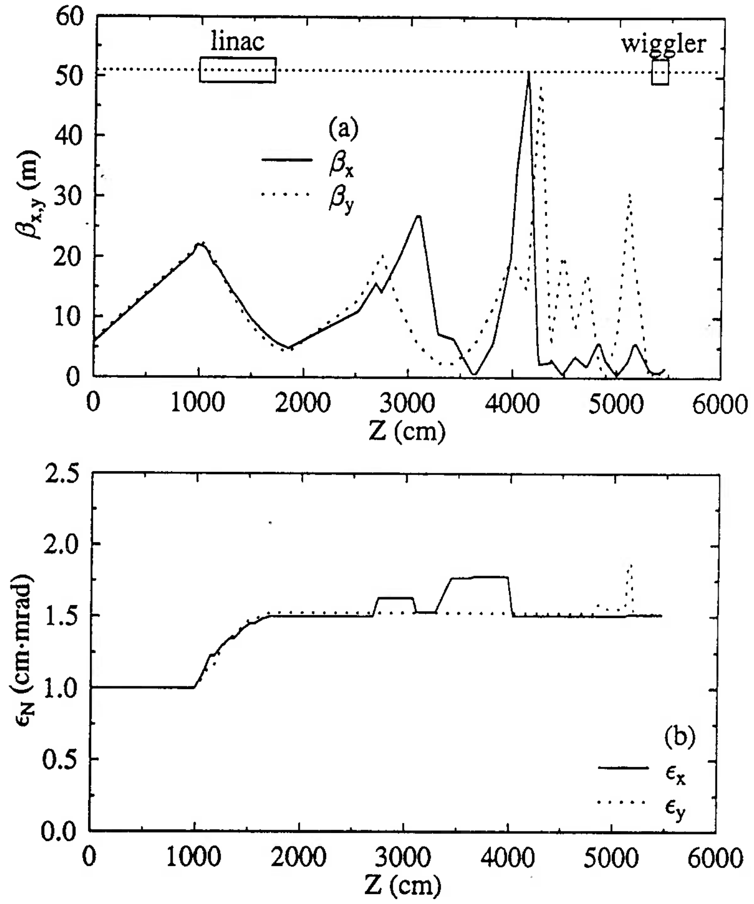

Figure 5-47: Betatron functions for mismatched β functions. $\beta_{0,x,y} = 6$ m; $\alpha_{0,x,y} = 0$; Bunch length $\sigma_z = 0.5$ mm.

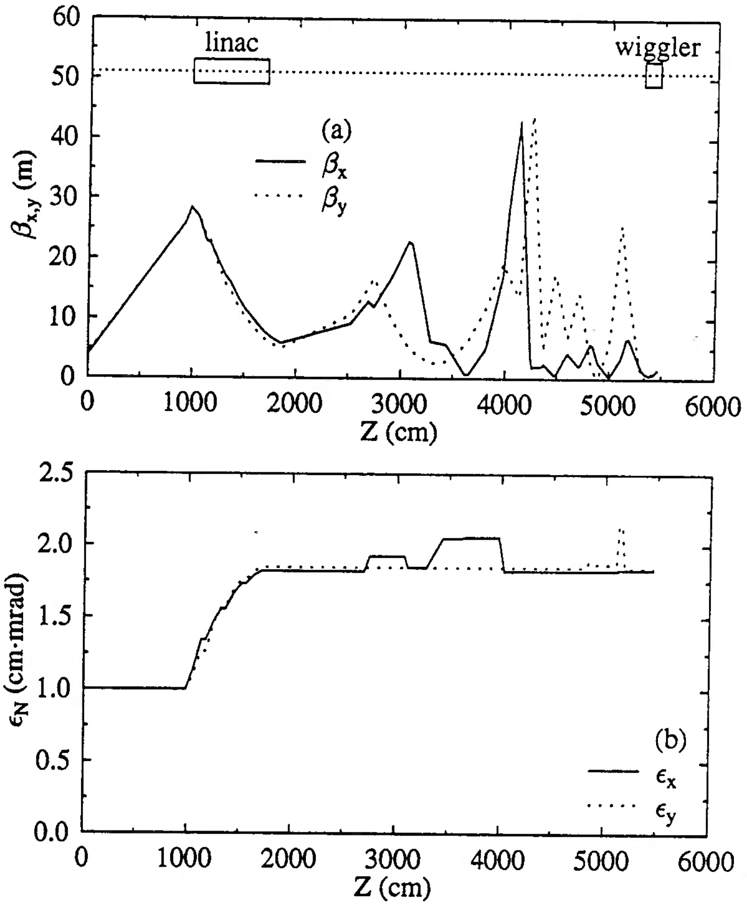

Figure 5-48: Betatron functions for mismatched β functions. $\beta_{0,x,y} = 4$ m; $\alpha_{0,x,y} = 0$; Bunch length $\sigma_z = 0.5$ mm.

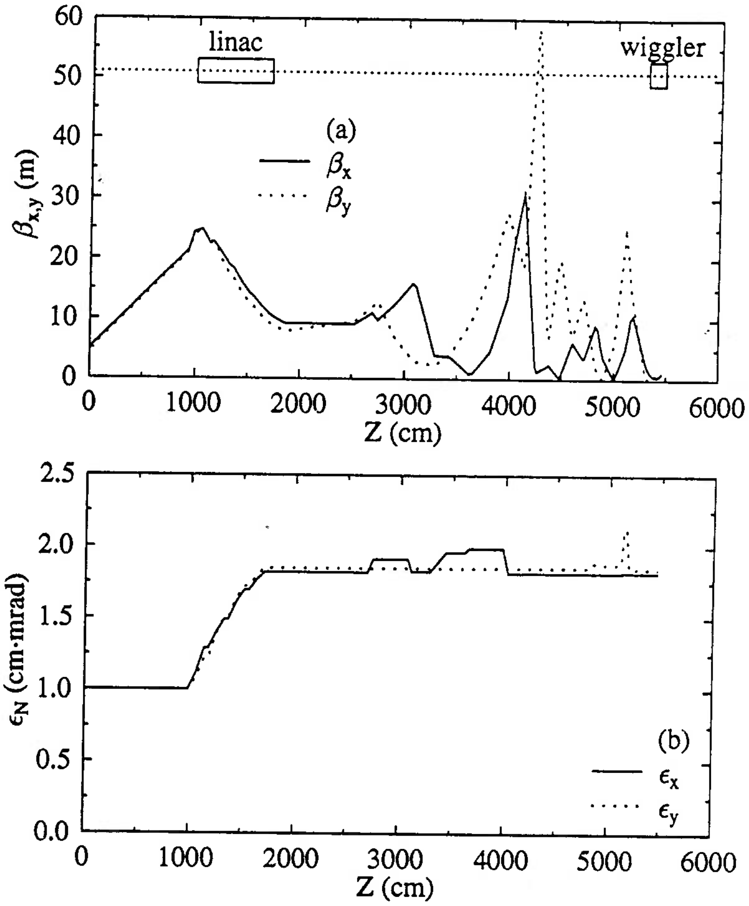

Figure 5-49: Betatron functions for mismatched αs. $\beta_{0,x,y} = 5$ m; $\alpha_{0,x,y} = +1$; Bunch length $\sigma_z = 0.5$ mm.

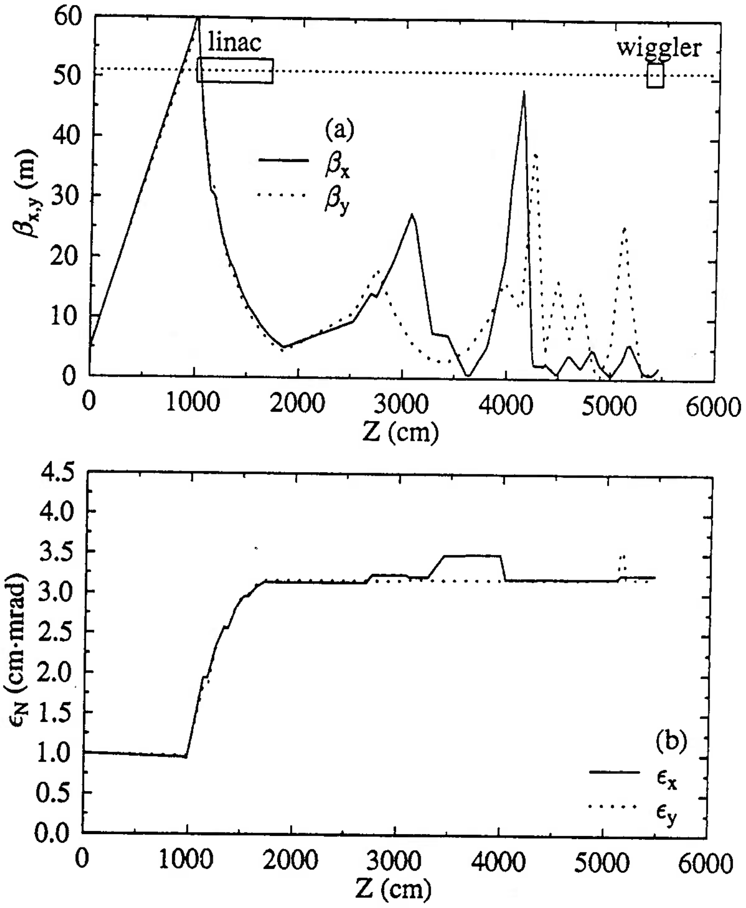

Figure 5-50: Betatron functions for mismatched αs. $\beta_{0,x,y} = 5$ m; $\alpha_{0,x,y} = -1$; Bunch length $\sigma_z = 0.5$ mm.

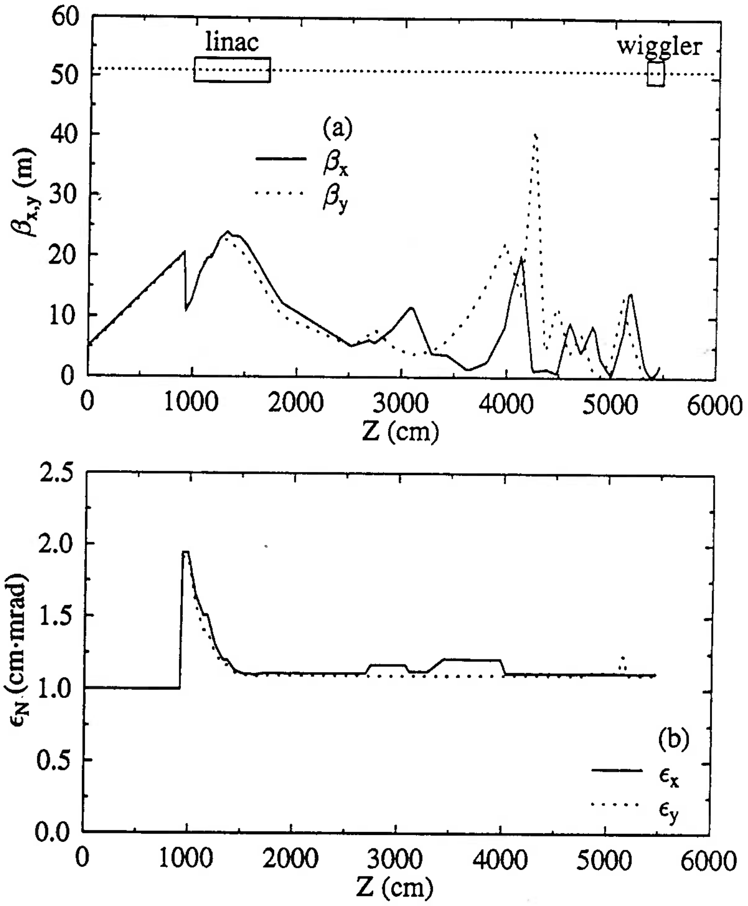

Figure 5-51: PARMELA simulation of the FEL linac. Skew quadrupole is used to correct the skew effects of the cavities. The emittance growth is reduced to 10%. Initial parameters: $\beta_{0,x,y} = 5$ m; $\alpha_{0,x,y} = 0$; Bunch length $\sigma_z = 0.5$ mm.

Chapter 6

Wakefield calculations for $v_t, v_s < c$

When a bunch of charged particles traverses a discontinuity in an accelerator, electromagnetic fields are excited. These fields are called wakefields, and are functions of space and time. The wakefields in turn interact with the particles and may cause instability, energy spread, emittance growth, etc. The wakefields can be considered a linear response of the system to an external excitation produced by the beam current. In general, the response can be expressed in terms of Green's functions. However, in most cases it is sufficient to consider the average effect of the accelerator structure: an energy loss and a transverse change in the momentum that a particle experiences when passing through the structure. Wake functions describe such average effects in an accelerator structure. They are functions of both the charge distribution in the bunch and the parameters of the beam environment.

Two kinds of wake functions are often mentioned in the literature, the longitudinal and the transverse. The longitudinal wake function w_l is defined as the energy loss ΔE_l of a test particle of charge e, that follows, at a distance s, a source particle of unit charge $q = 1$.

$$\Delta E_l = eqw_l(s) \qquad (6-128)$$

$$w_l(s, \mathbf{r}) = \frac{1}{qv} \int_{-\infty}^{+\infty} dz \mathbf{v} \cdot \mathbf{E}(\mathbf{r}, z, t) \left.\right|_{t=(z+s)/v} \qquad (6-129)$$

The transverse wake function is defined as the integrated transverse kick caused by the transverse component of the radiated field.

$$w_\perp(s, \mathbf{r}) = \frac{1}{q} \int_{-\infty}^{+\infty} dz \left(\mathbf{E} + \mathbf{v} \times \mathbf{B}\right)_\perp (z, \mathbf{r}, t) \left.\right|_{t=(z+s)/v} \qquad (6-130)$$

The Fourier transform of the wake function is called the impedance. The impedances corresponding to Eq. (6-129) and (6-130) are

$$\begin{aligned} Z_l(\omega, \mathbf{r}) &= \frac{1}{v}\int_{-\infty}^{+\infty} ds w_l(s, \mathbf{r}) e^{j\omega s/v} \\ &= \frac{1}{q}\int_{-\infty}^{+\infty} dz E_{z\omega}(z, \mathbf{r}) e^{-j\omega z/v} \end{aligned} \quad (6\text{-}131)$$

$$\begin{aligned} Z_\perp(\omega, \mathbf{r}) &= -\frac{j}{v}\int_{-\infty}^{+\infty} ds w_\perp(s, \mathbf{r}) e^{j\omega s/v} \\ &= -\frac{j}{q}\int_{-\infty}^{+\infty} dz \left(\mathbf{E}_\omega + \mathbf{v} \times \mathbf{B}_\omega\right)_\perp e^{-j\omega z/v} \end{aligned} \quad (6\text{-}132)$$

The wake functions and the impedances are the same quantities expressed in different domains. The wake function is the wakefield effect expressed in the time domain and the impedance is the wakefield effect expressed in the frequence domain. Either of them can be used to study beam-cavity interactions.

In the high frequency regime, which corresponds to short distance wake functions in the time domain, the impedance can be analytically calculated [31, 32, 33]. In analytical approaches, the problems addressed assume that both the velocities of the source particle v_s and the test particle v_t equal the velocity of light. By matching the fields at the beam pipe radius [31], an integral equation is obtained for the longitudinal electric component of the fields at the beam pipe radius. The kernel for the equation is approximated at high frequency. Under the causality condition, the integral equation becomes the Volterra equation of the first kind, which has the form

$$\int_0^x K(x-y) f(y) dy = g(x) \quad (6-133)$$

This can be solved analytically for some cases, and the solution for the coupling impedance can be found.

There are cases where the velocities of the source and test particles are not the speed of light. For the CEBAF FEL linac, the injection energy is 10 MeV, $\beta = v/c$=0.9987. Similarly, the injection energy to the first cryomodule of the CEBAF nuclear physics injector is 5 MeV, $\beta = v/c$=0.9948. In these cases the field propagates significantly faster than the charge, and the causality condition cannot be applied. The integral equation obtained from the field matching has the form of the Fredholm equation of the first kind

$$\int_a^b K(x,y)f(y)dy = g(x) \tag{6-134}$$

This kind of equation is ill conditioned. The solution is, in general, not unique.

To study the high frequency behavior of the impedance, efforts have been made to find a particular cavity that has simple kernels such that the integral equation can be solved analytically. So far, no answer had been found. Part of the reason is that the spectrum of the resonant frequency of a cavity has only a lower limit. No simple kernel can be found without making some approximation in evaluating the kernel.

In this chapter we will explore the properties of the wakefields for $(v_s,\ v_t) < c$. The Maxwell's equations are discretized and solved in the time domain. There are codes that are written for this purpose, such as TBCI [12] and ABCI [34], which are being widely used. These codes deal properly with the cases of $v_s = v_t = c$. An infinitely long beam pipe is simulated by applying a simple open boundary condition, which assumes that the phase velocity of the outgoing waves is c. TBCI has the option of $v_s = v_t < c$, but no open beam pipe is allowed in such a case. To address the problems of $v_s \neq v_t \neq c$, several issues need to be dealt with. At first, a proper open boundary condition should be used for $v < c$. The phase velocities of the propagating modes in the beam pipe are in general neither c nor the velocity of the particle. Even for one frequency, different modes have different longitudinal wave numbers. To accommodate the requirement of propagating the wakes of different phase velocities, we will apply the Lindman [40] boundary condition to the open beam pipe. The reflection coefficients at the open boundary can be reduced to less than 1% over a wide range of frequencies and incident angles. Secondly, the slippage between the source particle and the test particle should be included for the cases with $v_s \neq v_t$. Thirdly, since the integration for calculating the wake function can only be carried out at the beam pipe radius, the radial dependence must be found in order to calculate the wake functions at other radial positions. We will discuss the general scaling of the wake function for $v_s, v_t \leq c$ and the conditions for using the ultrarelativistic approximations. In the process of calculating the wakefields with very short bunches, we found that the Yee algorithm used in TBCI and ABCI is no longer appropriate. Unphysical results were obtained with the conventional choice of mesh/(bunch rms) ratio of 1/5. We found that the truncation error of the Yee algorithm is frequency dependent. A fourth-order FD-TD algorithm was developed to reduce the truncation error, and the program TBCI was modified for evaluating the wakefields of $v_s \neq v_t$ and of very short bunches.

6.1 Lindman boundary condition

Consider the two-dimensional wave equation in the (x, y) plane

$$\left(\frac{\partial^2}{\partial x^2} + \frac{\partial^2}{\partial y^2} - \frac{1}{c^2}\frac{\partial^2}{\partial t^2}\right) A = 0 \qquad (6-135)$$

The finite-difference form of Eq. (6-135) is

$$\left(\frac{\Delta_x^2}{D_x^2} + \frac{\Delta_y^2}{D_y^2} - \frac{\Delta_t^2}{c^2\tau^2}\right) A = 0 \qquad (6-136)$$

with forward-difference Δ defined as $\Delta_x A(x) = A(x + \Delta x) - A(x)$, D_x, D_y the mesh spacing and τ the time step. This difference equation has plane wave solutions of the form

$$A^i_{\ell,m} = Ae^{j(k_x \ell D_x + k_y m D_y - \omega i \tau)} \qquad (6-137)$$

at point (ℓ, m, i), where ω, k_x and k_y satisfy the dispersion relation

$$\sin^2(\frac{1}{2}\omega\tau) = \left(\frac{c\tau}{D_x}\right)^2 \sin^2(\frac{1}{2}k_x D_x) + \left(\frac{c\tau}{D_y}\right)^2 \sin^2(\frac{1}{2}k_y D_y) \qquad (6-138)$$

If this plane wave impinges on a fixed boundary at $x = x_0$, the additional function required to satisfy the boundary condition must have the same frequency ω and same wave number k_y along the boundary. Only waves with $k_x = -k_x$ can be used to satisfy the boundary condition.

We want to construct a boundary condition that is a linear operation and is satisfied by all outgoing waves with values of ω, k_x, and k_y consistent with the dispersion relation, such that the outgoing waves are absorbed. Consider the boundary condition

$$\Delta_t \Sigma_x A^i_{\ell,m} + \frac{Ic\tau}{D_x} G \Delta_x \Sigma_t A^i_{\ell,m} = 0 \tag{6 - 139}$$

where Σ is forward sum defined as $\Sigma_x A^i_{\ell,m} = A^i_{\ell,m} + A^i_{\ell+e,m}$. Consider $A^i_{\ell,m}$ to be a solution of the wave equation which consists of a left-going wave with amplitude L and a right-going wave with amplitude R

$$A^i_{\ell,m} = \left(Le^{-jk_x \ell D_x} + Re^{jk_x \ell D_x} \right) e^{j(k_y m D_y - \omega i \tau)} \tag{6 - 140}$$

Eq. (6-139) becomes

$$Le^{-jk_x(\ell+1/2)D_x} = \frac{IG - G_0}{IG + G_0} Re^{jk_x(\ell+1/2)D_x} \tag{6 - 141}$$

where $G_0 = \frac{D_x}{c\tau} \frac{\tan(\frac{1}{2}\omega\tau)}{\tan(\frac{1}{2}k_x D_x)}$. In the limit of τ, D_x, $D_y \to 0$, $G_0 = \omega / ck_x$. For a initially right-going wave, with the choice of $I = +1$ and $G = G_0$, the reflected left-going wave is zero, which is the case of the open boundary on the right-hand side beam pipe. Likewise with $I = -1$ and $G = G_0$, the reflected right-going wave of the left-going incident wave is zero, which is the case of the open boundary on the left-hand side.

From Eq. (6-138) and under the limit of τ, D_x, $D_y \to 0$

$$G_0 = \omega / ck_x = \left(1 - \frac{c^2 k_y^2}{\omega^2} \right)^{-1/2} \tag{6 - 142}$$

An approximation for G_0 in the time domain (which is stable in time) is

$$\hat{G}_0 = 1 + \sum_{n-1}^{N} \frac{\alpha_n (c\tau/D_y)^2 (\Delta_y^2/\Delta_t^2)}{1 - \beta_n (c\tau/D_y)^2 (\Delta_y^2/\Delta_t^2)} \tag{6 - 143}$$

where α_n and β_n are to be determined. Substituting Eq. (6-143) into Eq. (6-139), we have the following expression for the boundary condition

$$\begin{aligned}
\Delta_t \Sigma_x A^i_{\ell,m} + I\frac{c\tau}{D_x}\Delta_x \Sigma_t A^i_{\ell,m} &= -I\frac{c\tau}{D_x}\sum_{n=1}^{N} h^{i+1/2}_{n,m} & (6\text{-}144)\\
\left(\frac{\Delta_t^2}{c^2\tau^2} - \beta_n \frac{\Delta_y^2}{D_y^2}\right) h^{i+1/2}_{n,m} &= \alpha_n \frac{\Delta_y^2}{D_y^2}\Delta_x \Sigma_t A^i_{\ell,m} & (6\text{-}145)
\end{aligned}$$

If $h^i_{n,m} = 0$, the boundary conditions reduce to one-dimension boundary conditions, which are

$$\begin{aligned}
A^{i+1}_{\ell+1,m} &= A^i_{\ell,m} \quad \text{right} - \text{going wave} & (6\text{-}146)\\
A^{i+1}_{\ell,m} &= A^i_{\ell+1,m} \quad \text{left} - \text{going wave} & (6\text{-}147)
\end{aligned}$$

The $h^i_{n,m}$s are the correction functions to the one-dimensional boundary condition and are functions of the fields on the boundary at the previous time step. These quantities should be evaluated first. The difference equation (6-144) can then be solved to calculate the boundary values of the waves. The solutions for the difference equations (6-144) and (6-145) are as the follows:

1) Left-hand side boundary. (ℓ: the boundary mesh, $\ell+1$: the inner boundary mesh).

$$\begin{aligned}
A^{i+1}_{\ell,m} = {} & \frac{1}{1 - I\dfrac{c\tau}{D_x}}\Bigg(2A^i_{\ell,m} - (1 + I\frac{c\tau}{D_x})A^{i+1}_{\ell+1,m}\\
& + (1 - I\frac{c\tau}{D_x})(A^i_{\ell+1,m} - A^i_{\ell,m}) - 2Ic\tau\sum_{n=1}^{N} H^{i+1/2}_{n,m}\Bigg) \qquad (6\text{-}148)
\end{aligned}$$

where $I = -1$.

2) Right-hand side boundary. ($\ell+1$: the boundary mesh, ℓ: the inner boundary mesh).

$$\begin{aligned}
A^{i+1}_{\ell+1,m} = {} & \frac{1}{1 + I\dfrac{c\tau}{D_x}}\Bigg(2A^i_{\ell+1,m} - (1 - I\frac{c\tau}{D_x})A^{i+1}_{\ell,m}\\
& - (1 + I\frac{c\tau}{D_x})(A^i_{\ell+1,m} - A^i_{\ell,m}) - 2Ic\tau\sum_{n=1}^{N} H^{i+1/2}_{n,m}\Bigg) \qquad (6\text{-}149)
\end{aligned}$$

where $I = +1$. The $H_{n,m}$, defined as $h_{n,m}/2D_x$, has the same form for both left and right boundary conditions

$$\begin{aligned} H^{i+1/2}_{n,m} &= 2H^{i-1/2}_{n,m} - H^{i-3/2}_{n,m} + \frac{c^2\tau^2}{D_y^2}\Delta_y^2\Big(\beta_n H^{i-1/2}_{n,m} \\ &\quad + \frac{\alpha_n}{2D_x}(A^i_{\ell+1,m} + A^{i-1}_{\ell+1,m} - A^i_{\ell,m} - A^{i-1}_{\ell,m})\Big) \qquad (6\text{-}150) \end{aligned}$$

The optimized α_ns and β_ns up to $N = 3$ are

$$\begin{aligned} \alpha &= (0.3264,\ 0.1272,\ 0.0309) \\ \beta &= (0.7375,\ 0.98384,\ 0.9996472) \end{aligned}$$

The reflection coefficients with these α_ns and β_ns are less than 0.01 for a wide range of incident angles, which correspond to different wave numbers in the y direction, from 0^0 to 89^0.

Comparisons are made between the Lindman boundary condition and the one-dimension boundary condition used in the original TBCI. The fields are assumed propagating in a beam pipe of radius $a = 0.035$ m. The plane wave has the following form

$$A(r, z) = J_1(k_r r)e^{j(k_z z - 2\pi f t)} \qquad (6-151)$$

We have two test cases. The first case a) is for $f = 20$ GHz, $k_r a$ is the 4th zero of J_1, mesh size=0.1 mm, 3 time steps for one space mesh. The field is initiated on the inner boundary mesh and propagates outward. Fig. 6-52a presents the fields on the boundary after propagating 350 time steps. The second case b) is for $f = 50$ GHz; $k_r a$ is the 11th zero of J_1, and Fig. 6-52b shows the result after propagating 220 time steps. The Lindman boundary condition has much better accuracy than the one-dimensional boundary condition. The accuracy of the one-dimensional boundary is a function of the phase velocity and is time dependent. The Lindman condition has over all good accuracy.

6.2 Radial dependence of the wake function

Even though the particle-cavity interaction only happens within the cavity region, the fields generated with frequencies higher than the cutoff frequency will propagate in the beam pipe. The integral for calculating the wake function should be carried out from $-\infty$ to $+\infty$, which is not practical in numerical simulations. Since the fields satisfy the Maxwell' equations, the integral at different radial positions are related, and we can integrate the fields at the beam pipe radius where the fields are non-zero only within the open gap of the cavity. The integral thus only needs to be carried out in the gap region. The wake functions at other radii can be found by finding their radial dependence. The derivations of the functional dependence of the wake functions presented here assumes that the trajectories of the particles be straight lines.

The longitudinal component of the radiated **E** field satisfies the wave equation

$$(\nabla_\perp^2 - (\zeta_z^2 - k^2))E_z(r, \phi, z, t) = 0 \qquad (6-152)$$

The general expression of $E_z(r, \phi, z, t)$ in the cylindrical coordinate system is

$$E_z(r, \phi, z, t) = \sum_{m=-\infty}^{+\infty} \int_{-\infty}^{+\infty} d\omega d\zeta_z A(\zeta_z, \omega) G_m(k_r r) e^{-j\omega t + j\zeta_z z} e^{jm\phi} \qquad (6-153)$$

where

$$\begin{aligned} k &= \frac{\omega}{c} \\ k_r &= \sqrt{|\zeta_z^2 - k^2|} \\ G_m(k_r r) &= \begin{cases} I_m(k_r r), & \text{if} \quad \zeta_z^2 - k^2 \geq 0 \\ J_m(k_r r), & \text{if} \quad \zeta_z^2 - k^2 < 0 \end{cases} \end{aligned}$$

I_m and J_m are the modified Bessel function and the Bessel function of the first kind, respectively. The longitudinal wake function of the mth mode at (r, ϕ, $s = vt - z$) is

$$\begin{aligned} w_{l,m}(r, \phi, s) &= v \int_{-\infty}^{+\infty} dt d\omega d\zeta_z A(\zeta_z, \omega) G_m(k_r r) e^{-j\omega t + j\zeta_z z} e^{jm\phi}|_{t=(z+s)/v} \\ &= 2\pi \int_{-\infty}^{+\infty} d\omega A(\frac{\omega}{v}, \omega) I_m(k_r r) e^{-j\frac{\omega}{v}s} e^{jm\phi} \qquad (6\text{-}154) \end{aligned}$$

with

$$k_r = \sqrt{\frac{\omega^2}{v^2} - \frac{\omega^2}{c^2}} = \frac{\omega}{\gamma\beta c} \qquad (6-155)$$

At the pipe radius $r = a$

$$w_{l,m}(a, \phi, s) = 2\pi \int_{-\infty}^{+\infty} d\omega A(\frac{\omega}{v}, \omega) I_m(k_r a) e^{-j\frac{\omega}{v}s} e^{jm\phi} \qquad (6-156)$$

Fourier transforming Eq. (6-156), we have

$$A(\frac{\omega}{v}, \omega) e^{jm\phi} = \frac{1}{(2\pi)^2 v I_m(k_r a)} \int_{-\infty}^{+\infty} w_l(a, \phi, s') e^{j\frac{\omega}{v}s'} ds' \qquad (6-157)$$

Substituting Eq. (6-157) into Eq. (6-154) we have the wake function at radius r

$$w_{l,m}(r, \phi, s) = \frac{1}{2\pi v} \int_{-\infty}^{+\infty} ds' w_{l,m}(a, \phi, s') \int_{-\infty}^{+\infty} \frac{I_m(k_r r)}{I_m(k_r a)} e^{-j\frac{\omega}{v}(s-s')} d\omega \qquad (6-158)$$

It is clear now that the wake function at radius r is a weighted average of the wake function on the pipe radius. The weight function has finite width. In order to calculate the wake function at radius r up to a distance s, the wake integrated at the pipe radius should be some distance farther than s. The profile of the weight function which is defined as

$$\begin{aligned} W_{1,m}(\gamma, a, r, s - s') &= \frac{1}{2\pi v} \int_{-\infty}^{+\infty} \frac{I_m(k_r r)}{I_m(k_r a)} e^{-j\frac{\omega}{v}(s-s')} d\omega \\ &= \frac{\gamma}{2\pi a} \int_{-\infty}^{+\infty} \frac{I_m(q\frac{r}{a})}{I_m(q)} e^{-jq\frac{(s-s')}{a/\gamma}} dq \end{aligned} \qquad (6\text{-}159)$$

determines the effective region for the averaging. It is independent of the bunch length and is a function of r/a and a/γ only. The weight function for mode $m = 0$ for $\beta_t = 0.9948$, and $a = 1.74$ cm is shown in Fig. 6-53a, and the widths at half amplitude as functions of r/a and a/γ are shown in Fig. 6-53b. The weight function has Gaussian-like profile. The area under the curve is unity. The halfwidth for a given r/a is linear in a/γ. At the ultrarelativistic limit, $a/\gamma \to 0$, the weight function becomes $\delta(s - s')$, and the wake function for mode $m = 0$ is independent of radial position of the test particle.

From the Panofsky-Wenzel [41] theorem, the transverse wake function is related to the longitudinal one as follows

$$w_\perp(r,\phi,s) = -\frac{iv}{\omega}\nabla_\perp w_l(r,\phi,s) = -\int_{-\infty}^{s} \nabla_\perp w_l(r,\phi,z')dz' \qquad (6-160)$$

We have

$$w_{r,m}(r,\phi,s) = -\frac{m}{r}\int_{-\infty}^{s} dz' \int_{-\infty}^{+\infty} ds' w_{l,m}(a,\phi,s')W_{2,m}(\gamma,a,r,z'-s') \qquad (6\text{-}161)$$

$$w_{\phi,m}(r,\phi,s) = -j\frac{m}{r}\int_{-\infty}^{s} dz' \int_{-\infty}^{+\infty} ds' w_{l,m}(a,\phi,s')W_{1,m}(\gamma,a,r,z'-s') \qquad (6\text{-}162)$$

with

$$W_{2,m}(\gamma,a,r,z'-s') = \frac{\gamma}{2\pi a}\int_{-\infty}^{+\infty} dq \left(\frac{I_m(q\frac{r}{a})}{I_m(q)} + \frac{qr}{ma}\frac{I_{m+1}(q\frac{r}{a})}{I_m(q)}\right) e^{-jq\frac{(z'-s')}{a/\gamma}} \qquad (6-163)$$

At the ultrarelativistic limit, the Bessel functions in the weight functions are reduced to

$$\frac{I_m(q\frac{r}{a})}{I_m(q)} = \left(\frac{r}{a}\right)^m \qquad (6-164)$$

and the wake functions are

$$w_l(r,\phi,s) = \sum_{m=-\infty}^{+\infty} r^m u_{l,m}(a,s)\cos(m\phi) \qquad (6\text{-}165)$$

$$w_r(r,\phi,s) = -\sum_{m=-\infty}^{+\infty} m r^{m-1}\int_{-\infty}^{s} u_{l,m}(a,z')dz'\cos(m\phi) \qquad (6\text{-}166)$$

$$w_\phi(r,\phi,s) = \sum_{m=-\infty}^{+\infty} m r^{m-1}\int_{-\infty}^{s} u_{l,m}(a,z')dz'\sin(m\phi) \qquad (6\text{-}167)$$

where $u_{l,m}(a,s)$ is the amplitude of the longitudinal wake function integrated at the beam pipe radius and $u_{l,m}(a,s) = w_{l,m}(a,\phi,s)/a^m\cos(m\phi)$. At the ultrarelativistic limit, the longitudinal wake function is independent of r for $m = 0$ and scales as r^m for other modes whereas the transverse wake functions scale as r^{m-1}.

6.3 Numerical algorithm for solving Maxwell's equations in the time-domain

Numerical method uses typically finite-difference algorithm to solve the Maxwell's equations in the time-domain (FT-TD). In principle, it can deal with any complicated structure. The limitations of using this method are the computer memory and the CPU time. There are numerous computer codes that calculate wakefields. TBCI and ABCI are two codes that are widely used. The linear finite-difference algorithm is used in these codes. The linear algorithm, often referred as the Yee algorithm, was first proposed by Kane S. Yee in 1966 in 3-D Cartesian coordinates. It is the standard field solver of Maxwell's equations in the time-domain and has been widely used in numerical modeling of electromagnetic wave (microwave) interactions with arbitrary structures and beam-cavity interactions. The algorithm is reduced to $2\frac{1}{2}$ dimensions in TBCI and ABCI to deal with the problems in the cylindrically symmetric structures by projecting the fields to the r-z plane. The Yee algorithm discretizes both space and time into meshes. The continuous Maxwell's equations are replaced by finite-difference equations. The field distributions are represented by the field values assigned to the mesh points. The derivatives in the Maxwell's equations are replaced by the centered differences. Linear interpolation of the fields is used, and the algorithm has second order accuracy. The algorithm can usually give very good results by choosing appropriate mesh size and time step size. In the application of modeling microwave structures, good accuracy can be obtained by having the mesh size one tenth of λ_{min} [39]. In the application of wakefields calculations, good accuracy can be obtained by having the mesh size one fifth of σ, where σ is the rms bunch length of the driving particles, assuming a gaussian distribution. There are, however, instability problems due to the finite time-stepping in the iterative calculation of the fields. The stability of the time-stepping can be ensured by having the size of the time step satisfying the inequality

$$c\Delta t \leq \left(\frac{1}{\Delta x^2} + \frac{1}{\Delta y^2} + \frac{1}{\Delta z^2}\right)^{-1/2}$$

Problems arise when the fields have high frequency components. These were encountered in the wakefields evaluations of the CEBAF 5-cell cavities. The CEBAF beam has a very short bunch length. The spectrum of the current carried by the bunch contains very high frequency components. The wake functions calculated by use of TBCI and ABCI have unphysical oscillations even if the mesh size is one fifth of the rms bunch length.

It is found in this chapter that these unphysical oscillations are due to the accuracy of the Yee algorithm and are frequency-dependent. Even though the accuracy problem can be overcome by reducing the mesh size, the number of mesh points will increase so dramatically that it is not practical for large structures since the number of mesh points would be too large to be handled even by modern computers. In this chapter, we developed a fourth-order finite-difference formalism in a cylindrical coordinate system. These formulae have accuracy to the fourth order.

Before entering into the discussion of developing the fourth-order finite-difference formulae, let us first go through the Yee algorithm in a cylindrical coordinate system, and then discuss the problems encountered in calculating wake functions by using TBCI.

6.3.1 Yee algorithm in $2\frac{1}{2}$-D cylindrical coordinate system

The Yee FD-TD algorithm was developed in 1966 in a 3-D Cartesian coordinate system for solving scattering problems of microwaves by obstacles. In this section, we present the FD-TD formulae in a cylindrical coordinate system used in TBCI. These formulae are intended to calculate the fields excited by a driving current flowing parallel to the axis of the microwave structure, e.g. cavities. The formulae are equally good for wave propagation in cylindrically symmetric structures by replacing the driving current by driving boundary conditions. The fields are decomposed into multipoles in the cylindrical coordinate. For each (multipole) mode, the ϕ dependence of the fields is known ($\cos(m\phi)$ or $\sin(m\phi)$). Thus the fields are treated analytically in the ϕ coordinate. In the $r-z$ plane, the computation domain is discretized into meshes and the **E** and **H** fields are discretized and assigned to the meshes. The equations governing the relation of these fields are the Maxwell's equations

$$\begin{aligned}
\frac{\partial \mathbf{E}}{\partial t} &= \frac{1}{\epsilon_0}\nabla\times\mathbf{H} - \frac{\mathbf{J}}{\epsilon_0} && \text{(6-168)}\\
\frac{\partial \mathbf{H}}{\partial t} &= -\frac{1}{\mu_0}\nabla\times\mathbf{E} && \text{(6-169)}\\
\nabla\cdot\mathbf{E} &= \frac{\rho}{\epsilon_0} && \text{(6-170)}\\
\nabla\cdot\mathbf{H} &= 0 && \text{(6-171)}
\end{aligned}$$

Assuming the bunch of the charged particles has a line distribution $\lambda_s(s)$, where s is the distance from the center of the bunch, with velocity of βc moving in the z direction and off axis by a, the current density carried by the bunch can be expressed as

$$\mathbf{J}(r,\phi,z,t) = \frac{\beta c\lambda_s(z-\beta ct)}{\pi a}\sum_{-\infty}^{+\infty}\frac{1}{1+\delta_{0m}}\cos(m\phi)\delta(r-a)\mathbf{z}_0 \qquad (6-172)$$

where $\delta_{00}=1$ and $\delta_{0m}=0$ for $m\neq 0$. The electromagnetic fields excited by the mth component of the current have the following sinusoidal azimuthal dependence

$$\begin{aligned}
E_r(r,\phi,z,t) &= E_r^{(m)}(r,z,t)\cos(m\phi)\\
E_\phi(r,\phi,z,t) &= E_\phi^{(m)}(r,z,t)\sin(m\phi)\\
E_z(r,\phi,z,t) &= E_z^{(m)}(r,z,t)\cos(m\phi)\\
H_r(r,\phi,z,t) &= H_r^{(m)}(r,z,t)\sin(m\phi) && \text{(6-173)}\\
H_\phi(r,\phi,z,t) &= H_\phi^{(m)}(r,z,t)\cos(m\phi)\\
H_z(r,\phi,z,t) &= H_z^{(m)}(r,z,t)\sin(m\phi)
\end{aligned}$$

$E_r^{(m)}(r,z,t)$, $E_\phi^{(m)}(r,z,t)$, $E_z^{(m)}(r,z,t)$, $H_r^{(m)}(r,z,t)$, $H_\phi^{(m)}(r,z,t)$, and $H_z^{(m)}(r,z,t)$ are the magnitudes of the mth mode and are defined in the 2-dimensional $r-z$ plane and are separable from any other modes since the sinusoidal functions are orthogonal. The problem is then reduced to 2-dimensional and can be evaluated mode by mode. From now on the superscript m will be omitted and we will refer these 2-dimensional quantities as the fields. The full fields are obtained by multiplying the sinusoidal functions $\cos(\phi)$ or $\sin(\phi)$ to the 2-D fields.

The fields are discretized in the $r-z$ plane. The components of the fields are replaced by their nodal values assigned to the finite number of grid points as shown in Fig. 6-54, with J the total number of mesh points in the z direction. The arrangement of the E and H fields in Fig. 6-54 provides a natural geometry which fulfills the centered-difference analog to the space derivatives of the curl equations of the Maxwell's equations (6-168-6-171). The fields are also discretized in time t. The centered-difference analog to the time derivatives are obtained by evaluating the **H** fields a half time step ahead of the evaluation of the **E** fields. The centered-difference scheme has accuracy to the second order. This is demonstrated in the following. The E fields at time $(n \pm 1/2)\Delta t$ are expressed by the fields at $n\Delta t$ by use of the Taylor expansion

$$\begin{aligned} E^{n+1/2} &= E^n + \frac{\partial E^n}{\partial t}\left(\frac{\Delta t}{2}\right) + \frac{1}{2}\frac{\partial^2 E^n}{\partial^2 t}\left(\frac{\Delta t}{2}\right)^2 + O(\Delta t^3) && \text{(6-174)} \\ E^{n-1/2} &= E^n - \frac{\partial E^n}{\partial t}\left(\frac{\Delta t}{2}\right) + \frac{1}{2}\frac{\partial^2 E^n}{\partial^2 t}\left(\frac{\Delta t}{2}\right)^2 + O(\Delta t^3) && \text{(6-175)} \end{aligned}$$

Thus,

$$\frac{E^{n+1/2} - E^{n-1/2}}{\Delta t} = \frac{\partial E^n}{\partial t}\Delta t + O(\Delta t^2) \qquad (6-176)$$

and the truncation error is of the second order.

Let the **H** fields be evaluated at times $n\Delta t$ and the **E** fields at times $(n + 1/2)\Delta t$, n =1, 2, 3.... The solutions of the Maxwell's equations are

$$\begin{aligned} \mathbf{H}^{n+1} &= \mathbf{H}^n - \frac{\Delta t}{\mu_0}\nabla \times \mathbf{E}^{n+1/2} && \text{(6-177)} \\ \mathbf{E}^{n+3/2} &= \mathbf{E}^{n+1/2} + \frac{\Delta t}{\epsilon_0}\nabla \times \mathbf{H}^{n+1} - \frac{\Delta t}{\epsilon_0}\mathbf{J}^{n+1} && \text{(6-178)} \end{aligned}$$

Take the E_ϕ component at node k as an example.

$$\begin{aligned} E_{\phi,k}^{n+3/2} &= E_{\phi,k}^{n+1/2} + \frac{\Delta t}{\epsilon_0}\left(\frac{\partial H_r^{n+1}}{\partial z} - \frac{\partial H_z^{n+1}}{\partial r}\right)\Big|_{\text{at node } k} \\ &= E_{\phi,k}^{n+1/2} + \frac{\Delta t}{\epsilon_0 \Delta z}\left(H_{z,k-J}^{n+1} - H_{z,k}^{n+1} + H_{r,k}^{n+1} - H_{r,k-1}^{n+1}\right) && \text{(6-179)} \end{aligned}$$

Let $Z_0 = \sqrt{\mu_0/\epsilon_0} = \frac{1}{Y_0}$, $M = \frac{\Delta z}{v\Delta t}$ denotes the number of time steps for particles to proceed through one space step,

$$E^{n+3/2}_{\phi,k} = E^{n+1/2}_{\phi,k} + \frac{Z_0}{M\beta}\left(H^{n+1}_{z,k-J} - H^{n+1}_{z,k} + H^{n+1}_{r,k} - H^{n+1}_{r,k-1}\right) \qquad (6-180)$$

Similarly, the equations for other components of the **E** and **H** fields can be obtained. The following is a summary of the difference equations

$$\begin{aligned}
H^{n+1}_{r,k} &= H^{n}_{r,k} - \frac{Y_0}{M\beta}\left(E^{n+1/2}_{\phi,k} - E^{n+1/2}_{\phi,k+1} - \frac{m}{i-1}E^{n+1/2}_{z,k}\right) && (6\text{-}181)\\
H^{n+1}_{\phi,k} &= H^{n}_{\phi,k} - \frac{Y_0}{M\beta}\left(E^{n+1/2}_{z,k} - E^{n+1/2}_{z,k+J} + E^{n+1/2}_{r,k+1} - E^{n+1/2}_{r,k}\right) && (6\text{-}182)\\
H^{n+1}_{z,k} &= H^{n}_{z,k} - \frac{Y_0}{M\beta}\frac{2}{2i-1}\left(iE^{n+1/2}_{\phi,k+J} - (i-1)E^{n+1/2}_{\phi,k} + mE^{n+1/2}_{z,k}\right) && (6\text{-}183)\\
E^{n+3/2}_{r,k} &= E^{n+1/2}_{r,k} + \frac{Z_0}{M\beta}\left(H^{n+1}_{\phi,k-1} - H^{n+1}_{\phi,k} + \frac{2m}{2i-1}H^{n+1}_{z,k}\right) && (6\text{-}184)\\
E^{n+3/2}_{\phi,k} &= E^{n+1/2}_{\phi,k} + \frac{Z_0}{M\beta}\left(H^{n+1}_{z,k-J} - H^{n+1}_{z,k} + H^{n+1}_{r,k} - H^{n+1}_{r,k-1}\right) && (6\text{-}185)\\
E^{n+3/2}_{z,k} &= E^{n+1/2}_{z,k} + \frac{Z_0}{M\beta}\left(\frac{2i-1}{2i-2}H^{n+1}_{\phi,k} - \frac{2i-3}{2i-2}H^{n+1}_{\phi,k-J} - \frac{m}{i-1}H^{n+1}_{r,k}\right) && (6\text{-}186)
\end{aligned}$$

The current has only the z component. From Eq. (6-168), the source term needs to be added to Eq. (6-186) on the right hand side at the radial position of the bunch. The current density should be the averaged density in the mesh within which the field is defined.

a) Source on axis

If the current is on the axis, the current density is the total current divided by the area $\pi(\frac{\Delta R}{2})^2$. The source term for Eq. (6-186) is

$$-\frac{\Delta t}{\epsilon_0}\bar{J} = -\frac{4\lambda^{n+1}_{s,k}}{\epsilon_0 M\pi\Delta R} \qquad (6-187)$$

b) Source off axis

If the current if off axis, the current density is

$$\bar{J} = \frac{1}{\Delta R}\int_{a-\Delta R/2}^{a+\Delta R/2} J dr = \frac{\beta c\lambda_s(z-\beta ct)}{\Delta R^2(i-1)(1+\delta_{0m})} \qquad (6-188)$$

The source term for Eq. (6-186) is

$$-\frac{\Delta t}{\epsilon_0}\bar{J} = -\frac{\lambda_{s,k}^{n+1}}{\epsilon_0 M\pi(i-1)\Delta R(1+\delta_{0m})} \qquad (6-189)$$

where $\Delta R = \Delta z$.

In the applications of wakefield calculations, the fields are initially set to zero, $\mathbf{E}^{1/2} = 0$, $\mathbf{H}^0 = 0$, $\mathbf{J}^0 = 0$. The total electromagnetic fields can be calculated iteratively over these difference equations through the leapfrog process set forth by the centered-difference in the time axis.

6.3.2 Wakefield calculations with TBCI and ABCI

TBCI and ABCI are two computer codes being widely used in the accelerator community to calculate wakefields of various accelerator components as the charged particle traverses them. The Yee algorithm is employed in both codes to calculate the wakefields excited by the current. Usually, we are interested in the accumulated effects, called wake functions, that the fields act on a charge trailing the source particle by a distance s. The longitudinal and transverse wake functions are defined as

$$w_l(s,r) = \frac{1}{q}\int_{-\infty}^{\infty} dt\mathbf{v}\cdot\mathbf{E}(z,\mathbf{r},t)|_{z=vt-s} \qquad (6\text{-}190)$$

$$w_\perp(s,r) = \frac{1}{q}\int_{-\infty}^{\infty} dz\,(\mathbf{E}+\mathbf{v}\times\mathbf{B})\,|_{z=vt-s} \qquad (6\text{-}191)$$

where q is the charge of the source particles and r is the offset of the test particle. TBCI and ABCI give results as wake functions. These two codes can usually give good results. In this section, we will discuss some problems of the Yee algorithm in wakefield calculations. First, we'll present the problem we have had in calculating the wakefields of the CEBAF 5-cell cavity. Then, the behavior of the wakefields as functions of bunch and mesh parameters are studied for a simple pillbox cavity.

6.3.2.1 Problems in calculating wakefields of the CEBAF 5-cell cavity

The cross section of CEBAF 5-cell cavity is as shown in Fig. 6-55. The higher-order-mode coupler and the fundamental-power coupler can not be included since the bunch length of CEBAF beam is so small that the number of meshes used to discretize the 3-D structure would be so large that the problem cannot be handled even by large computers. The omission of these couplers retains the cylindrical symmetry of the structure so that TBCI can be used. The 5-cells of the cavity are close to elliptical with major axis about 9.4 cm and minor axis of about 5 cm (total width 10 cm). The two ends of the cavity are connected to 3.5 cm beam pipes. The 3.5 cm beam pipes are connected to 1.74 cm beam pipes and the 1.74 cm beam pipes are terminated at certain position where open boundary conditions are placed to simulate infinite long beam pipe conditions.

The mesh size should be much smaller than the rms bunch length σ so that the mesh would have good frequency resolution. The ratio of the rms bunch length and the mesh size is suggested in [36] to be at least of the order of five. The code can only handle uniform meshes, same mesh size in both r and z. In our calculation, the rms bunch length is 0.5 mm. The mesh size is 0.1 mm. The number of total mesh points is about 7.5 million. The number of time steps in one spatial mesh step is $MT = 3$, which is required by the numerical stability. The beam is on the axis. The wake is integrated at the beam pipe radius [36]. Fig. 6-56 shows the longitudinal wake function of mode $m = 0$. The dashed line is the charge distribution. The wake function obtained has strong oscillations. These oscillations are unphysical since the strength is stronger than the wake function in the bunch region. The same result is obtained with $M = 4$, which confirms that the problem is not due to the instability of the time stepping.

6.3.2.2 Wakefields for different bunch and cavity parameters

The wake function calculation of the CEBAF 5-cell cavity for short bunch beams have unphysical results. However, there are no such problems for longer bunches, for example millimeter or centimeter bunches. This suggests that the error is related to the bunch length or, in other words, the frequency of the fields. To have a better understanding of the problem, we studied the wakefields of a simple pillbox cavity. The pillbox cavity is shown in Fig. 6-57. We performed four test runs. The first two runs confirmed that the problem was due to the truncation error of the algorithm. The third run was to study the dependence of the errors on the bunch length for fixed cavity structure and σ/mesh ratio. The fourth run was to study the scaling of the errors with the frequency.

1. Wakefields for $\sigma = 0.5$ mm and σ/mesh =5

The cavity dimensions in this run are as follows: $r_a = 2$ cm, $r_b = 6$ cm, $r_c = 3$ cm, $L = 14$ cm and $d = 1$ cm. The bunch length $\sigma = 0.5$ mm. The mesh size is one fifth of σ. The number of time steps for one mesh step MT is 3. The result is shown in Fig. 6-58. Similar to the wake functions of the CEBAF cavity, oscillations are observed.

2. Wakefields for $\sigma = 0.5$ mm and σ/mesh =7.5

To verify that the oscillation in Fig. 6-58 is errors, the ratio σ/mesh is changed to 7.5 in this run. Other parameters stay the same. The result is shown in Fig. 6-59. The magnitude of oscillation in this run is reduced. Notice that for fixed structure and beam parameters, the error diminishes as the ratio σ/mesh increases while the frequency of the oscillation stays the same. This excludes the possibility that the error is contributed by a resonance between the grid frequency inherent in the finite-difference algorithm and the frequency excited by the bunch. The oscillation is cause by a numerical truncation error. One might expect that the truncation error is totally controlled by the small quantity $\Delta z/\lambda$. The next example shows that the truncation error depends on both the $\Delta z/\lambda$ and the frequency.

3. Wakefields for $\sigma = 2.5$ mm and σ/mesh=5

In this run, the cavity structure is the same as in the previous two runs. The bunch length is $\sigma = 2.5$ mm, and σ/mesh=5. The result is shown in Fig. 6-60. The wake function for a 2.5 mm bunch does not show any oscillation. The truncation error is small in this case.

For a gaussian bunch

$$\lambda(s) = \frac{1}{\sqrt{2\pi}\sigma} e^{-\frac{s^2}{2\sigma^2}} \qquad (6-192)$$

and the frequency spectrum has a gaussian profile

$$P(\omega) = \frac{1}{\sqrt{2\pi}} e^{-\frac{\omega^2\sigma^2}{2c^2}} \qquad (6-193)$$

The gaussian bunch excites wakefields with different strength for different frequencies. There is a rolloff frequency ω_R, for example the frequency which has a magnitude of 1 % in the spectrum, beyond which the excitation of the fields is negligible. The frequency ω_R is proportional to $1/\sigma$. If $\sigma/\Delta z$ is the same, say 5, for different bunch lengths (σs), frequencies with the same ω/ω_R for different σs will have the same $\Delta z/\lambda$ ratio. The truncation errors for these frequencies in these runs should be the same. But this is not the case as seen in the previous two examples. What makes the difference is that the frequency content in the wakefields in these runs are different. The frequency profile of a gaussian bunch tells us that a shorter bunch has more higher frequency components. The shorter the bunch, the higher the frequency contained in the spectrum. That the truncation error for the 0.5 mm bunch is larger than that for the 2.5 mm bunch suggests that the truncation error depends on frequency.

4. Scale everything in run 1 by 5

To check the frequency dependence of the truncation error, we scale the parameters in the first run by five. Now the cavity is five times bigger. The bunch is five times longer, $\sigma = 2.5$ mm. The ratio σ/mesh remains 5. The result is shown in Fig. 6-61. The wake function of this run has the same structure as the one shown in Fig. 6-58 except the scaling factor of five, the same factor as the cavity is scaled. This shows that the frequency dependence of the wake functions is linear. As we scale the cavity, the frequency of each mode is also scaled by the same factor. From mode analysis [37, 38], the wake function for resonant frequency ω_r is

$$W_r'(z) = \frac{R_s\omega_r}{Q}\cos(\frac{\omega_r z}{c}) \qquad (6-194)$$

where R_s and Q are the shunt impedance and the quality factor, respectively, and they depend only on the structure. The strength of the wake function for a given mode is proportional to its frequency. The same scaling factor is observed for the numerical error. The conclusion is that the numerical error has a linear frequency dependence.

6.3.3 Fourth-order FD-TD algorithm

We have seen that the truncation error imposes seriously problems in the calculation of wake functions of short bunches. In principle, the problem can be solved by use of fine meshes. But it is often impractical due to limitations in computer power. In this section, we will, extending J. Fang's work [42], derive a fourth-order FD-TD algorithm in the cylindrical symmetric coordinate system. The same Yee lattice is used to define the fields. Fourth-order accuracy is accomplished by including up to the third order derivatives of the fields in the Taylor expansion.

6.3.3.1 Fourth-order FD-TD algorithm in a cylindrical coordinate system

Expanding the **E** and the **H** fields to third order in time, we have

$$\begin{aligned} \mathbf{H}^{n+1} &= \mathbf{H}^n + \Delta t\frac{\partial \mathbf{H}^{n+1/2}}{\partial t} + \frac{\Delta t^3}{24}\frac{\partial^3 \mathbf{H}^{n+1/2}}{\partial t^3} + O(\Delta t^5) \qquad (6\text{-}195) \\ \mathbf{E}^{n+3/2} &= \mathbf{E}^{n+1/2} + \Delta t\frac{\partial \mathbf{E}^{n+1}}{\partial t} + \frac{\Delta t^3}{24}\frac{\partial^3 \mathbf{E}^{n+1}}{\partial t^3} + O(\Delta t^5) \qquad (6\text{-}196) \end{aligned}$$

Replacing the time derivatives in Eqs. (6-195,6-196) by the curl operators defined by the Maxwell's equations, we have

$$\mathbf{H}^{n+1} = \mathbf{H}^n - \frac{\Delta t}{\mu_0}\nabla\times\mathbf{E}^{n+1/2} - \frac{\Delta t^3 c^2}{24\mu_0}\nabla\times\nabla^2\mathbf{E}^{n+1/2}$$

$$
\begin{aligned}
&+\frac{\Delta t^3c^2}{24}\frac{\partial}{\partial t}(\nabla\times\mathbf{J}^{n+1/2})+O(\Delta t^5) && \text{(6-197)}\\
\mathbf{E}^{n+3/2} = {}& \mathbf{E}^{n+1/2}+\frac{\Delta t}{\epsilon_0}\nabla\times\mathbf{H}^{n+1}+\frac{\Delta t^3c^2}{24\epsilon_0}\nabla\times\nabla^2\mathbf{H}^{n+1}\\
&-\frac{\Delta t}{\epsilon_0}\mathbf{J}^{n+1}+\frac{\Delta t^3}{24\epsilon_0}\left(c^2\nabla\times\nabla\times\mathbf{J}^{n+1}-\frac{\partial^2\mathbf{J}^{n+1}}{\partial t^2}\right)+O(\Delta t^5) && \text{(6-198)}
\end{aligned}
$$

The first order derivatives involved in the curl operators are evaluated to the fourth-order finite-difference as

$$\frac{\partial H_{z,k+1/2}}{\partial z}=\frac{H_{z,k+1}-H_{z,k}}{\Delta z}-\frac{\Delta z^2}{24}\frac{\partial^3 H_{z,k+1/2}}{\partial z^3}+O(\Delta z^4) \qquad (6-199)$$

By using the above equations, the FD-TD formula to the fourth-order accuracy are obtained as the follows:

$$
\begin{aligned}
H_{r,k}^{n+1} = {}& H_{r,k}^{n}-\frac{Y_0}{M\beta}\left(E_{\phi,k}^{n+1/2}-E_{\phi,k+1}^{n+1/2}-\frac{m}{i-1}E_{z,k}^{n+1/2}\right)\\
&-\frac{\Delta z^3}{24}\frac{Y_0}{M\beta}\left(1-\frac{1}{(M\beta)^2}\right)\frac{\partial^3 E_\phi^{n+1/2}}{\partial z^3}\\
&+\frac{\Delta z^3 Y_0}{24(M\beta)^3}\left(\frac{m}{r^2}\frac{\partial}{dr}\left(r\frac{\partial E_z^{n+1/2}}{\partial r}\right)-\frac{m^3}{r^3}E_{z,k}^{n+1/2}+\frac{m}{r}\frac{\partial^2 E_z^{n+1/2}}{\partial z^2}\right.\\
&\left.+\frac{1}{r}\frac{\partial}{\partial z}\left(\frac{\partial}{\partial r}\left(r\frac{\partial E_\phi^{n+1/2}}{\partial r}\right)\right)+\frac{m^2}{r^2}\frac{\partial E_\phi^{n+1/2}}{\partial z}\right) && \text{(6-200)}\\
H_{\phi,k}^{n+1} = {}& H_{\phi,k}^{n}-\frac{Y_0}{M\beta}\left(E_{z,k}^{n+1/2}-E_{z,k+J}^{n+1/2}+E_{r,k+1}^{n+1/2}-E_{r,k}^{n+1/2}\right)\\
&-\frac{\Delta z^3}{24}\frac{Y_0}{M\beta}\left(\frac{\partial^3 E_z^{n+1/2}}{\partial r^3}-\left(1-\frac{1}{(M\beta)^2}\right)\frac{\partial^3 E_r^{n+1/2}}{\partial z^3}\right)\\
&-\frac{\Delta z^3 Y_0}{24(M\beta)^3}\left(\frac{1}{r}\frac{\partial^2}{\partial z\partial r}\left(r\frac{\partial E_r^{n+1/2}}{\partial r}\right)-\frac{m^2}{r^2}\frac{\partial E_r^{n+1/2}}{\partial z}\right.\\
&\left.-\frac{\partial}{\partial r}\left(\frac{1}{r}\frac{\partial}{\partial r}\left(r\frac{\partial E_z^{n+1/2}}{\partial r}\right)\right)+m^2\frac{\partial}{\partial r}\left(\frac{E_z^{n+1/2}}{r^2}\right)-\frac{\partial^3 E_z^{n+1/2}}{\partial r\partial z^2}\right) && \text{(6-201)}\\
H_{z,k}^{n+1} = {}& H_{z,k}^{n}-\frac{Y_0}{M\beta}\frac{2}{2i-1}\left(iE_{\phi,k+J}^{n+1/2}-(i-1)E_{\phi,k}^{n+1/2}+mE_{r,k}^{n+1/2}\right)\\
&+\frac{\Delta z^3}{24}\frac{Y_0}{M\beta}\frac{1}{r}\frac{\partial^3}{\partial r^3}\left(rE_\phi^{n+1/2}\right)\\
&-\frac{\Delta z^3 Y_0}{24(M\beta)^3}\left(\frac{1}{r}\frac{\partial^2}{\partial r^2}\left(r\frac{\partial E_\phi^{n+1/2}}{\partial r}\right)-\frac{m^2}{r}\frac{\partial}{\partial r}\left(\frac{E_\phi^{n+1/2}}{r}\right)\right.\\
&\left.+\frac{1}{r}\frac{\partial}{\partial r}\left(r\frac{\partial^2 E_\phi^{n+1/2}}{\partial z^2}\right)+\frac{m}{r^2}\frac{\partial}{\partial r}\left(r\frac{\partial E_r^{n+1/2}}{\partial r}\right)\right)
\end{aligned}
$$

$$
-\frac{m^3}{r^3}E_r^{n+1/2} + \frac{m}{r}\frac{\partial^2 E_r^{n+1/2}}{\partial z^2}\Bigg) \tag{6-202}
$$

$$
\begin{aligned}
E_{r,k}^{n+3/2} \quad = \quad & E_{r,k}^{n+1/2} + \frac{Z_0}{M\beta}\left(H_{\phi,k-1}^{n+1} - H_{\phi,k}^{n+1} + \frac{2m}{2i-1}H_{z,k}^{n+1}\right) \\
& + \frac{\Delta z^3}{24}\frac{Z_0}{M\beta}\left(1 - \frac{1}{(M\beta)^2}\right)\frac{\partial^3 H_\phi^{n+1}}{\partial z^3} \\
& + \frac{\Delta z^3 Z_0}{24(M\beta)^3}\Bigg(\frac{m}{r^2}\frac{\partial}{\partial r}\left(r\frac{\partial H_z^{n+1}}{\partial r}\right) - \frac{m^3}{r^3}H_z^{n+1} + \frac{m}{r}\frac{\partial^2 H_z^{n+1}}{\partial z^2} \\
& - \frac{1}{r}\frac{\partial^2}{\partial z \partial r}\left(r\frac{\partial H_\phi^{n+1}}{\partial r}\right) + \frac{m^2}{r^2}\frac{\partial H_\phi^{n+1}}{\partial z}\Bigg)
\end{aligned} \tag{6-203}
$$

$$
\begin{aligned}
E_{\phi,k}^{n+3/2} \quad = \quad & E_{\phi,k}^{n+1/2} + \frac{Z_0}{M\beta}\left(H_{z,k-J}^{n+1} - H_{z,k}^{n+1} + H_{r,k}^{n+1} - H_{r,k-1}^{n+1}\right) \\
& + \frac{\Delta z^3}{24}\frac{Z_0}{M\beta}\left(\frac{\partial^3 H_z^{n+1}}{\partial r^3} - \left(1 - \frac{1}{(M\beta)^2}\right)\frac{\partial^3 H_r^{n+1}}{\partial z^3}\right) \\
& + \frac{\Delta z^3 Z_0}{24(M\beta)^3}\Bigg(\frac{1}{r}\frac{\partial^2}{\partial z \partial r}\left(r\frac{\partial H_r^{n+1}}{\partial r}\right) - \frac{m^2}{r^2}\frac{\partial H_r^{n+1}}{\partial z} - \frac{\partial^3 H_z^{n+1}}{\partial r \partial z^2} \\
& - \frac{\partial}{\partial r}\left(\frac{1}{r}\frac{\partial}{\partial r}\left(r\frac{\partial H_z^{n+1}}{\partial r}\right)\right) + m^2\frac{\partial}{\partial r}\left(\frac{H_z^{n+1}}{r^2}\right)\Bigg)
\end{aligned} \tag{6-204}
$$

$$
\begin{aligned}
E_{z,k}^{n+3/2} \quad = \quad & E_{z,k}^{n+1/2} + \frac{Z_0}{M\beta}\left(\frac{2i-1}{2i-2}H_{\phi,k}^{n+1} - \frac{2i-3}{2i-2}H_{\phi,k-J}^{n+1} - \frac{m}{i-1}H_{r,k}^{n+1}\right) \\
& - \frac{\Delta z^3}{24}\frac{Z_0}{M\beta}\frac{1}{r}\frac{\partial^3}{\partial r^3}\left(rH_\phi^{n+1}\right) \\
& + \frac{\Delta z^3 Z_0}{24(M\beta)^3}\Bigg(\frac{1}{r}\frac{\partial^2}{\partial r^2}\left(r\frac{\partial H_\phi^{n+1}}{\partial r}\right) - \frac{m^2}{r}\frac{\partial}{\partial r}\left(\frac{H_\phi^{n+1}}{r}\right) \\
& + \frac{1}{r}\frac{\partial}{\partial r}\left(r\frac{\partial^2 H_\phi^{n+1}}{\partial z^2}\right) - \frac{m}{r^2}\frac{\partial}{\partial r}\left(r\frac{\partial H_r^{n+1}}{\partial r}\right) \\
& + \frac{m^3}{r^3}H_r^{n+1} - \frac{m}{r}\frac{\partial^2 H_r^{n+1}}{\partial z^2}\Bigg)
\end{aligned} \tag{6-205}
$$

The current term, Eq. (6-187) or Eq. (6-189), needs to be added to Eq. (6-215). The extra source terms for the higher-order corrections are

a) For the **E** field

$$
\begin{aligned}
\frac{\Delta t^3}{24\epsilon_0}\left(c^2\nabla \times \nabla \times \mathbf{J}^{n+1} - \frac{\partial^2 \mathbf{J}^{n+1}}{\partial t^2}\right) \quad = \quad & -\frac{\Delta z^2(z-\beta ct)}{24(M\beta\sigma)^2}\left(\frac{\Delta t}{\epsilon_0}\frac{\partial J^{n+1}}{\partial r}\right)\mathbf{r}_0 \\
& + \frac{m\Delta z^2(z-\beta ct)}{24r(M\beta\sigma)^2}\left(\frac{\Delta t}{\epsilon_0}J^{n+1}\right)\phi_0
\end{aligned}
$$

$$\begin{aligned}
&-\frac{\Delta z^2}{24(M\beta)^2}\left(\frac{\Delta t}{\epsilon_0}\frac{1}{r}\frac{\partial}{\partial r}(r\frac{\partial J^{n+1}}{\partial r})\right)\mathbf{z}_0 \qquad \text{(6-206)}\\
&+\frac{m^2\Delta z^2}{24r^2(M\beta)^2}\left(\frac{\Delta t}{\epsilon_0}J^{n+1}\right)\mathbf{z}_0\\
&+\frac{\Delta z^2}{24(M\sigma)^2}\left(1-\frac{(z-\beta ct)^2}{\sigma^2}\right)\left(\frac{\Delta t}{\epsilon_0}J^{n+1}\right)\mathbf{z}_0
\end{aligned}$$

b) For the **H** field

$$\begin{aligned}
\frac{\Delta t^3 c^2}{24}\frac{\partial}{\partial t}\left(\nabla\times\mathbf{J}^{n+1/2}\right) &= -\frac{m\epsilon_0\Delta z^2\beta c(z-\beta ct)}{24r(M\beta\sigma)^2}\left(\frac{\Delta t}{\epsilon_0}J^{n+1/2}\right)\mathbf{r}_0\\
&\quad -\frac{\epsilon_0\Delta z^2\beta c(z-\beta ct)}{24(M\beta\sigma)^2}\left(\frac{\Delta t}{\epsilon_0}\frac{\partial J^{n+1/2}}{\partial r}\right)\phi_0 \qquad \text{(6-207)}
\end{aligned}$$

where σ is the rms bunch length. $\frac{\Delta t}{\epsilon_0}J$ has the form of Eq. (6-187) or Eq. (6-189). The partial derivatives $\frac{\partial J}{\partial r}$ are defined half mesh off the radial position a. Since the average quantities are used in the difference equations, the partial derivatives have the following forms

$$\frac{\partial J}{\partial r}|_{r=a\pm\Delta R/2} = \mp\frac{\bar{J}}{\Delta R} \quad \text{with} \quad \bar{J} = \int_a^{a+\Delta R/2} J\delta(a-r)dr/\Delta R \qquad (6-208)$$

The second order derivative $\frac{1}{r}\frac{\partial}{\partial r}(r\frac{\partial J}{\partial r})$ is defined at $r=a$, and is

$$\frac{1}{r}\frac{\partial}{\partial r}\left(r\frac{\partial J}{\partial r}\right) = -2\frac{\bar{J}}{\Delta R^2} \qquad (6-209)$$

The higher-order derivatives in the fourth-order FD-TD equations should be evaluated at positions where the fields on the left hand side of the equations are defined. Replacing these derivatives by the finite-differences of the nodal field values, we have

$$\begin{aligned}
H_{r,k}^{n+1} &= H_{r,k}^{n} - \frac{Y_0}{M\beta}\left(E_{\phi,k}^{n+1/2} - E_{\phi,k+1}^{n+1/2} - \frac{m}{i-1}E_{z,k}^{n+1/2}\right)\\
&\quad -\frac{1}{24}\frac{Y_0}{M\beta}\left(1-\frac{1}{(M\beta)^2}\right)(E_{\phi,k+2}^{n+1/2} - 3E_{\phi,k+1}^{n+1/2} + 3E_{\phi,k}^{n+1/2} - E_{\phi,k-1}^{n+1/2})\\
&\quad +\frac{Y_0}{24(M\beta)^3}\left(\frac{2m}{(2i-2)^2}\left((2i-1)(E_{z,k+J}^{n+1/2} - E_{z,k}^{n+1/2})\right.\right.
\end{aligned}$$

$$
\begin{aligned}
& -(2i-3)(E_{z,k}^{n+1/2} - E_{z,k-J}^{n+1/2})\Big) - \frac{m^3}{(i-1)^3} E_{z,k}^{n+1/2} \\
& + \frac{m}{i-1}(E_{z,k+1}^{n+1/2} - 2E_{z,k}^{n+1/2} + E_{z,k-1}^{n+1/2}) \\
& + \Big(\frac{2i-1}{2i-2}(E_{\phi,k+1+J}^{n+1/2} - E_{\phi,k+J}^{n+1/2}) - 2(E_{\phi,k+1}^{n+1/2} - E_{\phi,k}^{n+1/2}) \\
& + \frac{2i-3}{2i-2}(E_{\phi,k+1-J}^{n+1/2} - E_{\phi,k-J}^{n+1/2})\Big) + \frac{m^2}{(i-1)^2}(E_{\phi,k+1}^{n+1/2} - E_{\phi,k}^{n+1/2})\Bigg) \qquad (6\text{-}210)
\end{aligned}
$$

$$
\begin{aligned}
H_{\phi,k}^{n+1} = {} & H_{\phi,k}^{n} - \frac{Y_0}{M\beta}\left(E_{z,k}^{n+1/2} - E_{z,k+J}^{n+1/2} + E_{r,k+1}^{n+1/2} - E_{r,k}^{n+1/2}\right) \\
& - \frac{1}{24}\frac{Y_0}{M\beta}\Bigg((E_{z,k+2J}^{n+1/2} - 3E_{z,k+J}^{n+1/2} + 3E_{z,k}^{n+1/2} - E_{z,k-J}^{n+1/2}) \\
& - \left(1 - \frac{1}{(M\beta)^2}\right)(E_{r,k+2}^{n+1/2} - 3E_{r,k+1}^{n+1/2} + 3E_{r,k}^{n+1/2} - E_{r,k-1}^{n+1/2})\Bigg) \\
& - \frac{Y_0}{24(M\beta)^3}\Bigg(\Big(\frac{2i}{2i-1}(E_{r,k+1+J}^{n+1/2} - E_{r,k+J}^{n+1/2}) - 2(E_{r,k+J}^{n+1/2} - E_{r,k}^{n+1/2}) \\
& + \frac{2i-2}{2i-1}(E_{r,k+1-J}^{n+1/2} - E_{r,k-J}^{n+1/2})\Big) - \frac{4m^2}{(2i-1)^2}(E_{r,k+1}^{n+1/2} - E_{r,k}^{n+1/2}) \\
& - \Big(\frac{2i+1}{2i}E_{z,k+2J}^{n+1/2} - \frac{6i-5}{2i-2}E_{z,k+J}^{n+1/2} + \frac{6i-1}{2i}E_{z,k}^{n+1/2} - \frac{2i-3}{2i-2}E_{z,k-J}^{n+1/2}\Big) \\
& + m^2\Big(\frac{E_{z,k+J}^{n+1/2}}{i^2} - \frac{E_{z,k}^{n+1/2}}{(i-1)^2}\Big) - \Big((E_{z,k+1+J}^{n+1/2} - E_{z,k+1}^{n+1/2}) \\
& - 2(E_{z,k+J}^{n+1/2} - E_{z,k}^{n+1/2}) + (E_{z,k-1+J}^{n+1/2} - E_{z,k-1}^{n+1/2})\Big)\Bigg) \qquad (6\text{-}211)
\end{aligned}
$$

$$
\begin{aligned}
H_{z,k}^{n+1} = {} & H_{z,k}^{n} - \frac{Y_0}{M\beta}\frac{2}{2i-1}\left(iE_{\phi,k+J}^{n+1/2} - (i-1)E_{\phi,k}^{n+1/2} + mE_{r,k}^{n+1/2}\right) \\
& + \frac{1}{24}\frac{Y_0}{M\beta}\Bigg(\frac{2i+2}{2i-1}E_{\phi,k+2J}^{n+1/2} - \frac{6i}{2i-1}E_{\phi,k+J}^{n+1/2} \\
& + \frac{6i-6}{2i-1}E_{\phi,k}^{n+1/2} - \frac{2i-4}{2i-1}E_{\phi,k-J}^{n+1/2}\Bigg) \\
& - \frac{Y_0}{24(M\beta)^3}\Bigg(\Big(\frac{2i+1}{2i-1}E_{\phi,k+2J}^{n+1/2} - \frac{6i-1}{2i-1}E_{\phi,k+J}^{n+1/2} \\
& + \frac{6i-5}{2i-1}E_{\phi,k}^{n+1/2} - \frac{2i-3}{2i-1}E_{\phi,k-J}^{n+1/2}\Big) - \frac{2m^2}{2i-1}\Big(\frac{E_{\phi,k+J}^{n+1/2}}{i} - \frac{E_{\phi,k}^{n+1/2}}{i-1}\Big) \\
& + \Big(\frac{2i}{2i-1}(E_{\phi,k+1+J}^{n+1/2} - 2E_{\phi,k+J}^{n+1/2} + E_{\phi,k-1+J}^{n+1/2}) \\
& - \frac{2i-2}{2i-1}(E_{\phi,k+1}^{n+1/2} - 2E_{\phi,k}^{n+1/2} + E_{\phi,k-1}^{n+1/2})\Big) \\
& + \frac{4m}{(2i-1)^2}\Big(i(E_{r,k+J}^{n+1/2} - E_{r,k}^{n+1/2}) - (i-1)(E_{r,k}^{n+1/2} - E_{r,k-J}^{n+1/2})\Big)
\end{aligned}
$$

$$-\frac{8m^3}{(2i-1)^3}E_{r,k}^{n+1/2}+\frac{2m}{2i-1}(E_{r,k+1}^{n+1/2}-2E_{r,k}^{n+1/2}+E_{r,k-1}^{n+1/2})\biggr)\tag{6-212}$$

$$\begin{aligned}
E_{r,k}^{n+3/2} \;=\;& E_{r,k}^{n+1/2}+\frac{Z_0}{M\beta}\left(H_{\phi,k-1}^{n+1}-H_{\phi,k}^{n+1}+\frac{2m}{2i-1}H_{z,k}^{n+1}\right)\\
&+\frac{1}{24}\frac{Z_0}{M\beta}\left(1-\frac{1}{(M\beta)^2}\right)(H_{\phi,k+1}^{n+1}-3H_{\phi,k}^{n+1}+3H_{\phi,k-1}^{n+1}-H_{\phi,k-2}^{n+1})\\
&+\frac{Z_0}{24(M\beta)^3}\biggl(\frac{4m}{(2i-1)^2}\Bigl(i(H_{z,k+J}^{n+1}-H_{z,k}^{n+1})-(i-1)(H_{z,k}^{n+1}-H_{z,k-J}^{n+1})\Bigr)\\
&-\frac{8m^3}{(2i-1)^3}H_{z,k}^{n+1}+\frac{2m}{2i-1}(H_{z,k+1}^{n+1}-2H_{z,k}^{n+1}+H_{z,k-1}^{n+1})\\
&-\Bigl(\frac{2i}{2i-1}(H_{\phi,k+J}^{n+1}-H_{\phi,k-1+J}^{n+1})-2(H_{\phi,k}^{n+1}-H_{\phi,k-1}^{n+1})\\
&+\frac{2i-2}{2i-1}(H_{\phi,k-J}^{n+1}-H_{\phi,k-1-J}^{n+1})\Bigr)+\frac{4m^2}{(2i-1)^2}(H_{\phi,k}^{n+1}-H_{\phi,k-1}^{n+1})\biggr)
\end{aligned}\tag{6-213}$$

$$\begin{aligned}
E_{\phi,k}^{n+3/2} \;=\;& E_{\phi,k}^{n+1/2}+\frac{Z_0}{M\beta}\left(H_{z,k-J}^{n+1}-H_{z,k}^{n+1}+H_{r,k}^{n+1}-H_{r,k-1}^{n+1}\right)\\
&+\frac{1}{24}\frac{Z_0}{M\beta}\biggl((H_{z,k+J}^{n+1}-3H_{z,k}^{n+1}+3H_{z,k-J}^{n+1}-H_{z,k-2J}^{n+1})\\
&-\left(1-\frac{1}{(M\beta)^2}\right)(H_{r,k+1}^{n+1}-3H_{r,k}^{n+1}+3H_{r,k-1}^{n+1}-H_{r,k-2}^{n+1})\biggr)\\
&+\frac{Z_0}{24(M\beta)^3}\biggl(\Bigl(\frac{2i-1}{2i-2}(H_{r,k+J}^{n+1}-H_{r,k-1+J}^{n+1})\\
&-2(H_{r,k}^{n+1}-H_{r,k-1}^{n+1})+\frac{2i-3}{2i-2}(H_{r,k-J}^{n+1}-H_{r,k-1-J}^{n+1})\Bigr)\\
&-\frac{m^2}{(i-1)^2}(H_{r,k}^{n+1}-H_{r,k-1}^{n+1})-\Bigl(H_{z,k+1}^{n+1}-H_{z,k+1-J}^{n+1}\\
&-2(H_{z,k}^{n+1}-H_{z,k-J}^{n+1})+H_{z,k-1}^{n+1}-H_{z,k-1-J}^{n+1}\Bigr)\\
&-\Bigl(\Bigl(\frac{2i}{2i-1}H_{z,k+J}^{n+1}-2H_{z,k}^{n+1}+\frac{2i-2}{2i-1}H_{z,k-J}^{n+1}\Bigr)\\
&-\Bigl(\frac{2i-2}{2i-3}H_{z,k}^{n+1}-2H_{z,k-J}^{n+1}+\frac{2i-4}{2i-3}H_{z,k-2J}^{n+1}\Bigr)\Bigr)\\
&+4m^2\Bigl(\frac{H_{z,k}^{n+1}}{(2i-1)^2}-\frac{H_{z,k-J}^{n+1}}{(2i-3)^2}\Bigr)\biggr)
\end{aligned}\tag{6-214}$$

$$\begin{aligned}
E_{z,k}^{n+3/2} \;=\;& E_{z,k}^{n+1/2}+\frac{Z_0}{M\beta}\left(\frac{2i-1}{2i-2}H_{\phi,k}^{n+1}-\frac{2i-3}{2i-2}H_{\phi,k-J}^{n+1}-\frac{m}{i-1}H_{r,k}^{n+1}\right)\\
&-\frac{1}{24}\frac{Z_0}{M\beta}\biggl(\frac{2i+1}{2i-2}H_{\phi,k+J}^{n+1}-\frac{6i-3}{2i-2}H_{\phi,k}^{n+1}\\
&+\frac{6i-9}{2i-2}H_{\phi,k-J}^{n+1}-\frac{2i-5}{2i-2}H_{\phi,k-2J}^{n+1}\biggr)
\end{aligned}$$

$$
\begin{aligned}
&+\frac{Z_0}{24(M\beta)^2}\Bigg(\Big(\frac{i}{i-1}H^{n+1}_{\phi,k+J}-\frac{3i-2}{i-1}H^{n+1}_{\phi,k}\\
&+\frac{3i-4}{i-1}H^{n+1}_{\phi,k-J}-\frac{i-2}{i-1}H^{n+1}_{\phi,k-2J}\Big)-2m^2\Big(\frac{H^{n+1}_{\phi,k}}{2i-1}-\frac{H^{n+1}_{\phi,k-J}}{2i-3}\Big)\\
&+\Big(\frac{2i-1}{2i-2}(H^{n+1}_{\phi,k+1}-2H^{n+1}_{\phi,k}+H^{n+1}_{\phi,k-1})\\
&-\frac{2i-3}{2i-2}(H^{n+1}_{\phi,k+1-J}-2H^{n+1}_{\phi,k-J}+H^{n+1}_{\phi,k-1-J})\Big)\\
&-\frac{m}{2}\Big(\frac{2i-1}{(i-1)^2}(H^{n+1}_{r,k+J}-H^{n+1}_{r,k})-\frac{2i-3}{(i-1)^2}(H^{n+1}_{r,k}-H^{n+1}_{r,k-J})\Big)\\
&+\frac{m^3}{(i-1)^3}H^{n+1}_{r,k}-\frac{m}{i-1}(H^{n+1}_{r,k+1}-2H^{n+1}_{r,k}+H^{n+1}_{r,k-1})\Bigg) \qquad (6\text{-}215)
\end{aligned}
$$

6.3.3.2 Frequency dependence of the higher-order terms

We anticipated in section 6.3.2 that the truncation error of the first order Yee algorithm is frequency dependent. This can be investigated by studying the higher-order terms derived in the previous section. For a given mode, assuming that the fields have $e^{-j\omega t}$ time dependence, the higher-order terms in Eqs. (6-197)-(6-198) have the following form

$$
\begin{aligned}
\Delta\left(\frac{\Delta \mathbf{H}}{\Delta t}\right) &= -\frac{\Delta z^2}{24\mu_0}\Big(\frac{\partial^3 E_\phi}{\partial z^3}\mathbf{r_0}-\Big(\frac{\partial^3 E_r}{\partial z^3}-(k_r^2+\frac{2}{r^2})\frac{\partial E_z}{\partial r}+\frac{k_r^2}{r}E_z\Big)\phi_0\\
&\quad-\Big((rk_r^2-\frac{1}{r})\frac{\partial E_\phi}{\partial r}+2k_r^2E_\phi\Big)\mathbf{z_0}\Big)-j\frac{\Delta t^2\omega^3}{24}\mathbf{H} \qquad (6\text{-}216)\\
\Delta\left(\frac{\Delta \mathbf{E}}{\Delta t}\right) &= \frac{\Delta z^2}{24\epsilon_0}\Big(\frac{\partial^3 H_\phi}{\partial z^3}\mathbf{r_0}-\Big(\frac{\partial^3 H_r}{\partial z^3}-(k_r^2+\frac{2}{r^2})\frac{\partial H_z}{\partial r}+\frac{k_r^2}{r}H_z\Big)\phi_0\\
&\quad-\Big((rk_r^2-\frac{1}{r})\frac{\partial H_\phi}{\partial r}+2k_r^2H_\phi\Big)\mathbf{z_0}\Big)-j\frac{\Delta t^2\omega^3}{24}\mathbf{E} \qquad (6\text{-}217)
\end{aligned}
$$

Except for the phase difference, the third order derivatives respect to z can be written as $k_z^3(E,H)$ and the first order derivative respect to r is approximately $k_r(E,H)$. These higher-order terms are, therefore, proportional to $\omega(k\Delta z)^2$, or, $\omega(\frac{\Delta z}{\lambda})^2$ (Δz and Δr are assumed equal). $(\Delta z/\lambda)^2$ is in general small and is usually used as a measure of the magnitude of the contributions from the terms related. The situation here now is different, the coefficients of $(\Delta z/\lambda)^2$ linearly increase with the frequency. If the frequency is very high, these terms may not be "small" any more.

In the first order Yee algorithm, these terms are the lowest order truncation errors and they are frequency dependent. Consider the case of the wakefields driven by a gaussian bunch, the profile of the frequency spectrum of such a bunch is also gaussian. Frequencies that have lower magnitudes in the spectrum excite wakefields with lower amplitudes. The wakefields excited by the frequencies higher than a certain frequency will be negligibly small. Assume this cutoff frequency is the frequency with a magnitude of 1% in the spectrum. The corresponding wave length of this frequency is $\lambda = 2\sigma$. Let the mesh size be one fifth of σ, that is $\Delta z/\lambda = 0.1$. This is the typical number suggested in [39] for numerical simulations of microwave propagation and in [36] for wakefield calculations. This number has been accepted as a general rule in the discretization of the Maxwell's equations so that the mesh would have enough frequency resolution. This rule works fine in the calculation of the wakefields of long bunches where the cutoff frequency of the excitation of the wakefields is low. Good accuracy can be obtained with the choice of $\Delta z = \sigma/5$. In the calculation of wakefields of short bunches, the fields contain higher frequency components. The quantity $\omega(\frac{\Delta z}{\lambda})^2$ may no longer be small even if $\Delta z = \sigma/5$ or $\Delta z/\lambda = 0.1$ is retained since it depends linearly on the frequency. The rule of $\Delta z = \sigma/5$ is no longer valid. This is what we have seen in the examples studied in section 6.3.2.2. Using a smaller mash size can improve the accuracy, but reducing the mesh size will increase the number of mesh points manyfold (for example 4-fold in the 2-D problem and 8-fold in the 3-D problems if the mesh size is halved). Computer memory becomes a problem.

The fourth-order FD-TD algorithm derived in this chapter can reduce the truncation error to the fourth order

$$\omega\left(\frac{\Delta z}{\lambda}\right)^4 \qquad (6-218)$$

Even though it is also linearly proportional to the frequency, the extra powers of $\Delta z/\lambda$

would greatly reduce the magnitude of the error. If the highest frequency of the excitation is not very high, the terms of the fourth order and higher of $\Delta z/\lambda$ are small.

6.3.3.3 Wakefields calculated by fourth-order FD-TD algorithm

The fourth-order FD-TD algorithm is implemented in TBCI. The results of the wake functions of a pillbox cavity and the CEBAF 5-cell cavity of a 0.5 mm bunch are shown in Fig. 6-62 and Fig. 6-63 by the solid lines. The dashed lines are the results of the second-order FD-TD algorithm. The same mesh size is used, which is $\sigma/\Delta z$=5. No oscillations are present in the calculations with the fourth-order FD-TD algorithm, and the errors are suppressed.

Higher-order truncation errors linearly depend on the frequency. They also accumulate with time. The longer the cavity the larger the accumulated error. The fourth-order FD-TD algorithm reduced these errors, and the accuracy is good for calculating the wakefields of sub-millimeter bunches. If the bunch is very short, the accuracy of the fourth-order algorithm presented in this chapter may not be good enough with $\sigma/\Delta z = 5$. A sixth-order algorithm or smaller mesh size should be used to obtain a good result. The fourth-order FD-TD algorithm typically takes more than six times the CPU time than the second-order Yee algorithm. In exchange, there is no extra computer memory required.

6.4 Wake functions for $v_s, v_t \neq c$

When the velocities of the source and the test particles are different, slippage occurs while the particles traversing the cavity. This effect should be included in the calculation of the wake functions which are the accumulated effects of the wakefields. In calculating the wake functions, we integrate the wakefields in the frame of the test particle. In the case of $v_t = v_s$, the mesh points for the wake function integration coincide with the mesh points used for the field calculations. The integral is performed by simply adding the fields at the mesh points at each time step. When $v_t \neq v_s$, where slippage exists between the particles, linear interpolation is used to evaluate the wakefields defined at the meshes in the frame of the test particle. The argument s in the wake function is defined as the initial position of the test particle relative to the source particle.

The wake functions for cases of $v_s, v_t \neq c$ are evaluated by use of the modified TBCI for the CEBAF 5-cell cavity. The rms bunch length is σ_z=3 mm. The mesh size is one fifth of σ_z. The wake functions are calculated at $r = 0$. We want to look at the wake functions for two different scenarios. The first scenario is $v_t = v_s < c$, which is the case of low energies. The second scenario is $v_t \neq v_s < c$, which is the case where multiple beams are accelerated in the same RF bucket.

Fig. 6-64 shows the wake functions for the cases of $v_t = v_s$. The values $\beta = 0.9948$ and $\beta = 0.9987$ correspond to beam energies of 5 MeV and 10 MeV respectively. The wake functions integrated at the pipe radius which is 1.74 cm are quite close to the wake function for $\beta = 1$. The wake functions on the axis calculated by applying the average weighting have a little difference from the $\beta = 1$ case. For these bunch length and energies, the effect of $v < c$ is small.

For the cases of $v_s \neq v_t$, as shown in Fig. 6-65, not only are amplitudes of the wake functions different, the slippage between the source and the test particles also results in displacement in the wake distribution. The value $\beta = 0.99$ corresponds to an electron energy of 3.6 MeV. What happens when $v_t = 0.99c < v_s = c$ is that the source particle and the wakefields propagate faster than the test particle. The test particle initially placed ahead of the source particles is caught by the fields generated by the source particle. So the wake function is displaced to the head side of the source bunch. For $v_t = c > v_s$, the test particle behind the source particle catches up with the source particle and a maximal wake force is accumulated. The wake function displaces to the tail side of the source bunch. For $\beta = 0.999$ which corresponds to $E = 11.5$ MeV, the wake functions are close to that for $\beta = 1$.

6.5 The smearing effects for $v < c$

The width of the short range wake function is roughly proportional to the bunch length, while the width of the weight function depends only on the energy and the cavity structure. Thus the smearing effect is bunch length dependent. If the width of the weight function is much smaller than the bunch length, the smearing effect will be small, and *vice versa.* Fig. 6-64 shows an example of long bunches, where the smearing effect is negligible. Fig. 6-66*a* shows the radial dependence of the wake functions of a pillbox cavity (3 cm × 4 cm, pipe radius=1 cm) for a short bunch with bunch length of 0.5 mm (rms) and $\beta_s = \beta_t = 0.9948$. The sharp peak of the wake function on the pipe radius is flattened by the weight function at $r < a$. The wake functions also show the slippage effects between the charge and the fields, which results in none zero wakefields ahead of the bunch. Numerical verification of this effect is obtained by integrating the wake at $r = 0.75$ cm for a long distance. Fig. 6-66*b* shows the results with integration limits of 6 cm and 25 cm. The later one gives a closer result to the wake function calculated by use of the weight function. For $\beta < 1$, the slippage between the particle and the fields results in finite wake in front of the bunch.

The effective range of the weight function for $r = 0$, wake function on axis, is proportional to the ratio of $\frac{a}{\gamma}$. The short range wake function has a peak which has a width that is proportional to the bunch length of the beam. The smearing effect of the short range wake function for a given energy then depends not only on the energy (γ) of the beam, but also on the bunch length. The ratio

$$R = \frac{\sigma_z \gamma}{a} \qquad (6-219)$$

is a measure of the smearing effect. Large R implies weak smearing. The relative difference of the peaks of the short range wake functions calculated at the pipe radius and on the axis of a pillbox cavity as a function of R is shown in Fig. 6-67. For $R = 1.5$, the relative difference is less than 10%.

The R value of Eq.(6-219) can be used to determine whether the beam can be treated as ultrarelativistic in the wakefield calculation. The difference of the wake functions as a function of R may be slightly different for different structures and bunch length. It is shown from the numerical simulations that the difference of the peak less than 10% can in general be obtained for $R > 1.5$. For cases with $R > 1.5$, the beam can be assumed ultrarelativistic. For $R < 1.5$, smearing effect is significant, wake functions at $r < a$ should be calculated by use of the weighted average.

The radius of the beam pipe of the CEBAF cavity is $a = 1.74$ cm. For σ_z=3 mm, the beam can be treated as being ultrarelativistic for $\gamma > 8.7$ or $E > 4.5$ MeV. While for $\sigma_z = 0.5$ mm, the beam can be treated as being ultrarelativistic for $\gamma > 52$ or $E > 26.5$ MeV.

To conclude, the algorithm developed in this chapter can be used to calculate wakefields of beams with $\beta < 1$ as long as the trajectory of the beam is approximately a straight line. The effects of slippage between the beams and between the beam and the fields are important in the cases of low energies and short bunches. The R value defined in Eq. (6-219) is a measure of the smearing effect on the wakefields of non-relativistic beam. The particle can only be assumed ultrarelativitic for cases with large R.

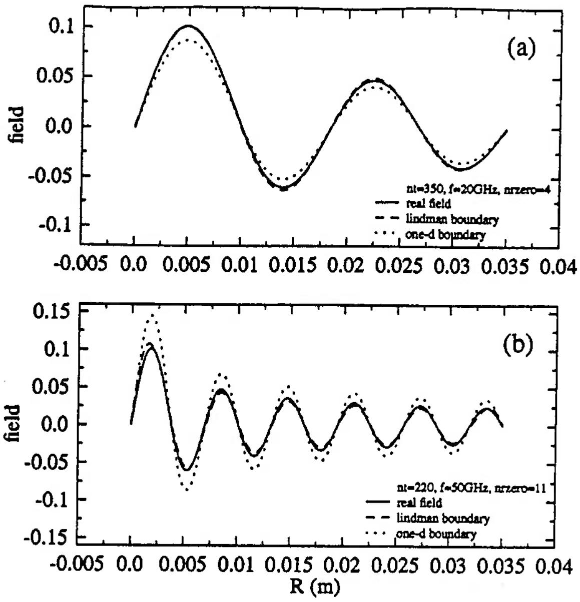

Figure 6-52: Comparison of the Lindman boundary condition with the one-dimension boundary condition used in original TBCI. Solid line: analytical; dashed line: lindman; dotted line: one-dimension. a) frequency=20 GHz, nzero=4, time steps=350; b) frequency=50 GHz, nzero=11, time steps=220.

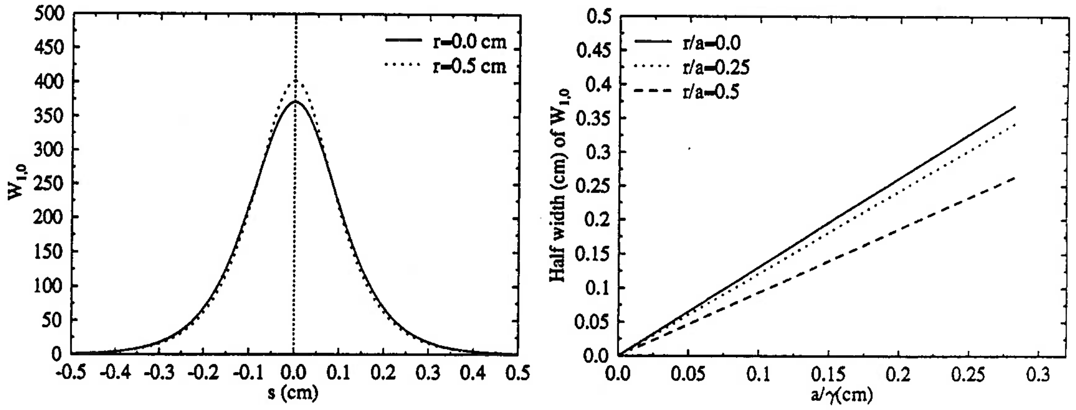

(a) (b)

Figure 6-53: Weight functions for $\beta_t = 0.9948$, $a = 1.74$ cm.

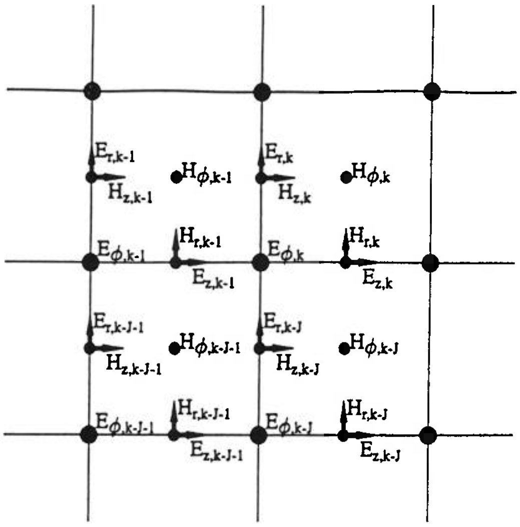

Figure 6-54: The **E** and **H** fields defined in the $r - z$ plane.

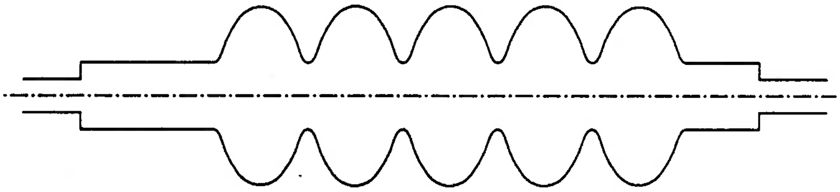

Figure 6-55: The cross section of CEBAF 5-cell cavity.

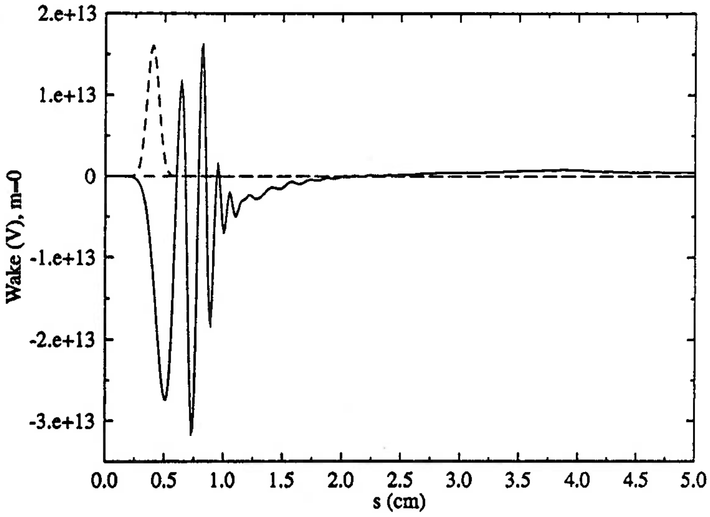

Figure 6-56: Wake function of the CEBAF 5-cell cavity. Bunch length $\sigma = 0.5$ mm. m=0

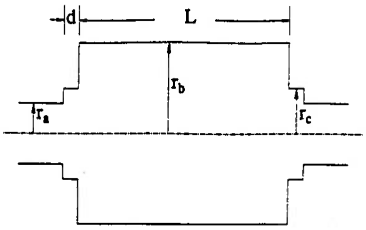

Figure 6-57: Pillbox cavity.

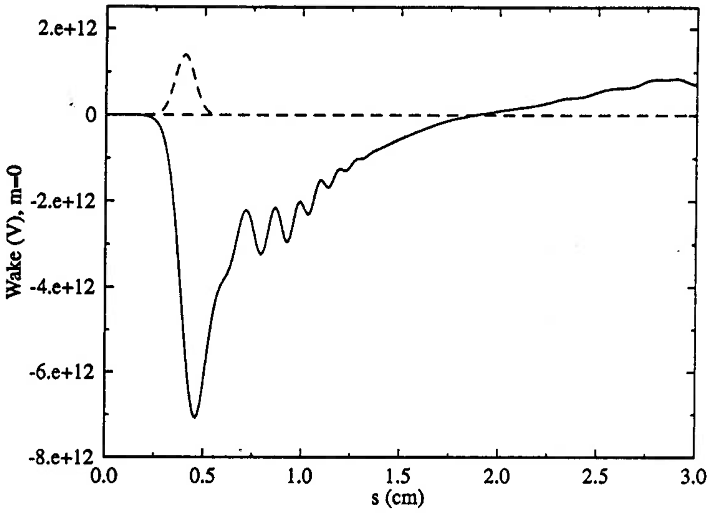

Figure 6-58: Wake function of a pillbox cavity for $\sigma = 0.5$ mm, $\sigma/\Delta z = 5$

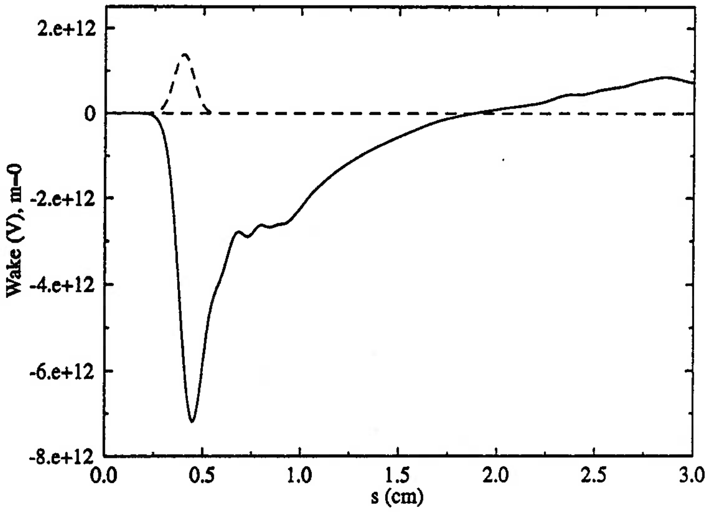

Figure 6-59: Wake function of a pillbox cavity for $\sigma = 0.5$ mm, $\sigma/\Delta z = 7.5$

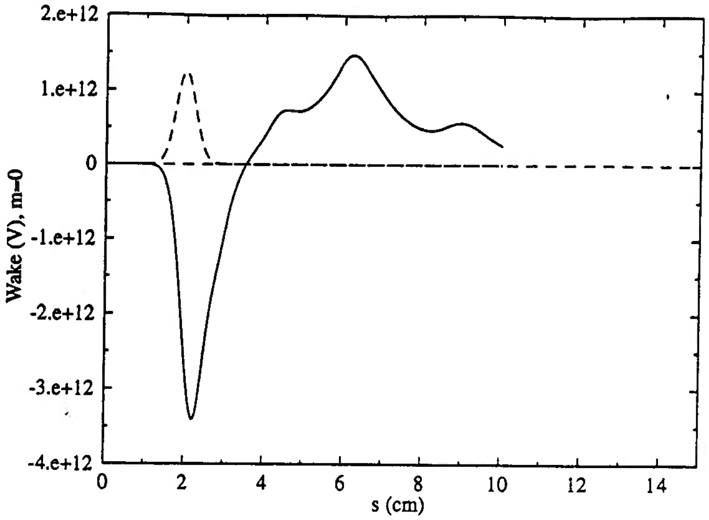

Figure 6-60: Wake function of a pillbox cavity for $\sigma = 2.5$ mm, $\sigma/\Delta z = 5$

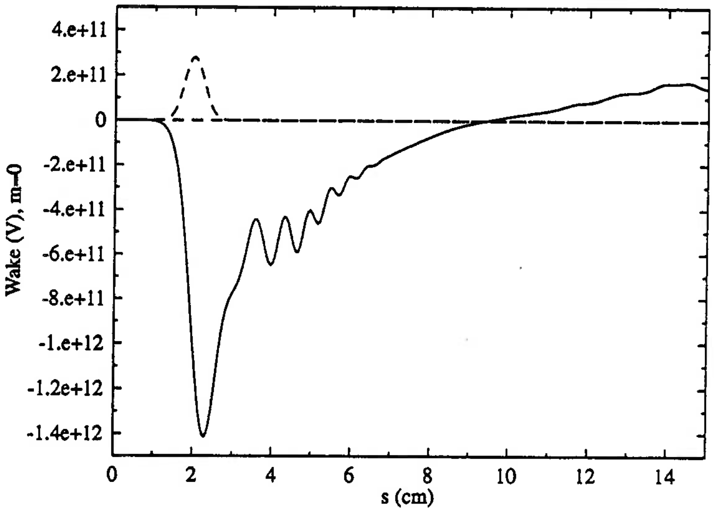

Figure 6-61: Wake function of a pillbox cavity 5 times as large as in the first run for $\sigma = 2.5$ mm, $\sigma/\Delta z = 5$

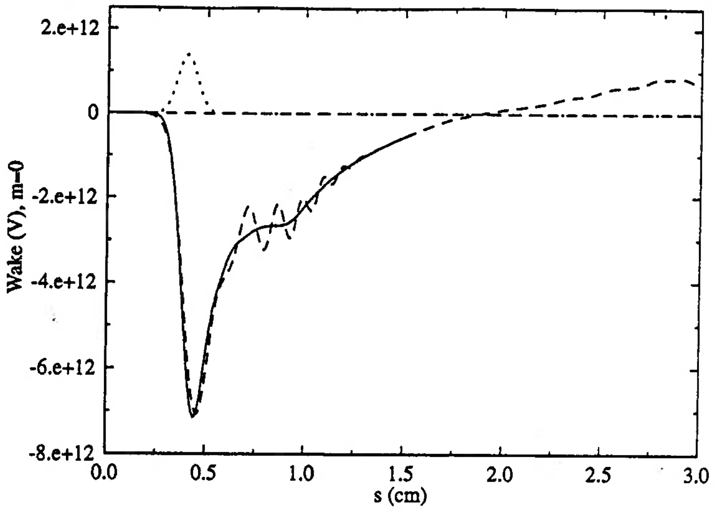

Figure 6-62: Wake function of a pillbox cavity calculated by the fourth-order FD-TD algorithm. Shown in dashed line is the second-order FD-TD result for comparison.

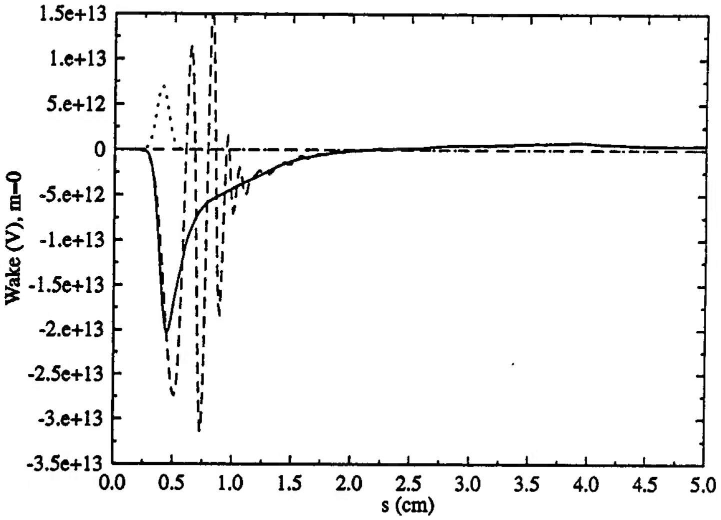

Figure 6-63: Wake function of the CEBAF 5-cell cavity calculated by the fourth-order FD-TD algorithm. Shown in dashed line is the second-order FD-TD result for comparison.

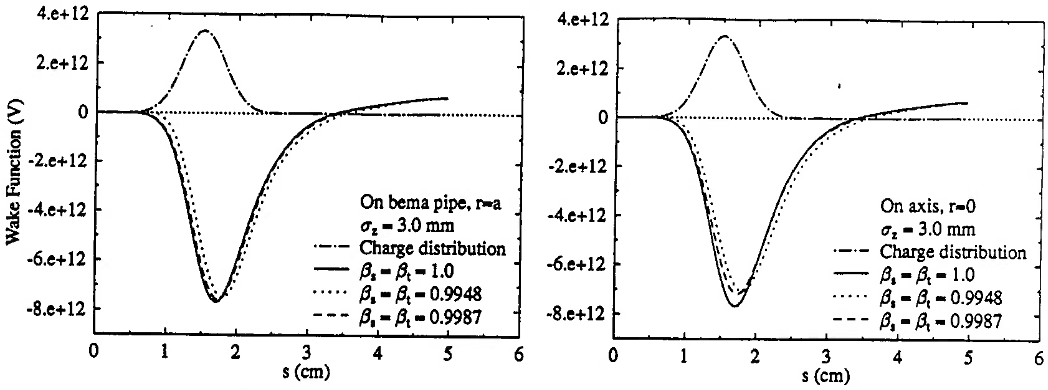

(a) (b)

Figure 6-64: Wake functions for $\beta_s = \beta_t = 0.9948$ (5 MeV) and $\beta_s = \beta_t = 0.9987$ (10 MeV). $\sigma_z = 3$ mm. a) Wake integrated on the beam pipe; b) Wake on axis.

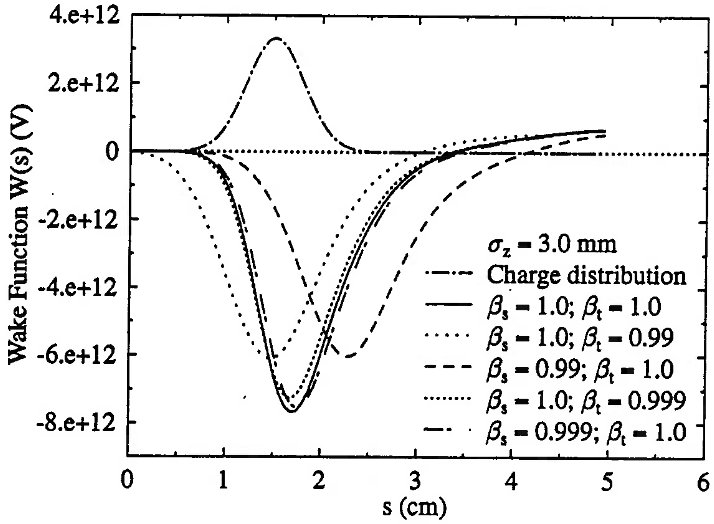

Figure 6-65: Wake functions for a) $\beta_s = 0.99$, $\beta_t = 1$ and b) $\beta_s = 1$, $\beta_t = 0.99$. $\sigma_z = 3$ mm

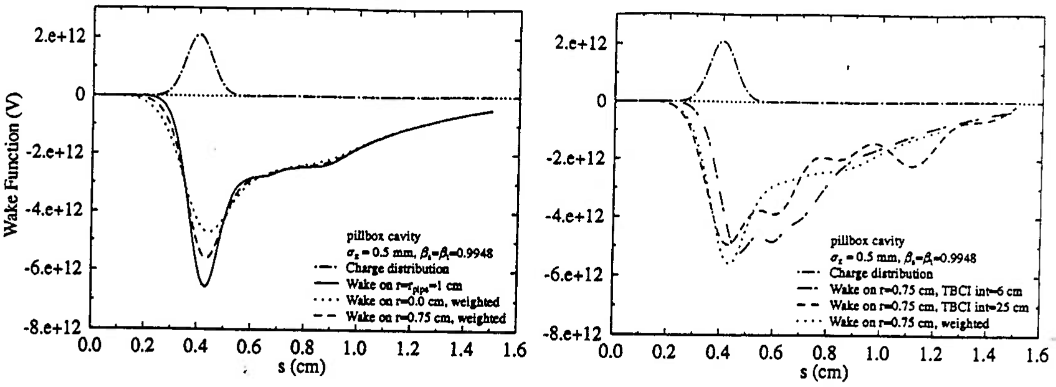

(a) (b)

Figure 6-66: Radial dependence of the wake functions for $\beta_s = \beta_t = 0.9948$. The rms bunch length is $\sigma_z = 0.5$ mm. Pillbox cavity.

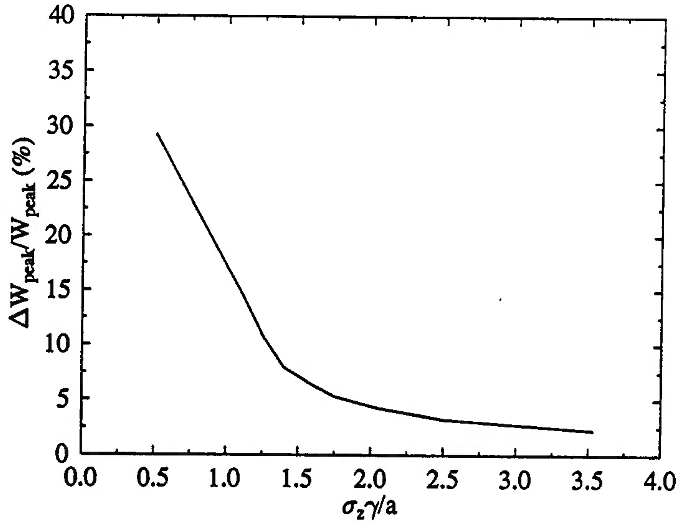

Figure 6-67: Relative difference $\frac{W_{pipe} - W_{axis}}{W_{pipe}}|_{peak}$ *vs.* $R = \frac{\sigma_z\gamma}{a}$. (calculated from the wake functions of a pillbox cavity; (r=3 cm)×(L=4 cm), pipe radius =1 cm).

Chapter 7

The Effects of Wakefields and Cavity Multipole fields on a 40 MeV IR FEL Linac

When a beam passes the cavity, it is not only accelerated by the RF field of the fundamental mode, but also radiates energy as the form of electromagnetic fields, known as wakefields, with frequencies that occupy the entire cavity eigenmode spectrum. For a high Q cavity, these fields will ring in the cavity for a long time. These fields then act back on the later beam bunches, and perturb their motion. Under unfavorable conditions, the perturbation on the beam further enhances the wakefields. The beam cavity interaction then leads to a possible collective instability. There two prime concerns about the beam cavity interactions in the CEBAF linacs. The recirculating structure of the CEBAF accelerator provides a potential mechanism for transverse multipass beam breakup. If the beam experience a momentum kick from the cavity fields, the recirculating beam will return to the cavity with a transverse displacement. On traversing the cavity second time, additional wakefields are exited. Steady state is maintained if the losses on the cavity walls and in the HOM coupler compensate the bunch excitation. At a high enough current level, there will be instability. Theoretical and experimental studies [43, 11] have shown that the threshold current for the multipass beam breakup in the CEBAF accelerator is well above the designed current. With the HOM damping mechanism employed in the cavity, the long-term wakefields are effectively minimized. The long-term wakefields are not likely to be a limiting factor to the beam current at CEBAF. As opposed to the long-term wakefield effects, another concern associated with the wakefields is the short-term or high-frequency wakefield interactions with the beam. Within the bunch region, the integrated form of the wakefield, called wake function, has a peak value and has strong variation within the bunch. For the longitudinal part of the wakefields, the forces that act upon the particles at different positions of the bunch are different and generate energy spread. The transverse part of the wakefields on the other hand may cause emittance degradation. The HOM damping mechanism are not effective in minimizing the short-term wakefield effects. There are methods of compensating the short-term wakefield effects by accelerating the beam at an RF phase other than on the crest. For a bunch much shorter than the wave length of the RF field, this compensation can only eliminate the linear part of the wakefields. The strength of the wakefield is proportional to the beam current. The stiff requirement on the energy spread and the emittance of the beams for a possible IR FEL driver at CEBAF, see Sec. 5.5 for more details on the accelerator, requires a deeper understanding of short-term wakefield effects which are the topic of this chapter. The beam dynamics simulations in this chapter include both the effects of the multipole fields of the cavity and the effects of the wakefields.

7.1 Momentum change due to the wakefields

The energy of the beam in the linac varies from 10 MeV to 40 MeV. The R value defined in Eq. (6-219) for $E = 10$ MeV, $\sigma = 0.5$ mm is 0.56. The smearing effect for this energy is strong, and the wake function at $r = 0$ should be calculated by use of the weight function. The smearing effect becomes small for energies higher than 25 MeV. The energies in the first four cavities of the FEL linac are lower than 25 MeV, so the wake functions in these cavities should be treated separately. The energy of the beam in the rest of the cavities in the linac is higher than 25 MeV, and the wake functions in these cavities are approximately the same and can be treated under the ultrarelativistic assumption.

To calculate the wakefields of a beam with bunch length of 0.5 mm in the CEBAF cavity, 7.6 million mesh points are needed. Since the whole mesh domain is needed in solving the Maxwell's equations for $\beta < 1$, the CPU time required for the wakefield calculations would be so long that it becomes impractical. The wake functions in the first four cavities have to be approximated by the wake functions of $\beta = 1$. Since the smearing flattens the peak of the wake function, this approximation will enable us to estimate the upper limit of the wakefield effects in these cavities.

For $\beta = 1$, a moving window which covers the region within which the wake functions are calculated in the bunch frame is established. Since we only need to calculate the short-range wake function, the effective number of mesh points used in the iterations is much smaller than the total number, and the CPU time requirement is reduced.

For $\beta = 1$, the wake functions have the form of Eqs. (6-165), (6-166), and (6-167). The net momentum change for a particle with charge e traversing the cavity is

$$\begin{aligned}\Delta\mathbf{P}(r,\phi,s) \;=\; & \frac{e}{v}\sum_{m=0}^{\infty}\Big(-mr^{m-1}\int_{-\infty}^{s} u_m(s')ds'\cos(m\phi)\mathbf{e_r} \\ & +mr^{m-1}\int_{-\infty}^{s} u_m(s')ds'\sin(m\phi)\mathbf{e}_\phi \\ & +r^m u_m(s)\cos(m\phi)\mathbf{e_z}\Big) \qquad (7\text{-}220)\end{aligned}$$

This equation describes the momentum change due to the existing fields in the cavity. The fields are generated by the source particle located at (r_1, ϕ_1, $z = ct$). They are proportional to the multipole strength of the source particle which is, for mode m, $I_m = qr_1^m$. In general, the momentum change of the test particle located at (r_2, ϕ_2, $z = ct - s$) due to the fields generated by the source particle located at (r_1, ϕ_1, $z = ct$) is

$$\begin{aligned}\Delta\mathbf{P}(r_1,r_2,\phi_1,\phi_2,s) \;=\; & \frac{eq}{v}\sum_{m=0}^{\infty}\Big(r_1^m r_2^{m-1}W_{T,m}(s)\cos(m(\phi_2-\phi_1))\mathbf{e_r} \\ & -r_1^m r_2^{m-1}W_{T,m}(s)\sin(m(\phi_2-\phi_1))\mathbf{e}_\phi \\ & +r_1^m r_2^m W_{L,m}(s)\cos(m(\phi_2-\phi_1))\mathbf{e_z}\Big) \qquad (7\text{-}221)\end{aligned}$$

The longitudinal and transverse wake functions $W_{L,m}(s)$ and $W_{T,m}$ are defined as

$$W_{L,m}(s) = \frac{u_m(s)}{I_m} = \int_{-\infty}^{+\infty} \frac{E_{z,m}(r_2, \phi_2, z = ct - s)dz}{q r_1^m r_2^m \cos(m(\phi_2 - \phi_1))} \tag{7-222}$$

$$W_{T,m} = -m \int_{-\infty}^{s} W_{L,m}(s')ds' \tag{7-223}$$

which are independent of r_1 and r_2. The TBCI output for the wake function is the integrated z component of the electric field

$$\int_{-\infty}^{+\infty} E_{z,m}(r_2, \phi_2, z = ct - s)dz$$

The auxiliary program TBCIIMPEDANCE or WAKEPRINT prints out $W_{L,m}$ and $W_{T,m}$.

7.2 Wake functions in the CEBAF 5-cell cavity

The CEBAF 5-cell cavity is as shown in Fig. 6-55. The rms bunch length σ_z of the FEL beam is about 1.6 ps, or 0.5 mm. The full bunch length used in TBCI is $\pm 5\sigma_z$. The mesh size to discretize the Maxwell's equations is 0.1 mm. The total number of mesh points for the 5-cell cavity is 7523295.

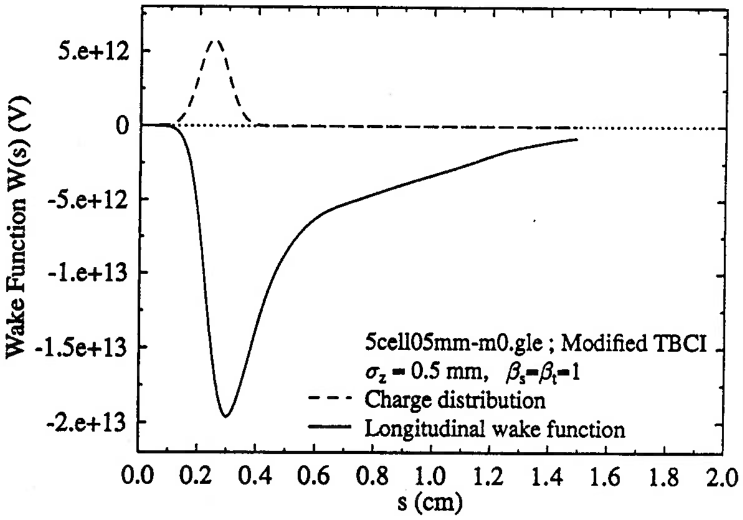

Figure 7-68: Longitudinal wake function of mode m=0 in the CEBAF 5-cell cavity for a bunch with bunch length $\sigma_z = 0.5$ mm.

7.3 Simulations of the wakefield effects in PARMELA

A separate element, called WAKE, is added to PARMELA to accommodate the calculation of the wakefield effects in the beam dynamics. The WAKE card is placed next to the cavity card in the input file. The argument for the input includes, IWAKE, Q0, SIGMA, NSIGMA, IELL. The IWAKE is a switch to turn the wake on (IWAKE=1) or off (IWAKE=0). The Q0 is the total charge of the bunch in pC. The SIGMA is the rms bunch length. The NSIGMA is the number of SIGMAs used in TBCI. The IELL is the number of elements prior to WAKE where the relative positions of the particles are evaluated.

In TBCI calculations, the particle distribution in the bunch is a δ function in the transverse plane. The actual beam size is finite. To calculate the wake generated by such a beam, we assume that all of the charges are located in the center of the beam in the transverse plane.

$$x_c = \sum_{n=1}^{N} x_n/N \tag{7-224}$$

$$y_c = \sum_{n=1}^{N} y_n/N \tag{7-225}$$

When the wake forces are applied in the PARMELA simulations, finite beam size is assumed. The relative positions of the particles are evaluated at the entrance of the cavity, that is IELL=-1. The position of the particle is recorded by means of the RF phase. Those particles with smaller RF phases arrive earlier and are in the head of the bunch. Particles with larger RF phases correspond to the tail of the bunch. For the CEBAF cavity with frequency of 1497 MHz, the relative position to the head of the bunch in centimeters in the longitudinal direction is

$$s = SIGMA * NSIGMA - \frac{20.026}{360}(\phi_0 - \phi) \tag{7-226}$$

where ϕ_0 is the RF phase at the center of the bunch. Linear interpolation is used to evaluate the wake functions off the mesh points.

7.4 The energy spread in the RF linac

There are two sources of energy spread in the RF linac. The sinusoidal RF field of the cavity produces a variation of acceleration within the finite bunch. The energy spread is a cosine-like function of RF phase. The variation of the longitudinal wakefields across the bunch also produces energy spread. Unlike the RF field, the wakefield effects depend linearly on the beam current and are independent of RF phase. The phase relations of these two kinds of energy spread make it possible to minimize the combined energy spread by properly phasing the RF phase of the cavity.

Let ϕ_0 be the RF phase of the acceleration, $\Delta\phi$ be the phase offset of a particle, and G_0 be the gradient of the cavity. The energy spread from the RF field for the particle for one cavity is

$$\Delta E_{RF}(\phi_0, \Delta\phi, G_0) = 0.5 G_0(\cos(\phi_0 + \Delta\phi) - \cos(\phi_0)) \qquad (7-227)$$

where $\Delta\phi < 0$ corresponds to the head of the bunch. The energy spread due to the wakefields, ΔE_{wake}, only depends on $\Delta\phi$, which is

$$\Delta E_{wake}(\Delta\phi) = W(\phi_0 + \Delta\phi) - W(\phi_0) \qquad (7-228)$$

The wakefields of the CEBAF cavity for the bunch length of 0.5 mm are given in Figs. 7-68 and 7-69. The total energy spread due to the RF field and the wakefield is

$$\Delta E(\phi_0, \Delta\phi) = \Delta E_{RF}(\phi_0, \Delta\phi, G_0) + \Delta E_{wake}(\Delta\phi) \qquad (7-229)$$

Assuming that the bunch has a Gaussian distribution, the rms energy spread of the bunch is

$$\sigma^2_{e,rf+wake}(\phi_0) = \frac{1}{\sqrt{2\pi}\sigma_z} \int_{-\infty}^{+\infty} (\Delta E(\phi_0, \Delta\phi(s)))^2 e^{-\frac{s^2}{2\sigma_z^2}} ds \qquad (7-230)$$

where σ_z is the rms bunch length, $\Delta\phi(s) = s\frac{360}{\lambda}$, $\lambda = 20$ cm for CEBAF cavity, and $\sigma_z = 0.5$ mm.

The energy spread, $\sigma_{e,rf+wake}(\phi_0)$, is now a function of the acceleration phase ϕ_0 only. Optimal ϕ_{opt} exists for a minimum energy spread. Fig. 7-70 shows the rms energy spread of the beam with different charges as functions of the RF phase of the cavity, where the gradient of the cavity is G_0=7.5 MV/m and the bunch length is σ_z=0.5 mm. For very low charge, the energy spread is caused solely due to the RF field. As the total charge of the bunch increases, the wakefield effects become significant. At certain RF phase, cancellation exists between the energy spread from the RF field and that from the wakefields. The total energy spread at this RF phase has a minimal value. When the total charge of the bunch becomes large, the wakefield effects become dominant. The total energy spread increases with the bunch charge. For the IR FEL, the total charge is Q =200 pC. The energy spread has a minimum of 4.4×10^{-4} MeV at $\phi_0 = -1^0$, which is smaller than minimum energy spread from the RF field. The energy spread $\Delta E_{RF}(\phi_0 = -1^0, \Delta\phi, G_0 = 7.5)$, $\Delta E_{wake}(\Delta\phi)$ and $\Delta E(\phi_0 = -1^0, \Delta\phi)$ along the bunch for this case are shown in Fig. 7-71.

The energy spread analyzed above is related to the RF field of the cavity and the longitudinal wakefield of the cylindrical symmetric mode (m=0). If the bunch is off axis, the longitudinal wakefield of the dipole mode (m=1) will also cause energy spread. However, since the dipole wakefield is proportional to $r_s \cdot r_t$, the contribution of the dipole mode is of higher order.

The energy spread of the beam includes the initial energy spread of the beam and the energy spread from the RF field and the wakefields. They are not correlated. The total energy spread of the beam is then

$$\sigma_E = \sqrt{\sigma_{E,0}^2 + \sigma_{RF+wake}^2} \qquad (7-231)$$

To study this matter more carefully, numerical simulations using PARMELA were performed. The initial energy spread ($\sigma_{E,0}$) at 10 MeV is 3×10^{-2} MeV. The PARMELA simulation of the energy spread of the FEL linac at the exit of the linac as a function of the acceleration phase is shown in Fig. 7-72. It is shown that in order to get a relative energy spread less than 2×10^{-3} at 40 MeV, the RF phase offset of the cavity should be within the range of (-10^0, 7.5^0).

7.5 The emittance in the FEL linac

The multipole RF fields of the cavity and the wakefields generated by the beam are the two sources of emittance degradation in the linac. The emittance degradation due to the RF fields is studied in Sec. 5.5. In this section, we will include the effect of the wakefields. The dominant mode of the wakefields that causes the emittance growth is the dipole mode, which is similar to the head-tail effects of the cavity multipole fields. The dipole mode of the wakefields can only be excited when the beam has an offset from the axis of the cavity. To reduce the wakefield head-tail effect, beam centering is important. However, the beam offset may result from some undetermined factors like the cavity misalignment and the cavity steering of the coupler fields. The misalignment of the cavity is within 1 mm. The beam offset from the cavity steering on the other hand is unavoidable since there are no orbit correctors inside the cryomodule. The upper limit of the emittance growth is estimated by assuming that the cavity is misaligned with a maximum possible misalignment.

The steering of the dipole mode of the wakefields has the following form

$$\Delta \mathbf{P}_{\perp}(r_0, r, \phi_0, \phi, s) = \frac{eq}{v}\left(r_0 W_{T,1}(s)\cos(\phi - \phi_0))\mathbf{e_r} - r_0 W_{T,1}(s)\sin(\phi - \phi_0))\mathbf{e}_{\phi}\right) \tag{7 - 232}$$

where (r_0, ϕ_0) is the transverse position of the center of the bunch and (r, ϕ) is the transverse position of a particle in the bunch. The strength of the transverse wake function linearly increase along the bunch. The result is that the tail gets kicked more, and the projected emittance is then increased.

Assuming that the beam has a initial offset of 1 mm, the PARMELA simulations show (Fig. 7-73) that the emittance has little dependence on the RF phase. The emittance degradation is mainly due to the cavity multipole fields. The contribution from the wakefields is negligible. The total emittance growth in the linac is about 60%.

The wakefield effects are proportional to the total charge of the bunch. Simulations indicate that there is no significant emittance growth for a total charge of 200 pC. The weak wakefield effects on the emittance growth can be attributed to the large opening of the cavity which results in low transverse wakefields. The large initial emittance is also a factor that makes the emittance growth less noticeable.

The PARMELA simulations on the energy spread and the emittance degradation conclude that the wakefield effects in the 40 IR FEL linac will not become a limiting factor on the beam qualities. The 2×10^{-3} relative energy spread is easily achievable within a wide range of RF phase (-10^0 to 7.5^0). The emittance growth is dominated by the $x - y$ coupling of the cavity multipole fields, which can be corrected by use of a compensation skew quadrupole placed in front of the linac (see section 5.5).

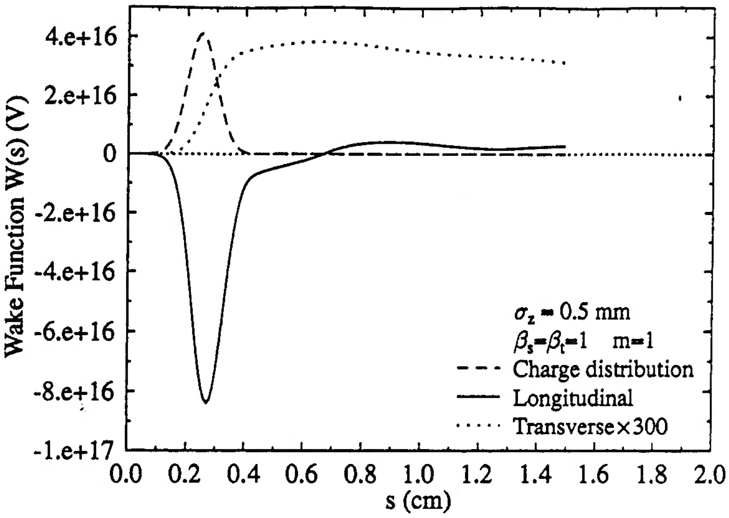

Figure 7-69: Wake functions of mode m=1 in the CEBAF 5-cell cavity for a bunch with bunch length of $\sigma_z = 0.5$ mm.

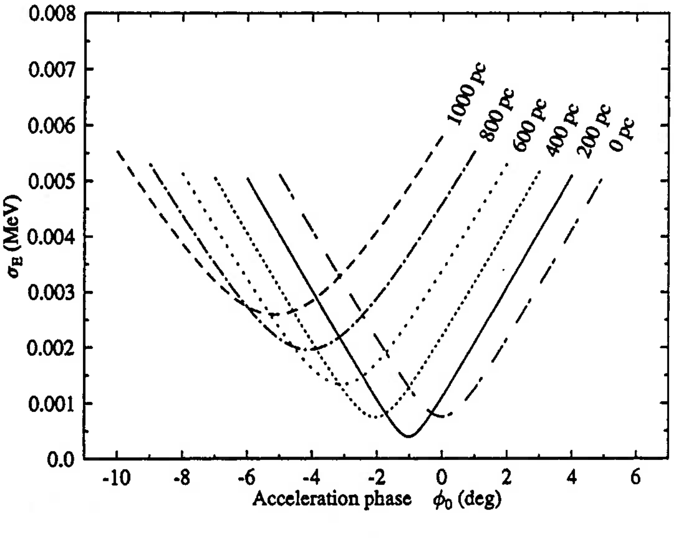

Figure 7-70: Induced rms energy spread of the beam *vs.* the acceleration phase ϕ_0. Gradient=7.5 MV/m, rms bunch length $\sigma_z = 0.5$ mm, charge=200 pC.

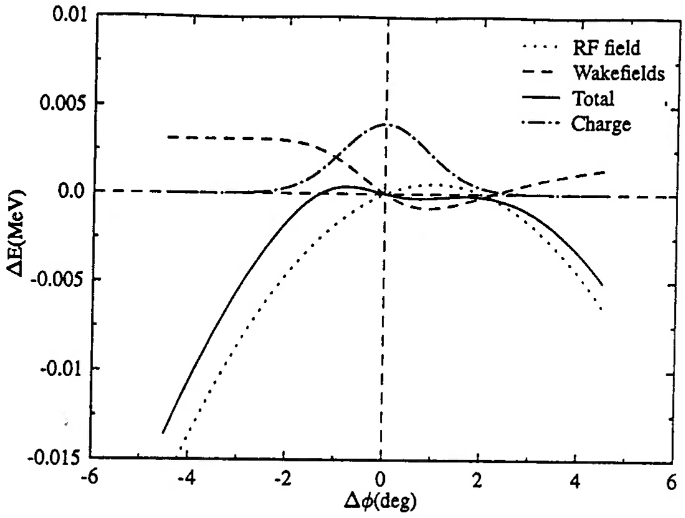

Figure 7-71: Energy spread due to the RF field and the wakefield. Gradient=7.5 MV/m, RF phase=-1^0, rms bunch length σ_z = 0.5 mm, charge=200 pC.

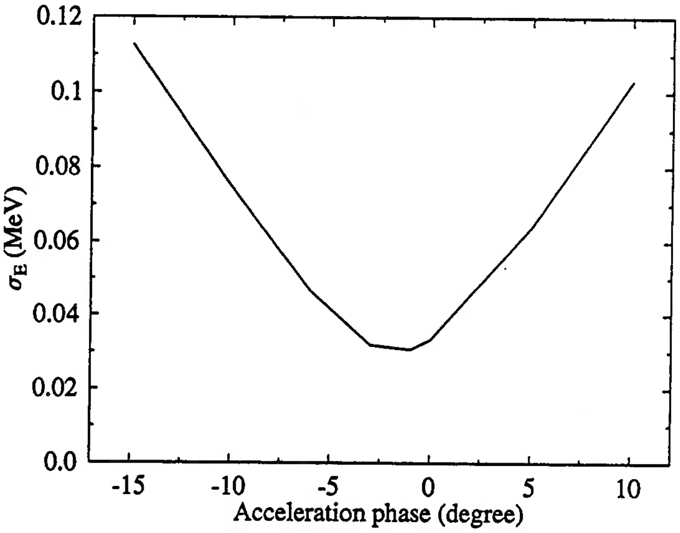

Figure 7-72: PARMELA simulation of energy spread in the FEL driver. Gradient=7.5 MV/m, rms bunch length σ_z = 0.5 mm, charge=200 pC.

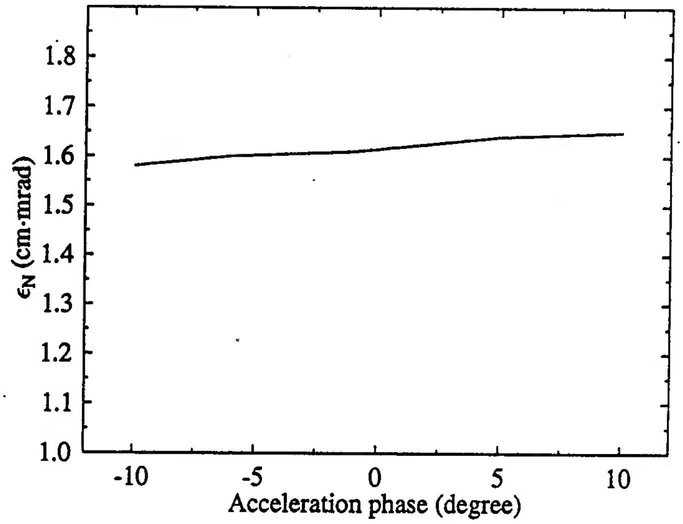

Figure 7-73: Normalized emittance as a function of the RF phase in the FEL driver. ϵ_0 = 1cm·mrad; Gradient=7.5 MV/m; Bunch length $\sigma_z = 0.5$ mm; Charge=200 pC.

Chapter 8

Conclusions

The dynamics of beams under the influence of multipole fields of the cavity and wakefields generated by the beam have been studied.

Full three-dimensional modeling of the cavity, which includes the 5-cells and the FP the HOM couplers, was established. The 3-D code MAFIA was used for this purpose. Several steps have been taken to make the modeling better represent the real cavity: a) the resonant frequency was tuned back to 1497 MHz by adjusting the radii of the five cells; b) a flat field distribution in the 5-cells is obtained by slightly adjusting the size of the two end cells; c) the short position of the fundamental mode in the waveguide is determined from the tuning curve of the cavity so that a proper boundary condition on the FP coupler can be applied; d) the coupling strength of the FP to the end cell is obtained to match the forward power flow in the FP waveguide. The 3-D fields calculated by use of MAFIA are Fourier decomposed in a 3-D cylindrical coordinate system. The multipole fields and their impact on beam dynamics were analyzed. Experimental measurements were performed to measure the multipole fields of the cavity, and the results agree with the numerical simulations. The misalignment of a cavity was estimated from experimental results of the cavity steering, and the resulting misalignment of the cavity found to be within specification.

A full 3-D modelling of the CEBAF superconducting cavity was included in the particle tracking program PARMELA. Numerical studies of the beam dynamics were carried out in the CEBAF injector, linacs, and a possible FEL driver. The head-tail and the $x - y$ coupling effects in the cryounit of the injector were found to be strong.

A 70% emittance growth was predicted in the cryounit. The emittance growth in the cryomodules of the injector depends strongly on the betatron matching conditions of the beam. It was found that large emittance growth can result if the β functions in the cryomodules are large. Emittance growth in the injector can be suppressed by changing the focusing of the cryounit by adjusting the RF phase of the first cavity. Head-tail effects in the CEBAF north linac are small due to the short bunch length and the cancellation between the cavity-pairs in the cryomodules. Cancellation of the head-tail effects relies on the gradient distribution in the cryomodules. Emittance growth due to the $x-y$ coupling is negligible for the first pass if the beam is well matched into the linac. In the higher passes, emittance growth under matched conditions are of order of 35%. Emittance growth for unmatched cases is more sensitive to the initial αs than the initial βs. It is important to match the beam with waists for the first pass. In the higher passes, the most unfavorable mismatch conditions are those with negative αs, *i.e.* initially diverging beams. Under nominal conditions, the final emittance of the CEBAF accelerator will remain within specification. Emittance growth in a 40 MeV IR FEL linac is about 60%, which is mainly due to $x-y$ coupling.

The behavior of the wake functions for $v_s, v_t \neq c$ was investigated. This issue is important in multipass FEL linacs and the low energy IR FEL linac. Wakefield calculations were based on code TBCI with several modifications. With the implementation of the Lindman boundary condition, the code is capable of dealing with both $v = c$ and $v < c$ with proper open boundary conditions. In addition, the truncation errors of the second-order YEE algorithm were found to be frequency dependent and were important in the calculation of wakefields of short bunches. A fourth order accuracy finite-difference algorithm was derived and was implemented in the modified TBCI to reduce the truncation errors. For the cases of $v_t \neq v_s$, the slippage between the source and the test particles was included in the wake function integration. A radial scaling algorithm for the wake function was obtained in order to calculate the wake functions inside the beam pipe. We found that the wake function at a radial position r is a weighted average of the wake function calculated at the pipe radius. It was found that the quantity that measures the smearing effect on the wake function's not only depends on the energy of the beam but also on the bunch length and the opening of the beam pipe. The quantity that measures the smearing effect is $R = \frac{\sigma_z \gamma}{a}$ where a is the pipe radius. We found that the smearing effects for $R > 1.5$ are, in general, small enough to be neglected. In such cases, the ultrarelativitic assumption for the beam can be used.

PARMELA simulations on the energy spread and the emittance degradation indicated that the wakefield effects in a proposed 40 IR FEL linac will not be a limiting factor on beam quality. The 2×10^{-3} relative energy spread is easily achievable within a wide range of RF phase (-10^0 to 7.5^0). Emittance growth is dominated by $x - y$ coupling driven by cavity multipole fields, which can be corrected by use of one skew quadrupole placed in front of the linac.

References

[1] H. Piel, "Fundamental Features of Superconducting Cavities for High Energy Accelerators," CAS Advanced Accelerator Physics, The Queen's College, Oxford, England, 1985.

[2] P. Kneisel, "Results of Some LALA-calculations for Accelerator Cavity with Elliptical Cross-section," SRF-820703.

[3] Los Alamos Accelerator Code Group, Reference Manual for the Poisson/Superfish Group of Codes, LA-UR-87-126.

[4] R. Sundelin, "Superfish Studies of the Elliptical Cavity Fundamental Mode," SRF-820803.

[5] J. Kirchgessne, "Preliminary measurements on LCY Fundamental Power Coupler," SRF-820902.

[6] C. Reece, "Fundamental Power Coupler E-field Profile Measurements," SRF-831201.

[7] R. Klatt et al.,"MAFIA - A Three-Dimensional Electromagnetic CAD System for Magnets, RF Structures and Transient Wake-Field Calculation", Proc. 1986 Linear Accelerator Conference, pp. 276, 1986.

[8] C. M. Lyneis, et al., NIM, 204, 269 (1983).

[9] J. J. Bisognano and G. A. Krafft, "Multipass Beam Breakup in the CEBAF Superconducting Linac," 1986 Linear Accelerator Conference Proceedings, SLAC 303, 452.

[10] J. J. Bisognano and R. L. Gluckstern, "Multipass Beam breakup in Recirculating Linacs," CEBAF-PR-87-007.

[11] N. Sereno, "Experimental Studies of Multipass Beam Breakup and Energy Recovery Using the CEBAF Injector Linac", Ph.D. thesis, University of Illinois, 1993.

[12] T. Weiland, "Transverse Beam Cavity Interaction, Part I: Short Range Forces," Nuclear Instruments and Methods, Vol. 212(1983), pp. 13-34.

[13] S. Heifets and B. Yunn, "Impedances of CEBAF superconducting Accelerator," CEBAF Technical note TN-0063, 1987.

[14] B. C. Yunn and J. J. Bisognano, "A Numerical Study of Superconducting Cavity Components," Proceedings of 1990 Linear Accelerator Conference, pp. 93, 1990.

[15] J. C. Slater, Microwave Electronics, D. Van Nostrand Company, Inc.

[16] J. J. Bisognano, Accelerator Physics, Class Notes, The College of William and Mary, 1991.

[17] J. D. Jackson, Classical Electrodynamics, John Wiley, New York, 2nd edition, (1962).

[18] "PARMELA - A Particle Dynamics Code for Electron Linacs," User's guide.

[19] B.Austin, T.W. Edwards, J. E. O'Meara, M.L. Palmer, D. A. Swenson, and D. E. Young, "The design of Proton Linear Accelerators for Energies Up to 200 MeV," MURA report No. 713, July 1, 1965.

[20] G. A. Krafft, J. Jackson and D. Douglas,"First Order Focusing and Steering of Misaligned Cavities," CEBAF-TN-90-0287.

[21] G. A. Krafft, "More on the Transfer Matrix of a Cavity," CEBAF-TN-91-069.

[22] G. Biallas and P. Brindza,"The CEBAF Cavity Cryostat," CEBAF-PR-86-004.

[23] Bruce Bowling, Private communication.

[24] N. S. Sereno,"Accelerator Physics Experiments Using a Beam Recirculated Through the Injection Accelerator at CEBAF," CEBAF-TN-90-282.

[25] Experiment was performed with Mike Tiefenback and Byung Yunn.

[26] R. C. York and C. Reece, "RF Steering in the CEBAF CW Superconducting Linac," CEBAF-PR-87-013.

[27] D. R. Douglas and R. C. York,"Transfer Matrix Simulating Motion Through a Linac Cavity," CEBAF-TN-0132, 1989.

[28] D. R. Douglas, Private communication.

[29] D. Douglas, S. Chen, and J. van Zeijts, "A Lattice Design for an IR FEL Driver," CEBAF-TN-94-037.

[30] "High-Power Ultraviolet and Infred Free-Electron Laser For Industrial Processing," Reference Design Report, The Laser Processing Consortium, May 1994.

[31] R. L. Gluckstern and B. Zotter, "Coupling Impedance for Asymmetric Cavities," CERN-LEP-613, July 1988.

[32] G. Dome, IEEE Transactions on Nuclear Science, Vol. NS-32, No. 5, October 1985, pp. 2531.

[33] S. A. Heifets and S. A. Kheifets, "High frequency Limit of the Longitudinal Impedance," CEBAF-PR-87-030, 1987.

[34] Y. H. Chin, User's Guide for ABCI, LBL-35258.

[35] Kane S. Yee,"Numerical Solution of Initial Boundary Value Problems Involving Maxwell's Equations in Isotropic Media," IEEE Trans. Antennas Proragation, vol. AP-14, pp. 302-307, May 1966.

[36] T. Weiland, "Comment on Wake Field Computation in Time Domain," Nucl. Inst. and Meth. 216 pp. 31-34, 1983.

[37] E. U. Condon, J. Appl. Phys. 12, 129 (1941).

[38] Alex W. Chao, Physics of Collective Beam Instabilities in High Energy Accelerators, John Wiley & Sons, Inc. 1993.

[39] A. Taflove, "Review of The Formulation and Applications of the Finite-difference Time-domain Method for Numerical Modeling of Electromagnetic Wave Interactions with Arbitrary Structures," Wave Motion, pp. 547-582, 1988

[40] E. L. Lindman, " 'Free-Space' Boundary Conditions for the Time Dependent Wave Equation," J. Comp. Phys. 18, pp. 66-78 (1975).

[41] W. K. H. Panofsky and W. A. Wenzel, "Some Considerations Concerning the Transverse Deflection of Charged Particles in Radio-Frequency Fields," Rev. Sci. Instr. 27, 967 (1956).

[42] J. Fang, Time Domain Finite Difference Computation for Maxwell's Equations, Ph.D. thesis, University of California at Berkeley, 1989.

[43] J. J. Bisognano and G. A. Krafft,"Multipass Beam Breakup in the CEBAF Superconducting Linac," CEBAF-PR-86-001.

VITA

Zenghai Li

Zenghai Li was born on November 18, 1962 in Wuji, Hebei province, the People's of Republic of China. He graduated from the county high school in 1978, one year after China re-established the national examinations for higher educations, and then he went to Hebei University, Baoding, Hebei, where he got his B.S. degree in infrared ray physics in 1982. He continued his graduate study at the China Institute of Atomic Energy in Beijing, and he got his Master's degree in accelerator physics in 1985. He worked at the China Institute of Atomic Energy as a research assistant from 1985 through 1989. In January 1989, he went to LAMPF, Los Alamos National Laboratory, USA, as a visiting scholar. He worked with MP-14 group there for two years. In January 1991, he entered the College of William and Mary for advanced graduate studies, and he worked at CEBAF (the Continuous Electron Beam Accelerator Facility) as a graduate research assistant with the Accelerator Physics Theory group. He is married to Zhaomei Zhang. They have a daughter, Jessica, who was born in August 1993. Zenghai Li is a member of the American Physics Society.